The Dissertation Committee for John Paul Cesar certifies that this is the approved version of the following dissertation:

The Search for Periodic Modulations of Nuclear Decay Rates with the NEMO-3 Experiment and Development of the Light Injection Monitoring System for the SuperNEMO Experiment

Committee:

Karol Lang, Supervisor

Jack Ritchie

Duane Dicus

Tim Andeen

Karl Gebhardt

The Search for Periodic Modulations of Nuclear Decay Rates with the NEMO-3 Experiment and Development of the Light Injection Monitoring System for the SuperNEMO Experiment

by

John Paul Cesar, B.S.

Dissertation

Presented to the Faculty of the Graduate School of
The University of Texas at Austin
in Partial Fulfillment
of the Requirements
for the degree of

Doctor of Philosophy

The University of Texas at Austin
December, 2016

The Search for Periodic Modulations of Nuclear Decay Rates with the NEMO-3 Experiment and Development of the Light Injection Monitoring System for the SuperNEMO Experiment

John Paul Cesar, Ph.D.
The University of Texas at Austin, 2016

Supervisor: Karol Lang

A search for periodic modulations of nuclear decay rates has been carried out using data from the NEMO-3 experiment. The Lomb-Scargle periodogram technique and it's error-weighted extension known as the Generalized Lomb-Scargle periodogram, both used in analyzing unevenly spaced time series, were applied to the Phase 2 data set spanning 6.0195 yrs. A study of double beta ($\beta\beta$) decay rates originating from ^{100}Mo source foils has shown no evidence of periodic modulation between the sample frequency range of $0.083063 - 365.25\,\mathrm{yrs}^{-1}$. Monte Carlo methods were used to test the sensitivity to detection of previously claimed modulations. For a yearly periodicity in $\beta\beta$ decay rates, a limit has been set for the relative amplitude of such a modulation of 2.1% at the 90% confidence level.

In addition to this, a calorimeter monitoring system has been developed for the successor to NEMO-3. SuperNEMO is a next generation detector that will employ the same powerful approach to search for neutrinoless double beta decay with half-life sensitivities on the order of 10^{26} years corresponding to $\langle m_{\beta\beta}\rangle < 50\,\mathrm{meV}$. One of the most important features of any detector searching for $0\nu\beta\beta$ decay is its energy resolution and thus it's crucial to monitor and correct for any changes in this parameter over time. A Light Injection (LI) system has been developed to monitor and help calibrate the response of 712 SuperNEMO calorimeter modules over the lifetime of the experiment. The LI system will inject, via optical fiber, UV light from light emitting diodes into each calorimeter optical module to track its behavior between absolute calibration runs to a precision of 1%. In addition, the system can also be used to test the linearity of modules up to incident electron energies as high as 5 MeV.

Contents

List of Figures vii

Chapter One: Introduction 1
Time Variability of Fundamental Constants 3
New Physics Interactions 8

Chapter Two: Nuclear Decays 10
History of Radioactivity 11
Types of Nuclear Decay 11
Nuclear Decay Rates 18
Related Claims 23

Chapter Three: The NEMO-3 Detector 27
Detector Description 27
General Design 28
The Source Foils 31
The Tracking Volume 38
The Calorimeter 42
Magnetic Coil and Passive Shielding 47
Calibration and Monitoring 49
The Anti-Radon System 53

Chapter Four: NEMO-3 Data 56
Monte-Carlo Simulations 57
Event Trigger and Reconstruction 58
Particle Identification 60
Time of Flight 63
Event Selection 67
Detector Efficiency 72
Decay Rate Time Series 77

Chapter Five: Analysis Technique 80
Frequency Domain Analysis 80
$\beta\beta$ Decay Rate Analysis Results 91

Chapter Six: The SuperNEMO Detector 115
Detector Description 115
General Design and the SuperNEMO Demonstrator 116
The Source Foils 118
The Tracking Volume 122
The Calorimeter 122
Radiopurity 126
Performance 127

Chapter Seven: The Light Injection Monitoring System 128
Introduction 128
Design Principles 129
Optical Performance 143
Optical Module Monitoring Performance 150

Chapter Eight: Conclusions 162

Bibliography 166

List of Figures

2.1. Semi-Empirical Mass Formula for a Generic Nuclei 17
2.2. Normalized BNL Decay Rate versus Time 21
2.3. Normalized PTB Decay Rate versus Time 22
2.4. Ratio of the BNL and PTB Data 23
2.5. Power Spectrum of the BNL Decay Rate Data 24
2.6. Power Spectrum of the DAMA/NaI Data 25
2.7. Power Spectrum of the DAMA/LIBRA Data 25
2.8. Power Spectrum of the Super-Kamiokande Solar Neutrino Flux Data . . . 26

3.1. $\beta\beta$ Decay Electron Energy Sum Distribution 29
3.2. The NEMO-3 Detector 29
3.3. Natural Gamma Backgrounds 33
3.4. NEMO-3 Source Distribution 34
3.5. NEMO-3 Geiger Cell Layout 39
3.6. NEMO-3 Geiger Cell 40
3.7. NEMO-3 Calorimeter Optical Module 47
3.8. Radon Trapping Principle 55

4.1. Bismuth-Polonium Event Display 62
4.2. Isolated Gamma Hits Example 63
4.3. Non-Isolated Gamma Hits Example 64
4.4. Crossing Electron Event Display 68
4.5. External Electron-Gamma Event Display 69
4.6. Candidate $\beta\beta$ Decay Event Display 73
4.7. Distribution of Number of Selected Events per Run 74
4.8. Distribution of Lengths per Run 74
4.9. Distribution of Decay Rates per Run 75
4.10. Detector Efficiency Versus Run 76
4.11. Distribution of Scaled Decay Rates per Run 78
4.12. Distribution of Scaled Decay Rate Errors per Run 78

4.13. Measured ^{100}Mo ββ Decay Rate Time Series 79

5.1. Lomb-Scargle Periodogram Example - No Modulation 91
5.2. Lomb-Scargle Periodogram Example - Modulated 92
5.3. Power Spectrum Analysis of ^{100}Mo ββ Decay Rate - Full Frequency Range 96
5.4. Power Spectrum Analysis of ^{100}Mo ββ Decay Rate - Reduced Frequency Range 98
5.5. LS Result Significance Testing 100
5.6. GLS Result Significance Testing 101
5.7. LS Sensitivity Contours for P2 ^{100}Mo ββ Decay Rate 103
5.8. GLS Sensitivity Contours for P2 ^{100}Mo ββ Decay Rate 104
5.9. LS Detection Error Contours for P2 ^{100}Mo ββ Decay Rate 106
5.10. GLS Detection Error Contours for P2 ^{100}Mo ββ Decay Rate 106
5.11. LS Sensitivity Contour Shifts Due to Modulation Phase 108
5.12. GLS Sensitivity Contour Shifts Due to Modulation Phase 109
5.13. LS Sensitivity Contours After Efficiency Systematic Smearing 112
5.14. GLS Sensitivity Contours After Efficiency Systematic Smearing 112
5.15. LS Sensitivity Contours After Signal Events Systematic Smearing 113
5.16. GLS Sensitivity Contours After Signal Events Systematic Smearing . . . 113

6.1. The SuperNEMO Demonstrator 118
6.2. SuperNEMO Source Frame 120
6.3. SuperNEMO Main Wall Optical Module 124

7.1. Light Injection (LI) Rack 130
7.2. LI System Illustration 132
7.3. LI Pulser Box Schematic 135
7.4. LED Driver Circuit 136
7.5. LED and Scintillator Spectra 139
7.6. LI Fiber Connector 141
7.7. LI Fiber Bundle 142
7.8. LI Fiber Bundle Testing 148
7.9. LI Fiber Bundle Uniformity Test Results 149
7.10. LI Test Bench 153
7.11. Test Bench DAQ Diagram 154

7.12. Test Bench ADC Spectra 155
7.13. Test Bench Stability 157
7.14. Test Bench Monitoring Accuracy 158
7.15. Test Bench Temperature Effects 160
7.16. Test Bench Temperature Correlations 161

Chapter One: Introduction

The modern day understanding of fundamental particle physics is summed up in a very successful theory known as the Standard Model (SM). Although this theory has stood up to the scrutiny of many high precision experiments, the model is still known to be incomplete. Aside from the fact that it is currently not unified under one framework with regards to gravitational theory, the SM has shown an inability to fully explain certain observed phenomena. The discovery that neutrinos oscillate and thus have mass, for example, is in disagreement with the SM description of these particles. In the search for a more unified theory of fundamental physics, these inconsistencies must be exposed and probed in greater detail.

One area that has been of interest in trying to find new physics hidden within the SM has to do with the possible time variation of fundamental constants [1] [2] [3]. Such constants govern processes that have long been considered to be immutable with respect to temporal or spatial variations as well as external influences. These processes require that the laws of physics be independent of time, place, and environmental conditions. Any non-standard variation of these processes or their underlying constants of nature may imply the presence of new Beyond the Standard Model (BSM) physics.

Recent claims imply that certain radioactive nuclear decays, specifically β decays, may exhibit periodic temporal variations in their decay rates [4], [5], [6]. All nuclear decays are goverened by the various fundamental forces and such processes have long been considered unaffected by external temporal or environmental effects, including those which may lead to a periodic modulation. The observation of such modulations

in nuclear decay rates may in fact point towards new BSM interactions that shed light on the path towards a more complete understanding of fundamental physics.

Although the NEMO-3 experiment was designed to search for a different BSM process known as neutrinoless double-beta decay ($0\nu\beta\beta$), the unique features of the detector and primarily its ability to isolate individual decay channels with high signal to background ratios has permitted the use of NEMO-3 data to further investigate the possibility of periodic modulations in nuclear decay rates.

This dissertation presents the results of analyzing over seven years worth of NEMO-3 nuclear decay data to search for periodic modulations in the measured $2\nu\beta\beta$ decay rate of ^{100}Mo. This work represents the first time such modulations have been searched for in $\beta\beta$ decays which are a second-order weak process. In addition to the analysis of NEMO-3 data in the context of nuclear decay rate variability, work was also carried out in preparation for the next generation successor to NEMO-3, known as SuperNEMO. The second part of this work focuses on the R&D efforts surrounding the development and testing of a calibration system to be used in the SuperNEMO experiment.

This first chapter will continue with an overview of the fundamental physics motivation behind the analysis carried out in this thesis while chapter 2 will go into more detail about the particular case of temporally modulated nuclear decay rates. Chapter 3 will introduce the NEMO-3 experiment and details of its detector. Chapter 4 will discuss the NEMO-3 data sets and extraction of the decay rate times series for different channels. Chapter 5 will present the analysis technique employed to search for periodic variations in time series and give the results of applying this search to NEMO-3 decay rate data. Chapter 6 will then move on to to describe and discuss the next generation $\beta\beta$ decay detector known as SuperNEMO. Chapter 7 will focus on

the development of the Light Injection (LI) Monitoring system for the SuperNEMO calorimeter. Finally, chapter 8 will summarize and conclude the works of this thesis.

1.1 Time Variability of Fundamental Constants

The most complete framework describing the known forces, interactions, and constituents of the Universe is the Standard Model of particle physics coupled with the theory of General Relativity. Taken together, these theories are built upon a number of independent parameters which determine the relative strength of the different forces, various matrix angles and phases, and the masses of fundamental particles. These parameters are referred to as fundamental constants because they cannot be explained or predicted (in terms of precise numerical values) *a priori* by the theories they comprise. In addition, the total number of such constants depends on which physical models are being considered. A common property of many proposed BSM models is a reduction in the total number of fundamental constants either by demonstrating that either some of the known constants are not truly fundamental or they are in fact not constant. In general, the values of fundamental constants are determined by vacuum expectation values of one or more scalar fields so that variations in the values are often implicit in different BSM models.

Paul Dirac first suggested, in 1937, the notion that fundamental constants may exhibit variations and he postulated that this may occur on timescales comparable to the age of the Universe [7]. Since this time, many searches [8] [9] [10] [11] have been undertaken to look for time-dependence, on various time scales, of fundamental constants such as the fine structure constant (α_{EM}), the gravitational constant (G), the proton-to-electron mass ratio (m_p/m_e), and others. Since these constants play important roles in some of the most fundamental physical processes, their precise val-

ues often have significant consequences on the structure and evolution of the Universe as predicted within the SM. For example, a 4% change in the value of α_{EM} would prevent stellar fusion from producing carbon at sufficient levels for carbon-based life to exist in the Universe [12]. Similar fluctuations in other fundamental constants can lead to equally, if not more, catastrophic changes to the known universe.

It is important to briefly discuss the dimensionality of fundamental constants. Dimensional constants such as the speed of light c, the electron charge e, or Planck's constant $\hbar$, have values which depend on the definition of the unit system. In a sense they can be thought of merely as conversion factors from one unit system to another with no other intrinsic physical meaning. Dimensionless constants, on the other hand, like α_{EM}, arise in general from ratios between dimensional quantities and are not subject to the same limitations. For this reason, it is argued in [13] that the focus of searches for variations in fundamental constants should be constrained to dimensionless quantities only. This has been adhered to in many searches but some experiments have still focused on dimensional constants, such as G, by claiming that meaningful variations in such constants can still translate to meaningful variations in underlying dimensionless constants.

The Fine Structure Constant

The fine structure constant, which defines the strength of the electromagnetic interaction, can be written as [14]

$$\alpha_{EM} \equiv \frac{e^2}{4\pi\epsilon_0\hbar c} \approx 1/137.035\ 999\ 070(98) \tag{1.1.1}$$

where e is the elementary charge unit (or the charge of the electron), ϵ_0 is the permittivity of free space, and $\hbar$ is the reduced Planck constant. Electromagnetic interactions are responsible for nearly all of the phenomena experienced on a daily basis

and play a role in the largest and smallest of length scales. This force, and by extension the coupling constant associated with it, is responsible, in part or whole, for nuclear processes, atomic interactions, chemical reactions, material properties, stellar evolution, and more.

The question of the constancy of α_{EM} has been at the center of most studies into the constancy of fundamental constants. One of the first instances of testing this constancy was carried out by comparing spectral lines for colliding galaxies originating from Cygnus A against local values. This gave constraints on the relative change of α_{EM}, given by $\Delta\alpha_{EM}/\alpha_{EM}$, of $(1.8 \pm 1.6) \times 10^{-3}$ [15]. Another early study was able to give much more stringent limits by studying the Oklo Phenomenon, named after a pre-historic natural fission reactor located in the central African state of Gabon. By comparing capture cross sections, based on geochemical evidence, for nuclear processes occurring in Oklo 1.8 billion years ago to results from modern laboratory tests, an estimated of $(0 \pm 1.8) \times 10^{-8}$ was set in [16]. More recently, the Oklo Phenomena was used to claim a decrease in the values of α_{EM} given by $\Delta\alpha_{EM}/\alpha_{EM} > (4.5) \times 10^{-8}$ [17]. In addition to long term variations in the fine structure constant, recent experiments have also used the frequency ratio of Al^+ and Hg^+ in single-ion atomic clocks to set constraints on the present rate of change in α_{EM} as $|\dot{\alpha_{EM}}/\alpha_{EM}| = (-1.6 \pm 2.3) \times 10^{-17}$/year [18].

The Gravitational Constant

The relative weakness of the gravitational force compared to the other fundamental forces has made it extremely difficult both to measure the absolute value of G as well as any variations in it. Furthermore, as a dimensional constant, any variations in G can only meaningfully be considered under certain assumptions of constancy of other

variables (such as stellar masses). In this case, the variations in G could be attributed to variations in the more fundamental gravitational coupling constant given by

$$\alpha_G \equiv \frac{Gm_e^2}{\hbar c} \approx 1.7518 \times 10^{-45}, \tag{1.1.2}$$

where m_e is the electron rest mass. Since gravitation becomes more important at larger distance scales most of the experiments probing for variations in G rely on astrophysical or cosmological measurements. One of the first such experiments, carried out within the confines of the solar system, involved measuring radar-echo time delays between Earth and Mercury to set a limit on $|\dot{G}/G| < 4 \times 10^{10}$/year [19]. More recently, a study which claims to actually measure the variation in α_g by comparing luminosity distances of galaxies based on type Ia supernovae, set a limit on $|\dot{G}/G| < 1 \times 10^{10}$/year over 9×10^9 years [20].

The Electron-Proton Mass Ratio

The ratio of the mass of the electron to the mass of the proton is often denoted by

$$\mu \equiv \frac{m_e}{m_p} \approx 5.44617 \times 10^{-4}, \tag{1.1.3}$$

Since the proton is a constituent of baryonic matter, which is composed of quarks, while the electron is a constituent of leptonic matter, this quantity can be related to the quantum chromodynamical scale which governs the theory of the strong interactions. It has been proposed that the quantum chromodynamical scale may have varied faster over the lifetime of the Universe than the quantum electrodynamical scale so that μ may have undergone larger variations than α_{EM}. Just as with α_{EM}, most of the searches for variations in μ have focused around astrophysical or cosmological measurements.

One of the earliest such measurements was based on the agreement between redshift values measured from quasar absorption spectra. If μ varies with the scale of the Universe an additional redshift, Δz, for hydrogen lines in these absorption spectra is introduced which can be used to estimate the variation in μ. This technique was used to set limits of $\Delta\mu/\mu = (0 \pm 4) \times 10^{-1}$ for redshifts between $z = 2.1$ and $z = 2.7$ [21]. This method has since been used with increasing precision to set stricter limits on variations of μ. A more recent study based on methanol transition lines set limits of $\Delta\mu/\mu = (0 \pm 1) \times 10^{-7}$ at redshift $z = 0.89$ [22].

It should be noted that results at different redshift values may be model dependent and thus mutually exclusive. This means that, for example, results which are consistent with no change in μ at low redshift cannot exclude the possibility of a variation in μ at higher redshift values.

The Weak Coupling Constant

Since the focus of this work is to look for variations in nuclear decays involving both β and $\beta\beta$ transitions, it should be noted that such decays can be sensitive to variations in both α_{EM} and the corresponding "weak structure constant" given by

$$\alpha_W \equiv \frac{G_F m_p^2 c}{\hbar^3}. \tag{1.1.4}$$

Here G_F is the Fermi constant which will be discussed in more detail in later sections on nuclear decays. Variations in α_{EM} have been constrained to limits which are better than what is achievable with nuclear beta decay studies alone. Variations in α_W however have been constrained both from β decays [23] and studies of the Oklo natural reactors [24].

It can be shown [25] that all β decays rates are proportional to α_W^2 which implies that constraints depend on the combination $\alpha_{EM}^s \alpha_W^2$ where $s \equiv \frac{d \ln \lambda}{d \ln \alpha}$ is a measure

of the sensitivity of an α decay rate λ on α_{EM}. By comparing different nuclei, a constraint can be set on the variation of α_{EM} alone which can then be translated to a constraint on the variation of α_W. This was done comparing the ratio of decay rates in ${}^{187}_{75}Re$ and ${}^{40}_{19}K$ which gave $|\Delta\alpha_{EM}/\alpha_{EM}| < 2 \times 10^{-5}$ and thus $|\Delta\alpha_W/\alpha_W| < 10^{-1}$ over the last 10^9 years [26]. Data from the Oklo phenomenon was used to further refine constraints of the variation in α_W. Estimates of the weak interaction's contribution to the ground state energy of the primary isotope used in Oklo analyses give an estimate of $|\Delta\alpha_W/\alpha_W| < 2 \times 10^{-2}$ over 1.8×10^9 years [27].

1.2 New Physics Interactions

Another possible cause for temporal variations either in physics processes or the underlying constant governing them is a BSM interaction. A common example is dark matter and dark energy, which constitute exotic forms of matter and energy, that are known to make up large portions of the energy density of the Universe. Since so little is known about these phenomena, it has been postulated that new interactions may exist between these BSM phenomena and typical SM processes or constants. For example, quintessence models of dark energy theorize that the potential energy of a new dynamical field is responsible for the acceleration of the scale factor of the Universe. One potential piece of evidence for this model has been suggested to take the form of variations in the fundamental constants [28]. Similarly, dark matter has also been proposed as a source of cosmological evolution of the fundamental constants. Just as in the case of dark energy predictions, this would be due to a newly proposed scalar field which can couple very weakly to SM particles [29].

Yet another possibility for new interactions may lie just beyond the SM. It is possible that well established SM constituents, such as neutrinos, might interact in novel

ways to produce interesting variations in known physical processes. Neutrinos are the least understood members of the SM and, in fact, they have already demonstrated the need for BSM models. The phenomenon of neutrino oscillation, in which neutrinos can change from one leptonic flavor to another as they propagate, has shown that neutrinos must be massive particles [30]. This contradicts the SM framework in which neutrinos are considered to be massless particles. The possible relationship between neutrinos and variations of physical processes will be discussed further in the next section.

Chapter Two: Nuclear Decays

One of the possible ways to observe variations in fundamental constants (or BSM physics interactions which alter these constants) is by observing nuclear decays. Nuclear decay is the process by which an unstable nucleus of an atom can spontaneously release matter and/or energy, the type of which determines the type of decay, in an attempt to reach a more stable configuration. If the resultant nucleus is of a different element altogether (via a change in the number of protons) the process is known as nuclear transmutation. The most common of these decays are alpha (α) decays and beta (β) decays. By contrast there are also decays which don't result in transmutation, the most common of which is gamma (γ) decay. The full suite of possible decay channels extends quite far beyond these most common three and is due to the various interactions that a nucleus can undergo to change its total energy state. The strong, weak, and electromagnetic forces all play roles in determining the various nuclear states and the available transitions between them.

This chapter will begin with a brief introduction to nuclear decay processes with a focus on β decays. The section after then introduces the experimentally measurable decay rate and also deals with current claims for (and objections to) periodically varying nuclear decay rates. Searching for periodic modulations in nuclear decay rates is then discussed in the context of the NEMO-3 experiment.

2.1 History of Radioactivity

The discovery of radioactivity is attributed to Henri Becquerel [31] who, in 1896, was trying to study the recently discovered x-rays using naturally fluorescent minerals. Becquerel exposed potassium uranyl double sulfate salts to sunlight, believing that they were in fact absorbing and re-emitting the incoming sunlight as x-rays, and then placed them on photographic plates wrapped in thick black paper (to prevent direct activation by the sunlight). In one particular experiment, a cloudy day precluded sufficient sunlight for Becquerel's test and he decided to store his experimental setup in a dark drawer for a number of days. Becquerel decided to develop the photographs from this experiment nonetheless, expecting only the weakest of an image. To his amazement, the photographs showed, quite to the contrary, very vivid images leading Becquerel to postulate the existence of a new phenomena, known now as radioactivity.

Further experiments by Becquerel and his contemporaries established the various properties of these radioactive emissions. The names alpha, beta, and gamma were given to the first discovered forms of radiation according to their ability to penetrate matter (alphas as the least penetrating and gammas as the most). By subjecting radioactive isotopes to strong magnetic fields, the charges and masses of these radiations could be measured. This lead to a flurry of research in the emerging field of nuclear physics.

2.2 Types of Nuclear Decay

The precise decay process that an atom will undergo depends in large part on the composition of its nucleus. The interplay between the various forces trying to hold the atom together can lead to complex structures which are unstable to various competing

decay channels. This means that a single isotope can decay through a number of processes each with different probabilities. Furthermore, the initial decay may not sufficiently reduce the excess nuclear energy, requiring a successive decay in order reach a more stable ground state (this is often the case for γ decays which tend to accompany other decay modes and are rarely seen in isolation).

The main contributor to nuclear instabilities is the binding energy of the nucleons. For the most part, this is determined by quantum chromodynamics (QCD), which is the theoretical framework for describing the strong interaction which governs the quarks and gluons comprising all nucleons. One of the more general properties arising from QCD is the prediction that nuclei will tend to be more stable with an equal number of protons and neutrons but this simple model begins to deviate from reality fairly quickly with increasing atomic number Z. Nonetheless, a common rule that is generally obeyed is that neutron-rich nuclei tend to decay via β decay while proton-rich nuclei tend to favor decay by α emission.

Beta Decay

The type of decay that Becquerel first observed in 1896 was β decay. Subsequent studies by Becquerel in 1900 [32] measured the charge to mass ratio (e/m) of the beta particles to demonstrate that they were in fact electrons. The following year, it was shown that beta decays transmute the parent nuclei into that of a different element. The most puzzling aspect of beta decays however was the issue of its energy spectrum. In 1914 James Chadwick [33] demonstrated that the energy of outgoing beta particles followed a continuous distribution from the Q-value of the decay (representing the maximal energy transfer of the decay) all the way down to nearly zero. In alpha and gamma decay, the outgoing particles always carry away energy at discrete values

nearly equal to the change in energy between the initial and final nuclear states. In addition to the apparent violation of the conservation of energy, beta decays also violated the conservation of angular momentum in that the outgoing electron, which is a spin 1/2 particle, could not conserve the total angular momentum change of the nucleus alone. The solution to this conundrum was proposed in 1930 in a now famous letter authored by Wolfgang Pauli (translated in [34]). Pauli postulated the existence of a "neutron" which resided in the nucleus and was also emitted but undetected so that it carried away the remaining energy and angular momentum to balance the problem. In 1934 Enrico Fermi published a landmark paper [35] in which he formulated a theory of beta decay in which the beta and "neutrino" particles (renamed from neutron after Chadwick's discovery of the true neutron in 1932) were created within the nucleus. Fermi's neutrino was postulated to be a spin 1/2 particle with very low mass and very weak interactions and because of this it wasn't discovered until 1956 by Clyde Cowan and Frederick Reines [37].

Beta decay, in the most general sense, is a broad term for a variety of transmutative processes mediated by the weak force. The most common is β^--decay, in which a neutron is transformed into a proton by emitting an electron and electron-type anti-neutrino. A symmetric process called β^+-decay occurs when a proton is transformed into a neutron by emitting a positron and electron-type neutrino. Since the neutron is a more massive particle than the proton, β^--decays are much more common. By contrast, β^+ decays can only occur when the nucleus already has some excess of energy that it can use to make up for the mass difference between the neutron and proton. This results in β^+-decays being mostly relegated to nuclei that begin in some type of excited state as a result of a previous decay. Lastly, there is the process known as electron capture, often called inverse beta decay, which occurs when an

atomic nucleus captures and electron from one of its orbital shells and uses it to convert a proton into a neutron. It can occur in any case where β^+-decay is allowed and can even be the sole decay mode when β^+ is energetically unfavorable. In such a process the only outgoing decay product is an electron-type neutrino but since the orbital electron that is consumed in the process leaves an empty valence hole, higher lying electrons can cascade in often resulting in the emission of subsequent low energy X-rays or Auger electrons.

All beta decays processes are transmutative as they change the number of protons in a nucleus resulting in a different element after the decay. The nuclear equations for each process are:

$$(A, Z) \rightarrow (A, Z+1) + e^- + \bar{\nu}_e \qquad \beta^- \text{ decay} \tag{2.2.1}$$

$$(A, Z) \rightarrow (A, Z-1) + e^+ + \nu_e \qquad \beta^+ \text{ decay} \tag{2.2.2}$$

$$(A, Z) + e^- \rightarrow (A, Z-1) + \nu_e \qquad \text{electron capture} \tag{2.2.3}$$

Here A represents the mass number of the nucleus and Z represents the atomic number (or number of protons) and the parent nucleus appears on the left while the resultant daughter nucleus appears on the right.

In Fermi's theory of beta decay, based on Pauli's neutrino hypothesis, he approached the problem by treating the decay-inducing interaction (between the four fermions - proton, neutron, electron and neutrino) as a weak perturbation to estimate the transition rate as

$$\lambda = \frac{2\pi}{\hbar} |V_{fi}^2| \rho(E_f). \tag{2.2.4}$$

This approach is called Fermi's Golden Rule. Here $\rho(E_f) = \frac{dn}{dE_f}$ is the density of final states and V_{fi} represents the matrix element connecting the initial and final states

which can be expressed as

$$V_{fi} = \int \psi_f^* V \psi_i d\tau = g M_{fi} \tag{2.2.5}$$

where g represents the strength of the interaction (now referred to as the weak interaction). This was in essence a precursor to the true theory for weak interactions which would be treated via exchanges of W and Z bosons but it still captured the dependence of beta decays on the strength of the new force. This is why studies of beta decay rates over time can reveal to what degree this fundamental coupling constant can vary.

Double Beta Decay

Beta decay results in the loss of nuclear energy via the creation of new particles (electrons and/or neutrinos) thus it requires that the mass of the parent nucleus exceed that of the daughter nucleus ($M(A, Z_{initial}) > M(A, Z_{final})$). To predict whether a transition can occur then it is necessary to estimate the masses of each nucleus. This is done using the semi-empirical mass formula (SEMF) [38] given by

$$M(A, Z) = Z m_p + (A - Z) m_n + \frac{E_B}{c^2} \tag{2.2.6}$$

where

$$E_B = a_V A - a_S A^{2/3} - a_C \frac{Z^2}{A^{1/3}} - a_A \frac{(A - 2Z)^2}{A} \pm \delta(A, Z), \tag{2.2.7}$$

and

$$\delta(A, Z) = \begin{cases} \frac{+a_P}{A^{1/2}}, & \text{if A even (Z even),} \\ 0, & \text{if A odd,} \\ \frac{-a_P}{A^{1/2}}, & \text{if A even (Z odd).} \end{cases} \tag{2.2.8}$$

The first two terms in the SEMF simply give the contributions of the number of protons and neutrons to the total mass. The third term is a correction related to the binding energy of the nucleus. Here the coefficients a_V, a_S, a_C, and a_A are empirically determined and correspond to different underlying physics mechanisms that contribute to this total binding energy. Considering fixed values of A (as is the case in β decays) the SEMF predicts parabolic mass curves as a function of Z. These curves are used to indicate which β decays are energetically favorable by comparing the masses of nuclei. Due to the final term in E_B, only one parabola will exist for odd values of A but two possible curves exist for even values of A even: One for even-even nuclei (even number of protons and neutrons) and one for odd-odd nuclei. This is illustrated in figure 2.1.

For some unstable nuclei, the process of β^- decay, which increases Z by one unit, would result in a nucleus of higher mass value (for example if the nucleus at position (c) transitioned to that at position (d) on the mass parabolas). In this case it is energetically unfavorable and β^- decay strongly suppressed. This occurs only for doubly even nuclei (those with even number of both protons and neutrons). An alternative decay channel for such nuclei is to undergo two simultaneous β decays (transitioning to point (e) on the mass parabolas) wherein two neutrons transform in to a pair of protons while emitting two electrons and two electron-type anti-neutrinos. The corresponding nuclear equation to describe this is given by

$$(A, Z) \rightarrow (A, Z + 2) + 2e^- + 2\bar{\nu}_e. \tag{2.2.9}$$

Just as with β decays, a complementary process can also occur via positron emission instead. For these so-called $\beta^+\beta^+$ decays, the process follows

$$(A, Z) \rightarrow (A, Z - 2) + 2e^+ + 2\nu_e. \tag{2.2.10}$$

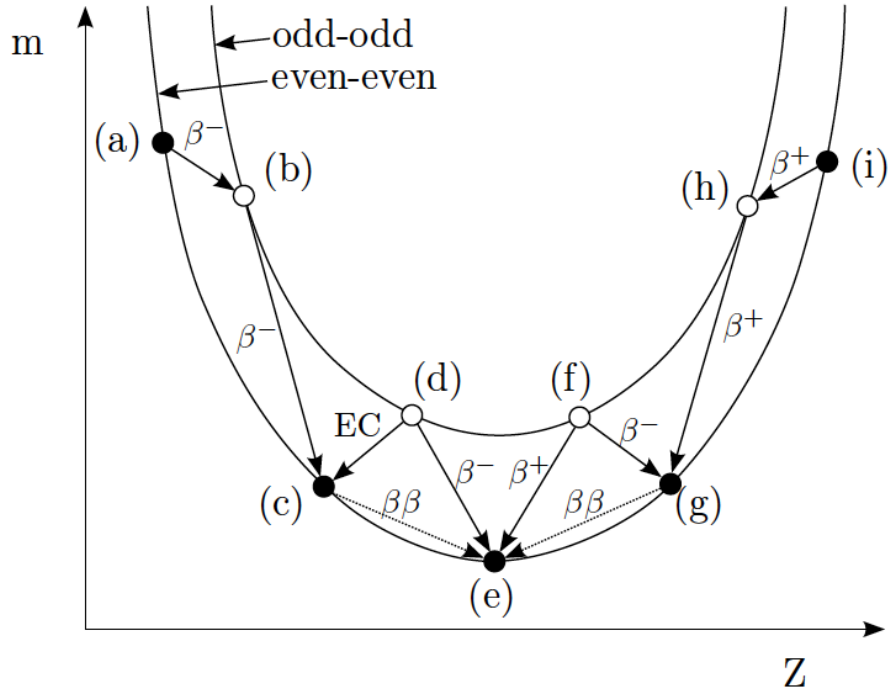

Figure 2.1: Predicted nuclear mass values, m, from the SEMF as a function of Z for a constant value of A (Specifically for the case where A is even). Letters point on the two parabola represent different nuclei while the arrows connecting them represent different allowable decay mechanisms.

This process, $2\nu\beta\beta$ decay, was first hypothesized by Maria Goeppert-Meyer in 1935 [39] on the basis of Fermi's theory of β decay. Following in Fermi's footstep, she calculated the transition rates as a second order weak perturbation. It is entirely consistent within the SM as it consists only of allowable SM vertices. In 1937 Ettore Majorana demonstrated [40] that the conclusions of β -decays remain unchanged if the neutrino is its own antiparticle ($\nu = \bar{\nu}$). This led Wendell H. Furry to propose [41], in 1939, the possibility of a BSM double beta decay process without the emission of any neutrinos. This process is now referred to as neutrinoless double beta decay and can be expressed (for either electron or positron emission) via

$$(A, Z) \rightarrow (A, Z + 2) + 2e^{\pm}. \tag{2.2.11}$$

One of the most important implications of this process, beyond proving that neutrino's are Majorana particles, is that it could be used to directly probe the neutrino mass scale since the decay rate for this process, unlike the SM $2\nu\beta\beta$ process, is proportional to the so-called Majorana mass of the neutrino. Since the search for this process is not the focus of the analysis presented herein, the reader is referred to other sources for a more complete explanation of $0\nu\beta\beta$ decays [42].

2.3 Nuclear Decay Rates

Regardless of which type of nuclear decay occurs, the process is stochastic meaning that it is impossible to predict when a particular unstable atom will decay. Each atom has the same probability of decaying at any given time. This implies that, given a sample of N atoms of a particular isotope that can undergo any nuclear decay, the rate at which the decay process occurs is proportional to the number of atoms present. If the activity, A, is defined as the number of decay events, dN, that occur in a time interval, dt, then

$$A = \frac{-dN}{dt} = \lambda N, \tag{2.3.1}$$

where λ is a proportionality constant and the negative sign denotes that the number of atoms of a given isotope decreases over time as more decays occur. This simple differential relation can be solved to yield the familiar nuclear decay equation for the number of un-decayed atoms as a function of time,

$$N(t) = N_0 \exp(-\lambda t), \tag{2.3.2}$$

where N_0 represent the initial number of atoms of a given isotope in the sample, and it can be seen now that λ represents the rate at which the decay process occurs. A more commonly used metric for comparing decay rates is the half-life, normally

written as $T_{1/2}$, which is the time it takes for half of the sample to decay, on average. It is related to the decay constant λ by

$$T_{1/2} = \frac{\ln(2)}{\lambda}. \tag{2.3.3}$$

Half-life values have no known upper or lower limits and span a wide range of values over many orders of magnitudes. Some isotopes have nuclei which tend to exist for tiny fractions of a second while others have nuclei with lifetimes much longer than the age of the universe.

The exponential-decay law, as expression 2.3.2 is often called, was established in the earliest days of research into nuclear decays by Ernest Rutherford [44], Marie Curie [45], and others. It has long been regarded as one of the most famous in all of physics for it implies that nuclear decay rates depend entirely and solely on a single time constant that is intrinsic to each nucleus. Various experiments [46] [47] [48] [51] have tried to search for deviations from the exponential nature of nuclear decay rates by subjecting nuclei to various external influences such as temeprature variations, extreme pressure differences, strong magnetic fields, different chemical states, and more. All results for alpha and beta decays have shown no signifianct perturbations when such variables were changed. Only for decays in which the atomic electrons play a role, specifically those such as electron capture and internal conversion, have exhibited changes in the decay rates when certain external conditions were manipulated [49] [50].

Recently, new claims [52] [53] [54] [55] [56] [57] [58] [59] [60] have now brought the the hallowed decay law back into the spotlight of new controversy. These assertions purport to have evidence for new perturbations in decay rates cause by an as-yet-unknown external influence. In particular many of these claims suggest a connection to solar processes since the modulations detected have been periodic in nature and

with frequencies that correspond well with things such as Earth-Sun dustance of synodic solar rotation rates. Naturally the topic has been highly contested [61] [62] [63] [64] [65] [66] [67] as many have tried to replicate the results in different isotopes and using different detection techniques. One common issue at the heart of this debate has centered on the issue of detector or instrument stability meaning that authors of such claims have been careful to ensure that the results properly account for such systematic effects.

The authors of [52] obtained data from two separate direct counting experiments: the first at Brookhaven National Laboratory (BNL) which observed ^{32}Si undergoing beta decay and the second from Physikalisch-TechnischeiBundesandstalt (PTB) in Germany which observed ^{226}Ra undergoing alpha decay. The authors have noted in subsequent papers [4] that although ^{226}Ra is not a beta emitter (which is the primary decay type in which this claim is supported), it is present in a complicated decay chain which does include many beta emitting isotopes. Since the detector in the PTB experiment (an ionization chamber) could not discriminate between the two types of decay (alpha or beta), the effects of the beta decay could have been manifested in the overall ^{226}Ra data set. Both experiments had the desirable quality of providing data sets spanning multiple years, four for the BNL data and fifteen for the PTB data.

For both of these data sets the authors calculated the quantity:

$$U(t) \equiv [\dot{N}(t)/\dot{N}(0)] \exp(\lambda t), \tag{2.3.4}$$

Where $\dot{N} = dN/dt$ is the counting rate, or activity, for a given isotope and λ is the decay constant from equation 2.3.2. This facilitates the comparison of different isotopes since $U(t)$ should be time-independent for all nuclides. One further detail is

that for ^{32}Si the function $U(t)$ was in fact constructed using the ratio

$$^{32}Si/^{36}Cl \equiv \dot{N}(^{32}Si)/\dot{N}(^{36}Cl), \tag{2.3.5}$$

because ^{36}Cl has a much longer half-life and was therefore useful to cancel out systematic detector effects that might appear in the ^{32}Si rate. The plots taken from [52], shown in figures 2.2 and 2.3 for the BNL and PTB data respectively, illustrate this function versus time along with an overlay of the inverse square of the Earth-Sun distance, $1/R^2$, in units of $1/(a.u.)^2$) for the corresponding times.

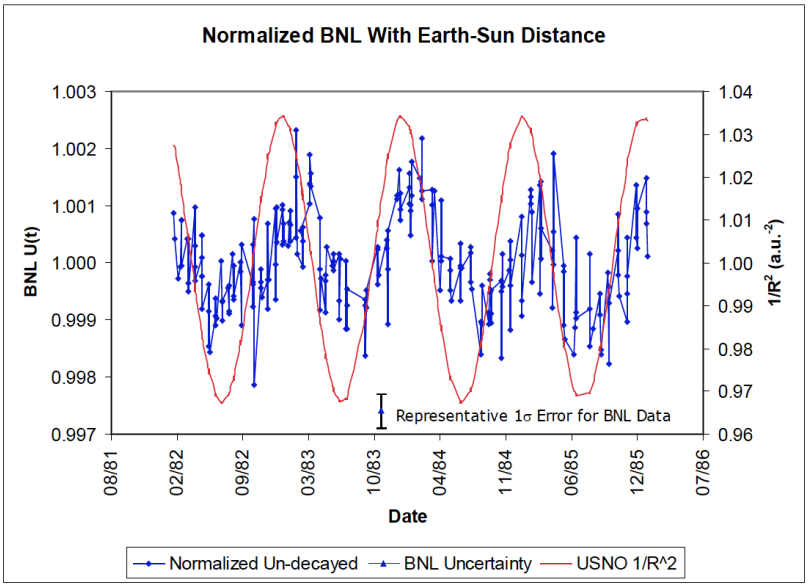

Figure 2.2: Plot of $U(t)$ for the raw BNL ^{32}Si /^{36}Cl ratio along with $1/R^2$ where R is the Earth-Sun Distance in units of $1/(a.u.)^2$. The scale on the left corresponds to $U(t)$ where as the one on the right corresponds to $1/R^2$.

A modulation of relative amplitude of about 0.1% is claimed with a period of nearly one year is claimed in both data sets with Pearson correlation coefficients of $r = 0.52$, for 239 BNL data points, and $r = 0.66$, for 1968 PTB data points. These correspond to formal probabilities of 6×10^{-18} and 2×10^{-246}, for the BNL and PTB data respectively, that these correlations would arise by chance from two

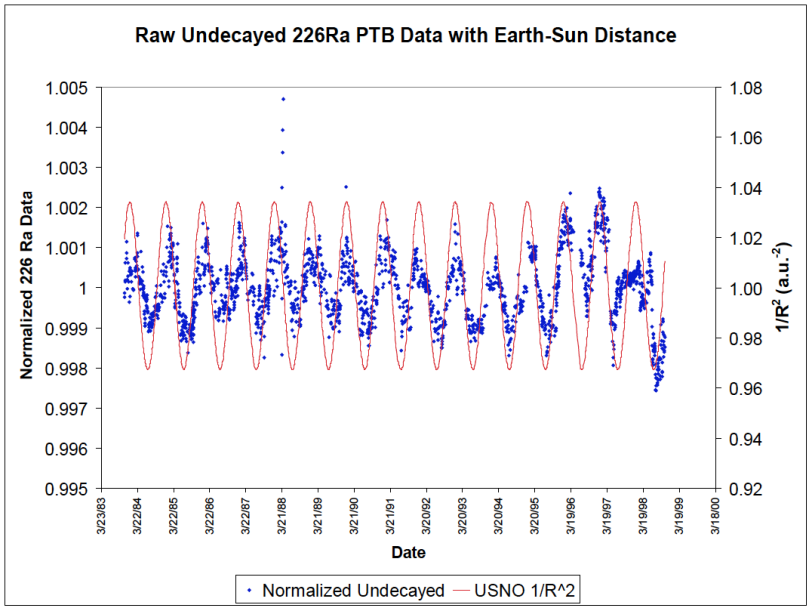

Figure 2.3: Plot of $U(t)$ for the raw PTB ^{226}Ra data (Note: a 5 pt. rolling average was applied in this case) along with $1/R^2$ where R is the Earth-Sun Distance.

uncorrelated data sets. Furthermore, the two data sets correlate with one another producing a Pearson correlation coefficient $r = 0.88$ with a formal probability of 4×10^{-12} that the BNL/PTB correlation could have arisen from uncorrelated data. The agreement between the two data sets is shown in figure 2.4.

The authors later revisited the BNL data and applied a more in depth power spectrum analysis [55] which involves tansforming a time series into the frequency domain to study its frequency spectral composition. If a time series shows evidence of a periodic modulation it will appear as a relatively large peak in the power spectrum at the corresponding frequency. This is precisely the technique which is employed in this work to search for periodicities in NEMO-3 decay rate data so the full details of this type of analysis will be revealed in chapter 5. Using this approach the authors scanned a frequency range between $10 - 15\,\mathrm{yrs}^{-1}$ to search for periodicities which might be related to solar synodic rotation rates. They find significant evidence for

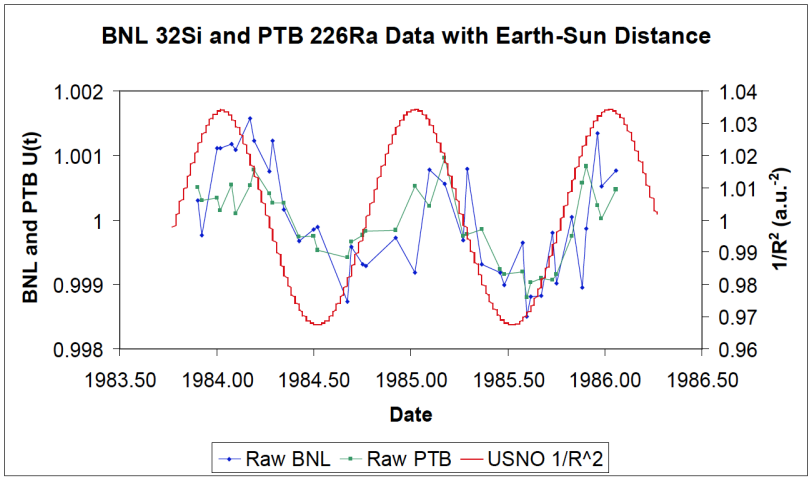

Figure 2.4: Plot of $U(t)$ for both the BNL and PTB data (averaged into common weekly bins for comparison purposes) spanning the two years during which the experiments overlapped.

modulations at 11.17 and 13.11 yrs^{-1} (see figure 2.5) which could be indicative of influences due to rotation of the solar core. The authors postulate that the solar neutrino flux, which can vary due to the solar core behavior, could be mediating an interaction with terrestrial nuclear decays.

2.4 Related Claims

In addition to the periodic modulations seen in nuclear decay rates, it has been noted by the authors in [52] that other experiments in different fields have also seen unexplained modulations in their data. In particular the authors note that the DAMA/LIBRA dark matter search experiment has shown evidence of an annual periodic modulation [68]. In [69] the authors of [52] reconstructed the DAMA data (from both the previous DAMA/NaI experiment and the most recent DAMA/LIBRA experiment) and applied a power spectrum analysis to the time series. In addition to the prviously claimed annual modulation they also find evidence of various new potential modula-

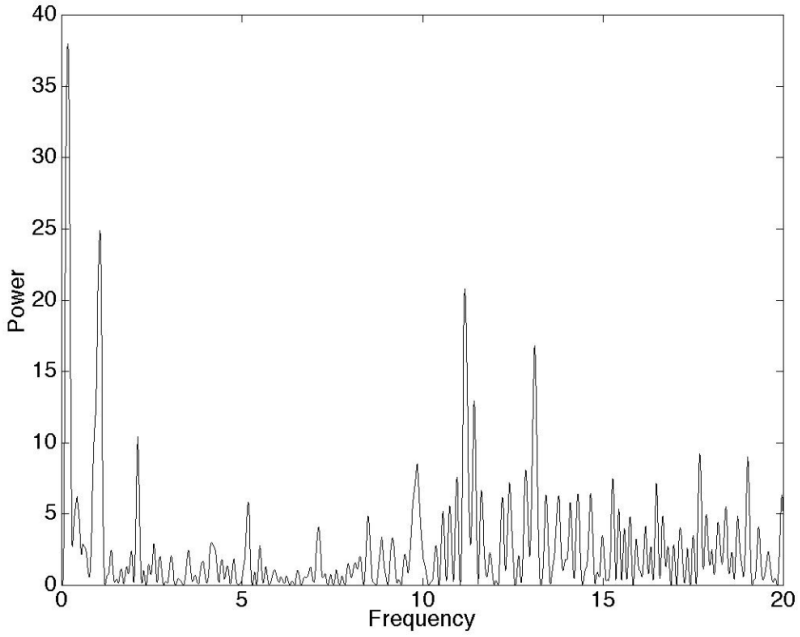

Figure 2.5: Power spectrum of the BNL time series of the ratio of ^{32}Si and ^{36}Cl decay rates. The largest peak at $0.17\,\mathrm{yrs}^{-1}$ is expected to be due to secular trends in the data. The peak near one corresponds to annual modulations. The next two largest peaks are those at 11.17 and $13.11\,\mathrm{yrs}^{-1}$.

tions in the frequency range of $11 - 13\,\mathrm{yrs}^{-1}$, one of which at $11.44\,\mathrm{yrs}^{-1}$ is present prominently in the DAMA/NaI data (but not the DAMA/LIBRA data). The two power spectra corresponding to each data set are shown in figures 2.6 and 2.7.

In order to further illustrate the possible solar origins of these modulations in terrestrial measurements the authors also analyzed solar neutrino flux data from the Super-Kamiokande neutrino observatory [70]. In doing so they once again found evidence for periodicities in a similar frequency range. Using 5 years worth of flux data, evidence is found for periodicities near 9.5 and $12.5\,\mathrm{yrs}^{-1}$ which again point to origins in the state of the deep solar interior. The corresponding power spectrum is shown in figure 2.8. The authors raise the possibility that the all of the above measurements may be lined such that the DAMA results and the variation in nuclear decays are all influenced by the same phenomena with possible origins in solar neutrinos, cosmic

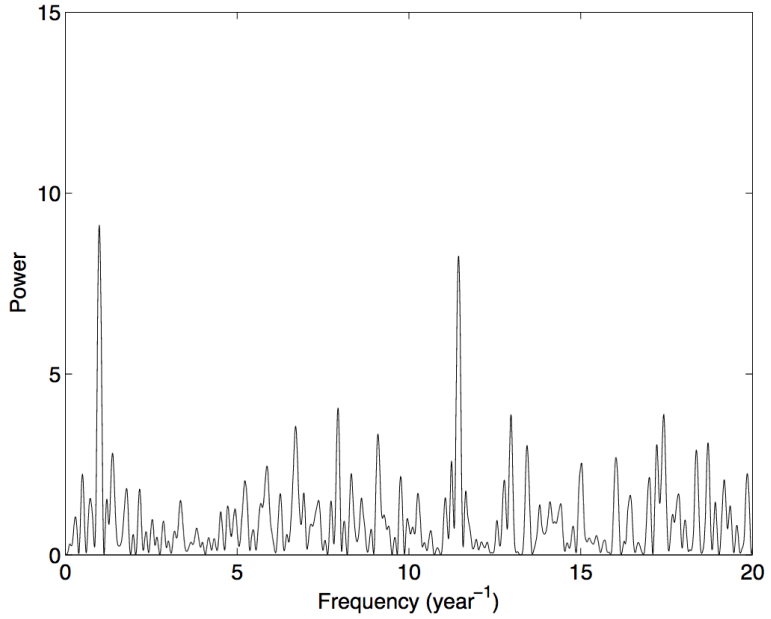

Figure 2.6: Power spectrum of the DAMA/NaI data. Aside from the clear annual modulation peak, the next largest peak is at $11.47\,\mathrm{yrs}^{-1}$ which does fall in the range of possible solar influence.

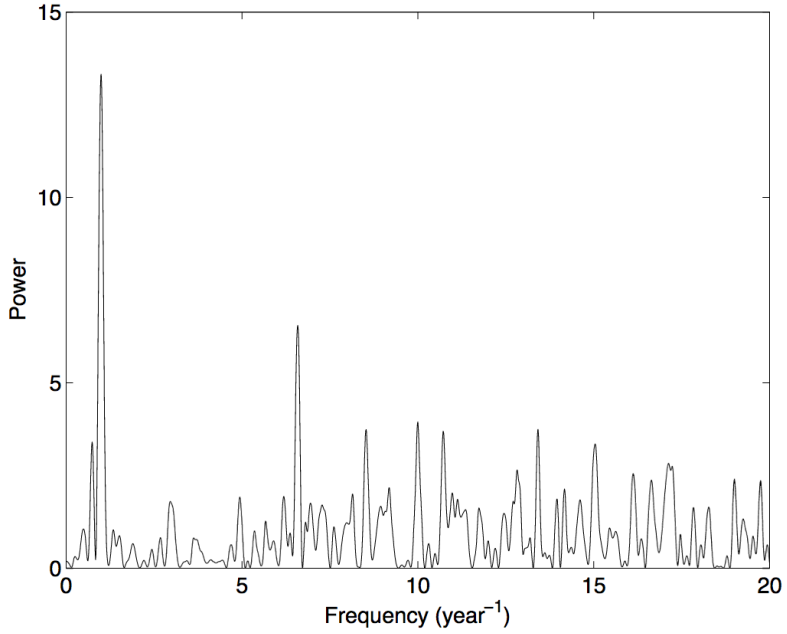

Figure 2.7: Power spectrum of the DAMA/LIBRA data. Aside from the clear annual modulation peak, the next largest peak is at $6.7\,\mathrm{yrs}^{-1}$ and does not have an obvious relationship to known solar periodicities.

neutrinos, dark matter, or a combination of the them all.

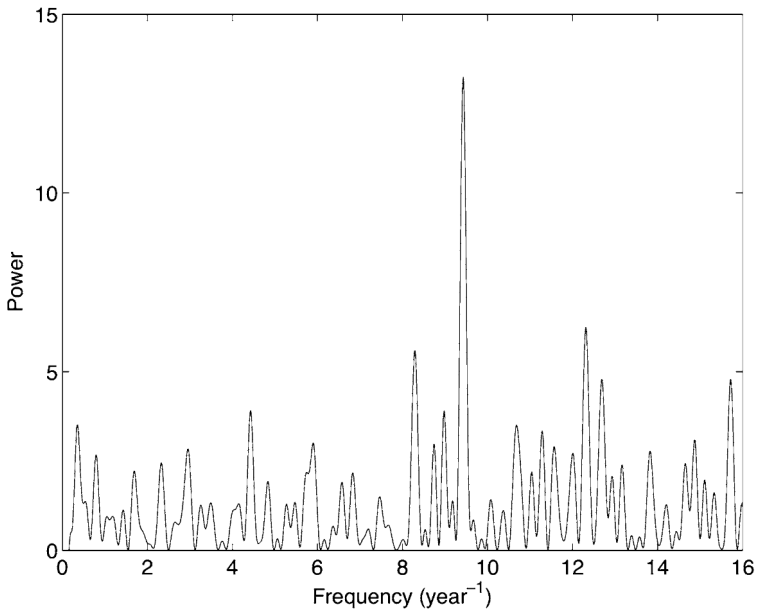

Figure 2.8: Power spectrum of the Super-Kamiokande solar neutrino flux time series. The largest peaks are at 9.5 and 12.5 yrs^{-1}.

Chapter Three: The NEMO-3 Detector

3.1 Detector Description

The NEMO-3 detector was designed with the philosophy of using multiple observables to directly detect the two electrons emitted in $\beta\beta$ decays. Unlike many other experiments where the source and detector are inextricably linked, NEMO-3 combined both tracking and calorimetric elements that were separate entities so that candidate $\beta\beta$ events could be distinguished from various backgrounds with high fidelity. It consisted of individual sectors that when combined formed a toroidal geometry in which the concentric inner and outer walls surrounded thin strips of the isotopic source foils. These walls were made up of plastic scintillator bricks coupled to low radioactivity photomultiplier tubes for energy and timing measurements. The volumes in between the source foils and calorimeter walls were instrumented with drift cells operated in Geiger mode to provide full three dimensional tracking information. To further aid in particle identification, a large solenoid encompassed the detector to produce a 25 Gauss magnetic field within the tracking volume. Finally, the entirety of the detector was further surrounded by various passive shielding elements to minimize influences from external backgrounds. NEMO-3 was built upon many years of experience from its predecessor, the NEMO-2 experiment, as well as an extensive research and development period to improve the detector in many key areas.

This chapter presents a detailed description of each of the main detector components as well as its auxiliary systems which are responsible for data acquisition, calibration, monitoring, and radio-purity. The general design and structure of the

detector is presented first as the frame for further discussions of each "layer" of the detector starting with the source foils in the center and moving outwards form there. An overview of the main calibration systems is then given. Lastly, the anti-radon facility is discussed.

3.2 General Design

The NEMO-3 detector was constructed in the Laboratoire Souterrain de Modane (or LSM) facility located deep within the Frèjus Mountain that sits on the border between France and Italy. It consisted of three distinct elements: the source foils, the tracking volume, and the calorimeter. The main principle behind any $\beta\beta$ decay detector is being able to detect and measure the energies of the two outgoing decay electrons. The distribution of the sum of the electron energies is the primary observable which is then fitted to determine the number of detected signal events and thus the half-life of the process. Unlike other detector approaches which combine the source and calorimeter elements for improved energy resolution, the NEMO approach focuses on observing many features of each decay event in order to drastically suppress most backgrounds. The result is a measured electron sum energy spectrum similar to that which is shown in figure 3.1.

Since $\beta\beta$ decays are so rare relative to the many background processes, such a distribution is only achievable with a detector that can accurately pinpoint on true $\beta\beta$ decay events. This is the driving goal that motivates the NEMO design which was embodied in the NEMO-3 detector.

The detector was subdivided into 20 equally sized wedges so that the $\beta\beta$ sources could vary from one wedge to another. A diagram of the near-fully assembled detector is shown in figure 3.2.

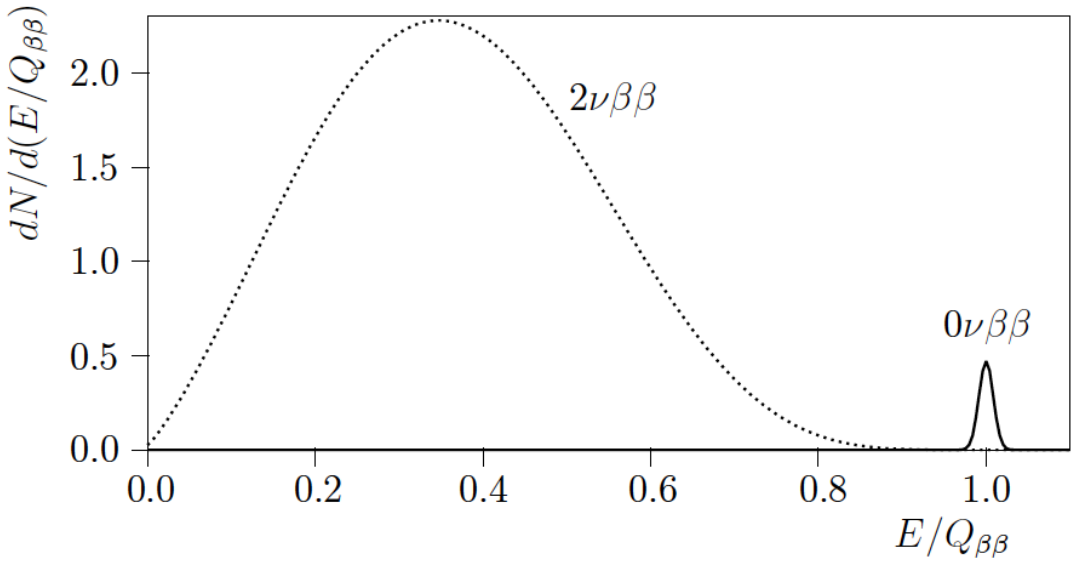

Figure 3.1: Distribution of the sum of the energies of the outgoing electrons from a ββ decay event in the case of both 0νββ and 2νββ processes. This illustration assumes that $T_{1/2}^{0\nu\beta\beta}$ is 1% of $T_{1/2}^{2\nu\beta\beta}$ and that the energy resolution of the detector is 2%.

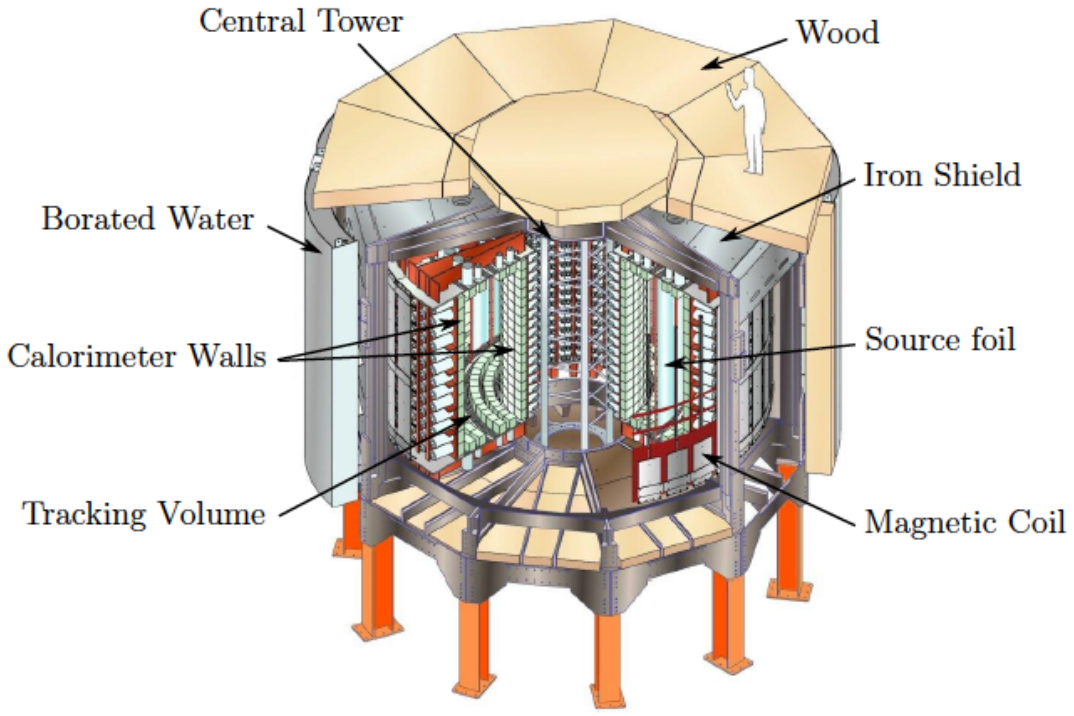

Figure 3.2: An illustration of the NEMO-3 Detector with a few sectors and some shielding cut away to reveal the interior.

Each wedge, or sector, followed the same design principles established in the NEMO-2 experiment of separating the source and detector and providing a rich data set of observables for each event. Since the calorimeter component could supply the detector with particle energy and timing measurements while the tracking component provided particle trajectory information, the NEMO-3 detector was able to discriminate between electrons, positrons, gammas, and alphas to aid in background measurement and suppression.

The source foils made up the heart of the detector and a total of approximately 10 kg of various isotopes was distributed into the 20 NEMO-3 sectors. These foils were designed to have a nominal thickness of 60 mg/cm^2 or less so that the detection efficiency for the $0\nu\beta\beta$ decay was not compromised by energy losses as the electrons exited the foils. All foils were installed vertically at the center of each sector leaving about 155 cm between either side of the foil and the corresponding calorimeter wall. In addition to the $\beta\beta$ isotopic foils, calibration foils made of high radio-purity copper and natural tellurium were also placed in the detector to measure the effects of external backgrounds on the foils.

The tracking volume surrounded the source foils and was made up of a total of 6,180 drift cells which were operated in Geiger mode to ensure robustness and minimize the complexity of readout electronics. Each cell was made using steel wires with a diameter of 50 µm and lengths of 270 cm. The tracking volume was filled with a gaseous mixture of helium, argon, ethyl alcohol, and water vapor.

The calorimeter which encompassed the tracking volume consisted of 1940 plastic scintillator blocks coupled to low radioactivity photomultiplier tubes (PMTs). These combined scintillator blocks and PMTs were known as optical modules (OMs) and hermetically covered both the inner and outer radii of each sector. In addition, there

were also a number of OMs which partially covered the iron plates, called petals, that sealed the top and bottom of each sector and provided structural support for the drift wire cells.

A large solenoid encircled the entire detector to produce a 25 Gauss magnetic field oriented parallel to the source foils. This field aided in particle charge discrimination and in the rejection of positrons. Further outwards and iron shield was used to limit the flux of γ-rays and thermal neutrons. Outside of the iron shielding were the primary neutron shielding elements whose main goal was to thermalize fast neutrons and suppress the thermal neutrons.

Finally, the last major element to the detector's design and overall shielding is its location within the Frèjus mountain. This provided an overburden of 4800 meters water equivalent for protection from cosmic-ray induced backgrounds. Measurements of the cosmic ray muon flux inside the LSM have yielded values of $5 \times 10^{-5}\,\mathrm{m}^{-2}\mathrm{s}^{-1}$ corresponding to a factor of one million reduction compared to sea level.

3.3 The Source Foils

One of the core design features of the NEMO technique, unique among $\beta\beta$ detectors, is the independence of the source and detector. This affords numerous advantages such as providing better background characterization and rejection, information on underlying decay mechanisms, and the ability to study multiple different $\beta\beta$ isotopes. This latter point is critical for cross checking any possible $0\nu\beta\beta$ signal in another isotope and reducing the dependence of the results on the hard-to-calculate nuclear matrix elements.

Each sector housed foils that were divided into seven strips that were on average 2480 mm long and 65 mm wide (63 mm if the strip was located at an outer edge of

the sector). Each strip was classified as either metallic or composite and had a mean surface density between 30 and 60 $\mathrm{mg/cm^2}$. This corresponded to a thickness less than 60 μm (density of about 10 $\mathrm{g/cm^3}$) for metallic strips and less than 300 μm (density of about 2 $\mathrm{g/cm^3}$) for composite strips. The primary difference between metallic and composite foils is the presence of an organic glue that is mixed with powdered isotopes to create the composite foils.

Isotope Selection

There are currently 41 known naturally occurring isotopes that can undergo $\beta\beta$ decay (35 of these decaying via $\beta^-\beta^-$ emission and the remaining six decaying via $\beta^+\beta^+$ emission). These isotopes vary from one to another in a number of key parameters that affect their utility in the search for $0\nu\beta\beta$ decay. These parameters include the energy of the $\beta\beta$ transition ($Q_{\beta\beta}$), the natural isotopic abundance, the values of its corresponding phase space ($G^{2\nu}$ and $G^{0\nu}$) and matrix ($M_{2\nu}$ and $M_{0\nu}$) elements, and the feasibility of enrichment and purification.

In NEMO-3 the $Q_{\beta\beta}$ value was one of the top considerations when choosing isotopes to observe since this determines the level of background contamination in the energy range where the search for $0\nu\beta\beta$ decay takes place. Of the three main chains of natural radioactivity (uranium, thorium, and actinium) the uranium and thorium present the largest problem due to the presence of ^{214}Bi and ^{208}Tl among their progenies. The ^{208}Tl in isotope in particular produces the highest energy naturally occurring γ-ray with energy 2615 keV. Above this energy the presence of background events due to natural radioactivity drops dramatically and so $Q_{\beta\beta}$ values above this are highly preferable. The energy spectrum for naturally occurring radiation is shown in figure 3.3.

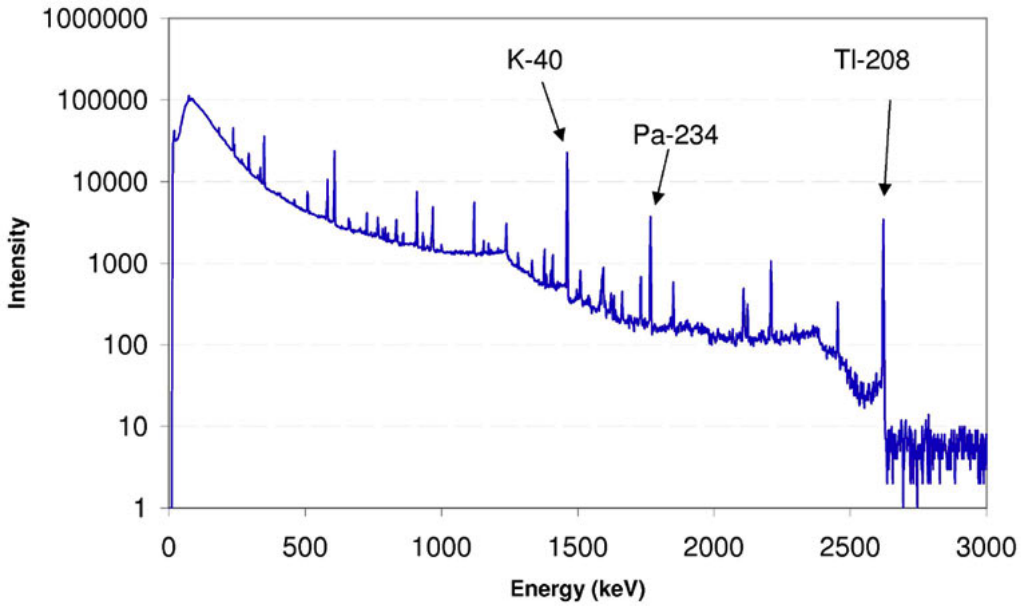

Figure 3.3: Spectrum of naturally occurring radioactive backgrounds. The sharp peak at 2615 keV followed by a sharp drop off in counts demonstrates the γ-ray line due to ^{208}Tl and the relative lack of background events above it.

The other top consideration in NEMO-3 isotope selection was the natural abundance for which a value of 2% or greater was desired. In general the higher this value, the easier the enrichment was for the isotope. Of the 35 $\beta\beta$ isotopes that exist, only five were able to satisfy these two selection criteria. In addition, two more isotopes were also selected for the NEMO-3 experiment. Despite its extremely low natural abundance, ^{48}Ca was included due to its very large $Q_{\beta\beta}$ value as well as improvements in enrichment techniques in Russia (where all sources were produced for NEMO-3) which made possible the production of a small sample for experiment. Lastly, ^{130}Te was included primarily to resolve a historical discrepancy between two incompatible geochemical half-life measurements [73] [74]. Table 3.1 summarizes the main selection parameters for the seven $\beta\beta$ isotopes that were used in NEMO-3 while figure 3.4 shows how the sources were distributed among the different sectors.

Isotope	$Q_{\beta\beta}$ [KeV]	Abundance [%]
^{48}Ca	4272.0±4.1	0.187
^{116}Cd	2804.7±4.2	7.5
^{100}Mo	3034.8±6.3	9.6
^{150}Nd	3367.1±4.9	5.6
^{82}Se	2995.2±3.3	9.2
^{130}Te	2528.8±2.1	33.8
^{96}Zr	3350.0±3.5	2.8

Table 3.1: Summary of the properties of $\beta\beta$ isotopes used in NEMO-3.

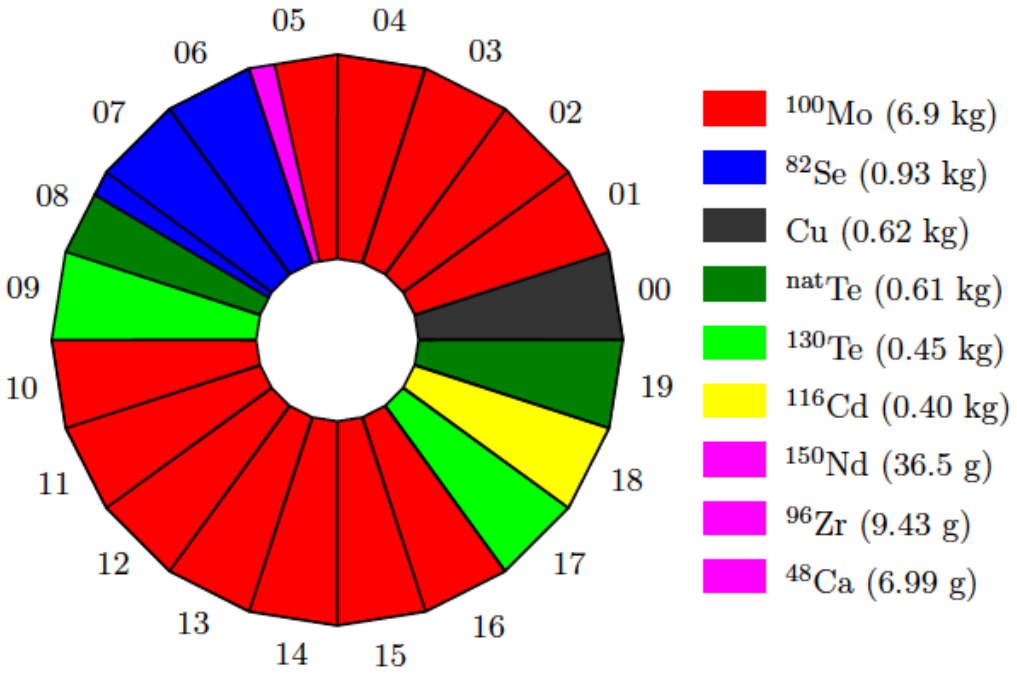

Figure 3.4: An illustration of the source distribution in the 20 sectors of NEMO-3.

Enrichment, Purification, and Foil Production

As indicated previously, the isotopic source foils in NEMO-3 were classified as either metallic (for cadmium, copper, and a fraction of molybdenum foils) or composite (for

tellurium, zirconium, calcium, neodymium, selenium, and the remaining molybdenum foils). The composite foils were created by mixing a powdered form of the desired isotope with an organic glue made of water and PVA (polyvinyl alcohol) and then sandwiching this mixture in between two specially prepared sheets of thin mylar (called backing film). All components were screened using HPGe detector to ensure high levels of radio-purity.

Since each selected isotope varied in terms of their chemical and physical properties and naturally occurred in different abundances, different procedures were used to enrich and purify each sample. Since a major focus of this document is on the $\beta\beta$ of ^{100}Mo , more details on the enrichment and purification are presented in the next section for this particular isotope.

^{100}Mo Production

As with all sources produced for NEMO-3, enrichment of ^{100}Mo , which has a natural abundance of 9.6%, was handled by the Institute for Theoretical and Experimental Physics (ITEP) in Moscow, Russia. The process began with the formation of MoF_6 gas using natural Mo. This was then centrifuged to seperate out heavier isotopes including ^{100}Mo . An oxidation reduction reaction then transformed the enriched $^{100}MoF_6$ gas into $^{100}MoO_3$ which was then processesed into ^{100}Mo metallic powder. Two samples totalling 10 kg were created with enrichment levels of $95.14 \pm 0.05\%$ and $98.95 \pm 0.05\%$. The enriched ^{100}Mo powder then underwent different purification and fabrication processes to create the two different types of foil strips.

Metallic Foils

The enriched ^{100}Mo powder was first pressed into solid ^{100}Mo samples. These samples were melted under vacuum to create a liquid from which monocrystals could be drawn. Impurities from long-lived natural radioactive isotopes (uranium, thorium, and radium) would migrate to the surface of these monocrystals and the "skin" of each crystal could then be physically removed via cutting the samples. When repeated multiple times, this produced very pure final crystal samples which were heated and rolled in a vaccuum and then cut into strips that made up the foils. These strips are used in sectors 02, 03, and 04 as well as partially in sectors 01 and 05 and represent in total $2479 \pm 5\,\mathrm{g}$ of the ^{100}Mo used in NEMO-3.

Composite Foils

The composite foils also begin using the same enriched metallic ^{100}Mo powder but undergo chemical purification to remove unwanted radio-isotopes. This process starts with a solution containing the enriched powder, ultra pure water, quartz distilled HNO_3, and a small amount of pure $Ba(NO_3)_2$ salt. This solution is heated until the Mo powder dissolves and the heat is then further increased to raise the acidity while lowering the volume. This cause the Mo to precipitate as MoO_3. At this stage the role of the baryum salt is important in blocking sites on the MoO_3 that would otherwise carry Ra. After this, the acid soluble-impurities are filtered from the MoO_3 resulting in a filter cake that was then rinsed and dried and heated in a furnace. This heating was done in two stages: the first stage was with He at 200 °C to further dry the MoO_3 while the second stage was done with H_2 at 850 °C to reduce the MoO_3 back into pure metal powder with less than 2% O_2.

In preparation for mixing with the organic glue used in composite foils, the powder

was first passed through a sieve which accepted grain sizes of 45ñm or less. This ensured a good bond between the powder and the glue and any leftover powder was ground up to be re-sieved to keep waste to a minimum. Next the powder was mixed with the glue, introduced into a syringe, and heated to create a paste which could be uniformly spread onto the surface of one of the mylar backing films. Once finished, another mylar backing film would be used to cover the first one. These backing films had been irradiated with an ion beam to create microscopic holes (about 0.4 μm in diameter) with a density of about $(2-7)\times 10^7$ holes/cm^2 which helped with bonding to the paste and with letting a foils dry. From this, strips were cut to length and installed in sectors 01, 05, and 10 - 16 with a total mass of 4435 ± 22 g.

Calibration Foils

As mentioned previously, an additional two foils were also installed in the detector to study external backgrounds. The first of these was ^{nat}Te which was chosen due to its similar Z-value compared to ^{100}Mo . Since external γ-ray induced event rates are proportional to Z^2, this should lead to similar background contributions in the ^{nat}Te and ^{100}Mo foils. Although ^{nat}Te still contains about 33% of ^{130}Te which can also undergo $\beta\beta$ decay, the $Q_{\beta\beta}$ value is low enough (2.53 MeV) so that the backgrounds are still comparable between the two isotopes in the region of interest for ^{100}Mo ($2.8-3.2$ MeV). A total of 614 g of ^{nat}Te were installed in sectors 08 and 19. The copper foil provides a similar estimation of external backgrounds but for lower Z-value isotopes. A total of 621 g was installed in sector 00.

3.4 The Tracking Volume

The 6,180 wire drift cells were distributed symmetrically into 18 total layers (nine on either side of the source foil). Each sector followed a "4-2-3" pattern meaning it had, on each side of the foil, four layers (each with 16 cells on the inner side or 18 on the outer) placed immediately next to the foil, followed by a gap, then another two layers (with 14 inner cells and 20 outer cells), followed again by a gap, and finally ending with the three layers (with 12 inner and 23 out cells) which were adjacent to the calorimeter walls. The gaps were used for the placement of additional calorimeter OMs affixed to the petals on the top and bottom of each sector. The higher density of cells near the foil was chosen to maximize the event vertex precision while the lower density layers further away from the foils were found to be sufficient for trajectory curvature measurements. This wire cell layout for any given sector is shown in figure 3.5. The next sections describe the elementary Geiger cells used in the tracking volume as well as the gas mixture employed.

Elementary Geiger Cells

Each wire cell in the tracking volume had an open octagonal cross section with a 3 cm diameter. A central anode wire was surrounded by eight ground wires which were shared between up to four adjacent cells to minimize the amount of wires and thus the potential for electron scattering. In addition, a ninth ground wire was also added between adjacent cells from different layers (but not adjacent cells within the same layer) to reduce electrostatic cross talk. This brought the number of wires in the tracking volume, including anode and ground wires, to 39,820 in total. An illustration of this basic cell is shown in figures 3.5 and 3.6.

All ground and anode wires were made from stainless steel and had diameters of

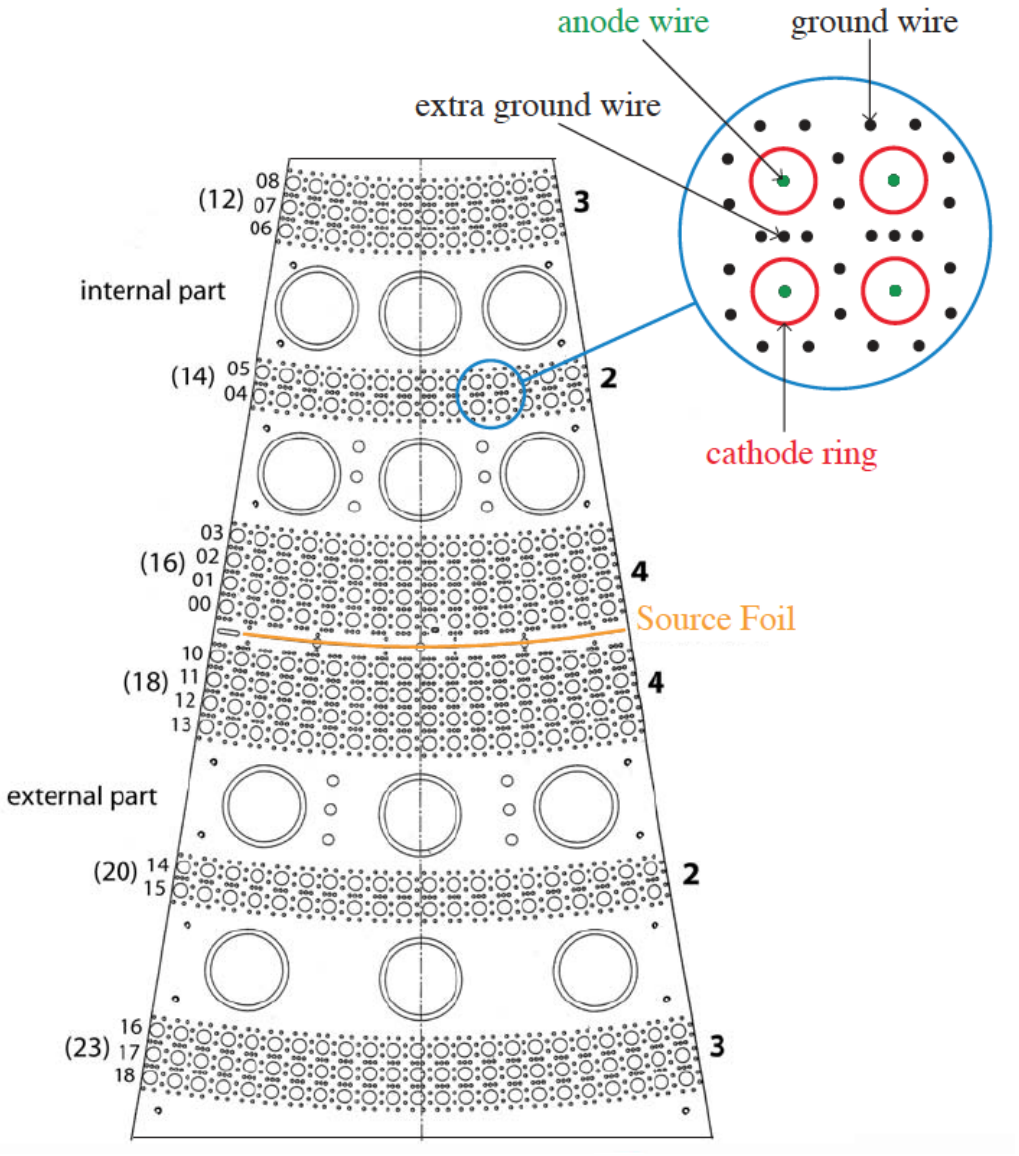

Figure 3.5: An illustration of the Geiger cell layout in a NEMO-3 sector. The large circles separating layers are for calorimeter modules attached to the petals.

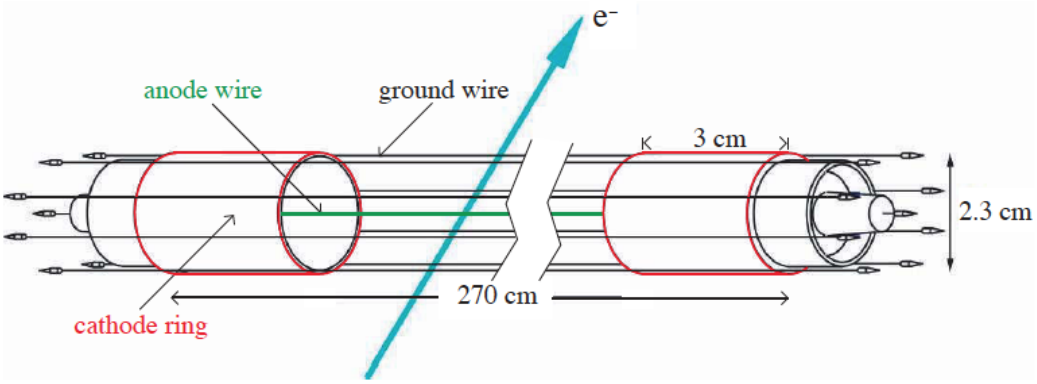

Figure 3.6: An illustration of an elementary Geiger cell used in the NEMO-3 tracking volume.

50 μm and lengths of 2.7 m. They were strung vertically and affixed to the iron petals that cap the tops and bottoms of each sector. Located at each end of a cell is a 3 cm long and 2.3 cm diameter copper cathode ring. They are concentric with the anode wires while the grounding wires sit just outside of the rings.

The drift wire cells in NEMO-3 were operated in Geiger mode which allows saturated amplification of the signal. This makes the cells more robust and allows the readout to be done with simple (RC) electronics but has the limitation of necessitating low event rates. Under normal operating conditions the voltage of the anode wires was set to, on average, +1800 V and the gas was a mixture of helium, ethyl alcohol, argon and water. When a charged particle, such as an electron from the source foil, passed through a cell it would ionize some of the helium gas producing He^+ ions that drift towards the anode wire. An avalanche effect causes a large amplification of charge, known as the primary avalanche, which is read from the anode by electronics and determines the arrival time of the signal. The drift times are measured as the difference between the event start time (measured by the calorimeter, the fastest timing element in the detector) and the anode arrival time and are used to establish the transverse position of the particle track with a spatial resolution of 0.5 mm.

In the Geiger regime the avalanches will also give rise to a Geiger plasma that propagates along the axis of the anode wire with a speed of $6-7\,\mathrm{cm}/\mu\mathrm{s}$. The creation and propagation of this plasma results in the generation of a voltage which in turn generates a current with the help of the cathode rings. Electrons collected by the cathode rings at each end of the wire define propagation times for the upward and downward traveling Geiger plasmas. The difference between these times are then used to establish the longitudinal position of the particle track with a spatial resolution of $0.8\,\mathrm{cm}$.

For a typical event the anode rise time was about $10\,\mathrm{ns}$ and produced a "one-plasma" amplitude (The amplitude of a signal pulse when part of the Geiger plasma reaches one end of the cell, about half of the anode pulse amplitude) of around $50\,\mathrm{mV}$ measured at $270\,\Omega$. This leads to a current of about $200\,\mu\mathrm{A}$ collected over a typical total propagation time of $40\,\mu\mathrm{s}$ which results in a total charge collection of $Q = 10^{-8}\,\mathrm{C}$ or about 6×10^{10} electrons. Following an event each cell then had a dead time corresponding to the total charge collection time of about $500\,\mathrm{ms}$.

Gas Mixture

The original design of the tracker called for a gas mixture of helium, whose low Z-value yielded good detector transparency, and ethyl alcohol, which was used as a quencher to limit photo-ionization and the re-firing of adjacent cells. The alcohol content had to be carefully chosen though as an excess would reduce the photon path length too much and all but kill the full propagation of the Geiger plasma. Eventually, small amounts of argon and water vapor were also introduced into the mixture to help stabilize the cells and counteract aging effects. The final mixture consisted of these gases in the following approximate proportions: 95% helium, 4% ethyl alcohol, 1%

argon and 0.15% water vapor.

3.5 The Calorimeter

The NEMO-3 calorimeter consisted of 1,940 optical modules (OMs) made of plastic scintillator blocks coupled to either 3 or 5 inch photomultiplier tubes (PMTs) via optical light guides. They completely covered the inner and outer vertical walls enclosing the tracking volume and partially cover the top and bottom end caps, or petals, of each sector. Beyond serving primarily to measure the energy of incident particles they also are used to provide fast trigger signals and give time-of-flight measurements. The OMs are supported on a rigid frame which immerse the blocks inside of the tracking chamber gas mixture (to minimize electron energy losses) while keeping the PMTs outside of the gas (to prevent rapid aging from the helium).

Due to the geometry of the detector, seven types of OMs, each with slightly varying dimensions, were developed to instrument each sector: IN, EE, and EC type OMs were used for the inner and outer walls while L1, L2, L3, and L4 type OMs were used on the petals. The inner detector wall used two 17-layer columns of IN type OMs which employed 3 inch PMTs. The external walls were made of three 13-layer columns wherein the central column used EC type OMs while the edge columns on either side used EE type OMs. Both EE and EC types OMs used 5 inch PMTs. The L1 - L4 OMs were used at radially increasing concentric layers on each top and bottom petal. Each layer consisted of three blocks with L1 and L2 layers on the internal side relative to the foils and L3 and L4 layers on the external side. The L1-L3 type OMs all used 3 inch PMTs while the L4 OMs used 5 inch PMTs. Details on the dimensions and number of each type are summarized in tables 3.2 and 3.3.

Type	**Number** (per sector)	**Dimensions** Thickness×Height×Width [mm^3]	**PMT**
IN	34	110×153×154/138	3”
EC	13	99×200×218/228	5”
EE	26	99/123×200×218/228	5”

Table 3.2: Summary of properties for the NEMO-3 wall-mounted optical modules (OMs).

Type	**Number** (per sector)	**Dimensions** Thickness×Length×Width [mm^3]	**PMT**
L1	6	100×126×113/126	3”
L2	6	100×126×133/146	3”
L3	6	100×126×174/188	3”
L4	6	100×126×195/208	5”

Table 3.3: Summary of properties for the NEMO-3 petal-mounted optical modules (OMs).

Scintillator Properties

Polystyrene (PS) is used as the base material for all NEMO-3 scintillator blocks. Although 2 cm of this material are sufficient for stopping electrons with energies up to 12 MeV, the full thickness of all block types was set at 10 cm to give a 50% efficiency for detecting 500 keV γ-rays. The chemical composition of the scintillator blocks consisted of p-Terphyenyl (PTP) as the primary scintillating agent as well as 1.4-di-(5-phenyl-2-oxazoly)benzene (POPOP) which acted as a wavelength shifting agent to better match the scintillation spectrum with the response of the PMT photocathodes. The components were mixed in the following proportions: 98.49% PS, 1.5% PTP, and

0.01% POPOP for inner and outer wall blocks (IN, EE, and EC) and 98.75% PS, 1.2% PTP, and 0.05% POPOP for petal blocks (L1-L4).

Photomultiplier Tubes

NEMO-3 chose to use PMTs from Hamamatsu Photonics primarily on the basis of their low radioactivity but also for their overall performance in terms of quantum efficiency, gain, linearity, and electronic noise. The IN, L1, L2, and L3 type OMs used Hamamatsu R6091 3-inch PMTs with 12 dynodes and a flat photocathode ($\phi = 76\,\text{mm}$). The EE, EC, and L4 type OMs used Hamamatsu R6594 5-inch PMTs with 10 dynodes and a hemispherical photocathode ($\phi = 127\,\text{mm}$). Although both PMT types used light guides to couple to their respective scintillator blocks the geometry of the 5-inch PMTs also necessitated the use of an additional interface guide between the PMT and light guide.

Light Guides

A 60 mm thick cylindrical piece of polymethylmethacrylate (PMMA) plexiglass is used to interface PMTs with their respective scintillator blocks while keeping the PMTs well protected from the tracking volume gases. They were chosen on the basis of providing a good seal against helium from the tracker and excellent optical performance with light transmission of 98% in the range $380 - 420\,\text{nm}$. To bolster their mechanical properties, light guides were glued to an iron ring providing a press fit between the guide and the petal or wall.

Optical Module Assembly

A great deal of work was put into the preparation and assembly of the different elements that make up a NEMO-3 OM. Beginning with the scintillator blocks, each was sanded under water with 1200 grit sandpaper to produce diffusive reflections at the surfaces. Next, each block was wrapped in five layers, around the four lateral faces only, of 70 μm thick Teflon tape. This aided in diffusely scattering the scintillation light to improve light collection characteristics. Before proceeding to the next stage, each block was temporarily wrapped in 12 μm for testing its energy resolution using a tunable electron source set to generate a 1 MeV beam. Blocks that passed this test with suitable energy resolution values were then wrapped permanently in aluminized mylar. For petal blocks, two layers of 6 μm thick aluminized mylar were used on all six faces (leaving a hole for light guide coupling). For wall blocks, two layers of 6 μm thick aluminized mylar were used on the entrance face of each block while one 12 μm thick layer was used on the remaining five faces (again with an allowance for light guides). This layer served two purposes for the OMs: it offered protection from ambient light or light produced during operation of the Geiger cells in the tracker and it improved light reflection in the scintillator blocks to aid in light collection by the PMTs. Before coupling the blocks to light guides, the guides were wrapped in a layer of aluminized mylar, glued to their iron rings, and then mounted onto the wall or petal structures using RTV. Once a good seal against helium was verified, the light guide and scintillator block were optically glued together and then checked to ensure that no major bubbles or irregularities were present. The peak energy resolution of each partial OM was then measured with 1 MeV electrons again and the information was used in determining which PMTs to couple to which blocks.

In order to maximize the uniformity of response of the calorimeter, better per-

forming PMTs were coupled to worse performing blocks and vice-a-versa. To do this, each block was illuminated with a 1 MeV electron source to obtain an ADC response. The distribution of this value across all scintillators is roughly Gaussian with mean $\langle \text{ADC} \rangle$ and covariance σ_{ADC}. This permits the definition of a quantity μ given by

$$\mu = \frac{\text{ADC} - \langle \text{ACD} \rangle}{\sigma_{\text{ADC}}}, \tag{3.5.1}$$

which characterizes the light efficiency properties of a block with respect to the mean response.

In a similar manner, the each PMT can be quantified relative to the ensemble behavior using the Corning Blue (CB) value as a discriminating variable. The Corning Blue value is a measure of the PMT's sensitivity at 430 nm (in units of μA/lm) and is provided for each tube by Hamamatsu. In this case the CB value for each PMT is used along with the mean ($\langle \text{CB} \rangle$) and variance ($\sigma_{\text{CB}}$) of all values to define

$$\nu = \frac{\text{CB} - \langle \text{CB} \rangle}{\sigma_{\text{CB}}}. \tag{3.5.2}$$

Scintillator-PMT coupling was then chosen based on the relation that $\mu \approx -\nu$ but results were constrained by the limited number of PMTs relative to blocks and by the fact that multiple PMTs were associated to each HV channel wherein values could not vary by more than 80 V. Furthermore, the association was done separately for IN, L1, and L2+L3 blocks (for 3 inch PMTs) and for L4 and EE+EC blocks (for 5 inch PMTs). This too limited how well the pairing relation could be applied.

The final gluing of the PMTs to scintillators was carried out in the LSM lab. The interface guides for the 5 in PMTs were wrapped in a layer of aluminized mylar and glued to the PMTs prior to transportation to the LSM. Once each sector was erected, the PMTs were glued to light guides and allowed to dry. A light tight sleeve was then placed over them and sealed with RTV. Next, a μ-metal magnetic shield

was installed around each PMT and extending to the light guide as well. Finally, a radiopure sponge-like material was used to fill any holes or gaps to prevent light leaks. An illustration of a fully assembled OM is shown in figure 3.7.

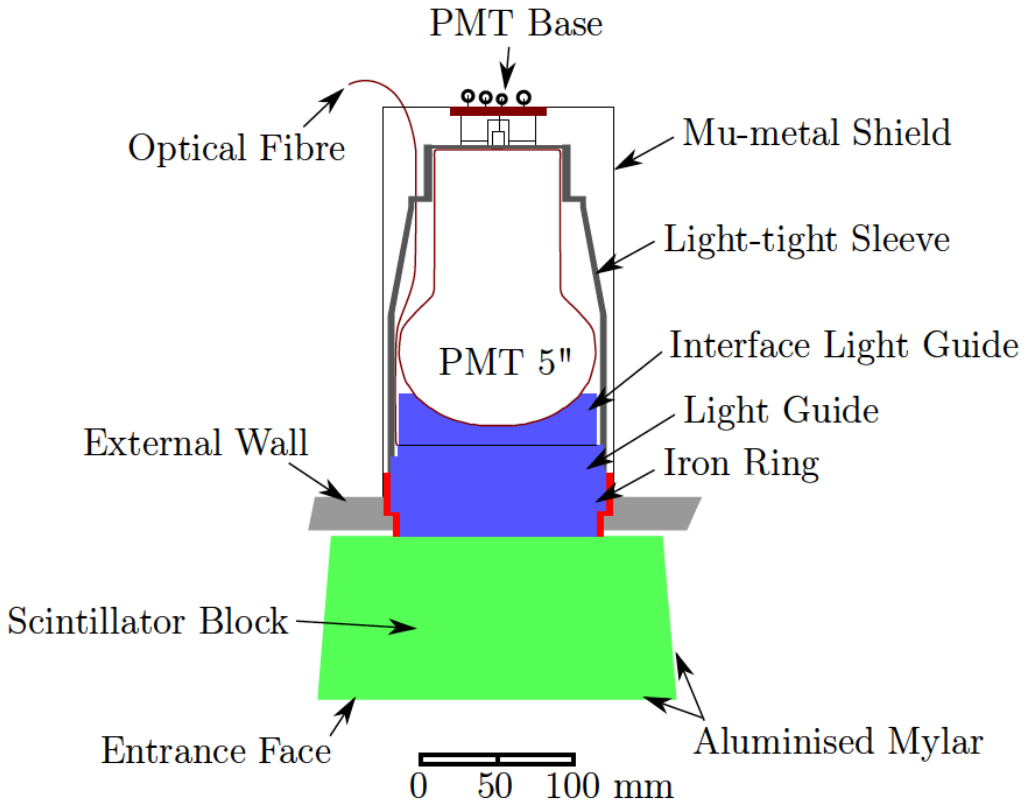

Figure 3.7: An illustration of a NEMO-3 calorimeter optical module (OM) with a 5 inch PMT.

3.6 Magnetic Coil and Passive Shielding

There are two main sources of external background in NEMO-3. The first comes from γ-rays due to natural radioactivity, neutron capture, and bremsstrahlung of cosmic ray muons in the environment surrounding the detector. The second comes from neutrons due to (α,n) reaction, the spontaneous fission of uranium, and interaction

of cosmic ray muons in the surrounding rocks. These neutrons can then be captured in or near the detector producing more high energy γ-rays. These γ-rays from external origins can then interact in the source foils of the detector producing events which mimic $\beta\beta$ decays. In order to limit the influence of γ-rays and neutrons the detector was surrounded by a large solenoid and two external shield structures. The innermost of the two was designed to suppress γ-rays and thermal neutrons while the outermost was designed to suppress slow and fast neutrons.

Magnetic Coil Assembly

Simulations of neutron capture induced γ-rays in NEMO-3 showed that the primary background contributions were due to (e^+e^-) events and to a far lesser extent (e^-e^-) events in the source foils. The detection of these γ-rays in the calorimeter can reject about 80% of these events. Of those that remain, the 25 G magnetic field produced by the solenoid provides enough charge discrimination to reject 95% of the (e^+e^-) events.

This coil surrounds the entire detector but was designed to be piecewise removable to allow access to individual sectors. The coil is made up of 203 highly radiopure copper rings divided into ten sections (covering two sectors each). Each ring has a square cross section 10 mm $\times$ 10 mm with 3 mm of separation between adjacent rings. Once fully assembled the coil had a diameter of 5320 mm and a height of 2713 mm and a total weight of approximately 5 tons.

To produce the desired field strength of 25 G a current of 29 A was passed through the coil. The electrical resistance of the entire coil was approximately 0.65 Ω leading to a required voltage source of 18.9 V. Air fans mounted to the iron shielding in each sector provided cooling for the coils as well as PMTs.

Iron Shielding

The iron shielding was also subdivided into ten section along with two additional pieces to cap the top and bottom of the detector. The pieces were all 20 cm thick (unless limited to 18 cm where required by support structures) and when fully assembled contributed 177 tones to the weight of the detector. The particular material used in their construction was again chosen foe its radio-purity.

Neutron Shielding

The neutron shield consisted of three parts: the first is 20 cm worth of paraffin beneath the central tower, the second consists of 28 cm-thick pieces of wood on the top and bottom of the detector, and the last consists of ten large tanks of borated water, 35 cm thick, which comprise the external wall of the detector. These elements are designed to stop fast neutrons with energies of a few MeV while simultaneously suppressing thermal and epithermal neutrons.

3.7 Calibration and Monitoring

The accurate measurement of the energy from a $\beta\beta$ decay event is one of the most important goals for the NEMO-3 detector and thus a robust calibration procedure is required. This is achieved using radioactive calibration introduced into the detector for dedicated calibration runs. Such runs employed ^{207}Bi and ^{90}Sr sources, usually lasted approximately 24 hours, and were performed on a monthly basis. During the times between these runs a laser survey system was employed to monitor the day-to-day stability of the calorimeter.

Since the calorimeter is also important in providing time-of-flight information to

distinguish internal and external events, temporal calibration is also required. The relative timing offset for each calorimeter OM is determined by measuring times for coincident events from a ^{60}Co radioactive source. Particle time-of-flight values must also be corrected for several other effects including amplitude corrections due to leading edge discriminators (called time-energy corrections) and TDC slope corrections. These effects were also measured using the laser survey system.

Radioactive Source Calibrations

Every sector in NEMO-3 was instrumented with a single flat copper calibration tube installed vertically at the same radial position as the source foils but near the edge of the sector. Each tube had three pairs of windows located at different vertical positions ($Z = 0, \pm 90$ cm where zero corresponds to the midpoint in the vertical or Z-axis) with orientations towards the inner and outer calorimeter wall. Each 26×20 mm window was sealed from the tracker gas using 25 μm thick kapton. A long delrin rod supported the six sources which lined up with the windows when the rod was lowered into the detector. The vertical positioning of the sources maximized the illumination uniformity upon the calorimeter. Furthermore, since the radial position was identical to that of the foils, the trajectories of calibration particles were nearly identical to those originating from the foils.

Two different radioactive sources are used for absolute energy calibrations. The first ^{207}Bi , decays via electron capture to ^{207}Pb which produces conversion electrons with K-shell energies at 482 keV and 976 keV (and with much lower intensity at 1682 keV). Since many γ-rays are also produced in the decay the tracker must be on during ^{207}Bi calibration runs to select the electrons of interest. This limits the activity that the ^{207}Bi sources can have which is the main reason for the duration

of these runs. All 60 ^{207}Bi sources had activities of about 222 Bq. These source could be used for absolute energy calibrations up to 1.5 MeV. For calibrations up to 3 MeV ^{90}Sr sources were used. This isotope decays into ^{90}Y which is a was a pure β emitter with endpoint energy of 2.283 MeV (at an intensity of 99.984%). For these runs, the tracker was not required which meant that higher activity sources of 6 kBq could be used along with shorter run durations. For each energy calibration run, energy spectra are collected from each of the 1940 calorimeter channels and the peak (for ^{207}Bi runs) or endpoint (for ^{90}Sr runs) positions are fitted to determine correction values used in calibrations. The three energy calibration points are also used to check for linearity of each channel up to 4 MeV.

For timing calibrations ^{60}Co is used due to its emission of two coincident γ-rays of energies 1173 keV and 1332 keV. Since the tracker is also not needed in these runs, intense sources can again be used over relatively short duration runs. Spectra of the arrival time difference are generated from these events and used to determine the time delays between the 1940 calorimeter channels. These values are then used to to calibrate the temporal response of each channel.

Laser Surveys

Experiments with long exposure times such as NEMO-3 require stability for many years. In order to monitor the calorimeter stability between the infrequent source runs daily laser surveys are used to track the response of each channel over time. The laser survey system has multiple objectives during each of these survey runs. The first is to check the absolute energy and time calibration, the second is to measure PMT linearity up to 12 MeV, and the third is to determine the time-energy relation. To accomplish this to the desired precision ($< 1\%$) the laser system must excite a

response from each calorimeter channel that is very similar to that of an electron induced event. Furthermore, the laser output must be known accurately and must remain stable as well.

The laser survey system used an N_2 laser of wavelength $377 \pm 15\,\text{nm}$. The beam produced from this laser is passed through a series of optical filters and splitters. The first splitter sends part of the laser beam to a photo-diode to monitors the stability of the laser output. The other part of the beam is passed to a system of various attenuating filters which adjust light levels to those which exercise the dynamic range of the calorimeter OMs. This portion of the beam proceeds to another splitter which distributes this light into two small plastic scintillating spheres wrapped in Teflon and aluminum. The purpose of the spheres is to absorb the laser UV light which excites 420 nm scintillation light that is then sent to OMs via optical fibers. This light then mimics the signal of electrons in the OMs. One sphere couples to fibers which deliver light to the 1040 OMs that use 3 inch PMTs while the second sphere couples to fibers that reach the remaining 900 OMs using 5 inch PMTs. In addition, there are six total reference OMs that are external to the detector and compare light levels against conversion electrons from ^{207}Bi sources. Two reference OMs (one 3 inch PMT and one 5 inch PMT version) look at the same light as the photo-diode. Two 3 inch PMT OMs look at the light received by the corresponding 3 inch PMT OMs in the detector. Similarly, the last two reference OMs use 5 inch PMTs and monitor the light delivered to corresponding OMs in the detector that use 5 inch PMTs.

By using the results of an absolute energy calibration run with radioactive sources, and accounting for changes in the laser output using the photo-diode and reference OMs, the behavior expected for each calorimeter OM could be predicted and compared to the response actually seen from the laser survey. Those OMs which showed

uncharacteristic or unstable behavior during the survey period were omitted from analyses covering that particular survey period. The laser system demonstrated that 82% of the NEMO-3 OMs suffered no instability with an additional 7% suffering from only temporary instability only within a particular survey period. In the latter case, this was generally attributed to instabilities in the laser system itself.

The laser survey system was also used to study and correct for two different timing effects. The first is an effect due to leading edge time discriminators which produce a time-vs-energy dependence. This dependence can be parameterized and by using the laser survey system to simulate a full scan of energies from 0 to 12 MeV, the parameters can be extracted and used for correction factors. These full range laser runs were carried out only a few times per year. The system was also used for daily time corrections to account for TDC slope variations. In this case the correction factor was simply the based on the difference in TDC values at two times: $t_{corr} = tdc_t - tdc_0$.

3.8 The Anti-Radon System

Radon is a product of the decay chains of ^{238}U and ^{232}Th , both of which have long life times are are commonly found in rocks and other materials. The ^{238}U chain leads to the production of the more stable radon isotope, ^{222}Rn , with a half-life of 3.8 days while the ^{232}Th chain results in ^{220}Rn with a half-life of 55.6 seconds. In either form, radon is a very diffusive noble gas which permits it to enter into otherwise sealed volumes and decay leaving its progenies trapped. This presented a problem for NEMO-3 in the form of ^{214}Bi , a progeny of ^{222}Rn , and ^{208}Tl , a progeny of ^{220}Rn . The former can produce β decays with energies up to 3.27 MeV while the latter can produce β decays with energies up to 4.99 MeV. If the radon deposited these progenies on or near the source foil they could mimic $\beta\beta$ events. For this reason

a lot of effort was invested in reducing the radon background within the NEMO-3 detector.

The amount of radon present in the LSM lab air varied greatly, even depending on the time of day of measurements, but on average had an activity of about $20\,\mathrm{Bq/m^3}$. The RTV used to seal the majority of NEMO-3 components provided a large reduction in radon levels leading to activities of $20 - 40\,\mathrm{mBq/m^3}$ measured for the gas inside the detector. After nearly one year of operation it was decided that the radon levels needed to be reduced much further and thus a system was developed consisting of a polyethylene tent surrounding the detector and a radon trapping facility to purify the air entering this tent. The basic idea was that the immediate detector environment, contained within the tent, could be purified so that radon diffusion into the detector could be further reduced.

The radon tent covered the entire detector down to the floor of the lab and was supported by a steel cage structure. The tent was composed mainly of $200\,\mu\mathrm{m}$ thick sheets of polyethylene, in two layers, along with an aluminum and plexiglass floor and an iron roof with outlets containing active charcoal filters.

The radon trap facility was based on commonly used techniques employing charcoal to trap molecules or atoms. The basic idea, illustrated in figure 3.8, was that larger molecules such as O_2 or N_2 in air could pass through the charcoal while smaller radon molecules would be trapped until they decay. The full facility cools compressed air from the lab to $-50\,^{\circ}\mathrm{C}$ and passes this through two adsorption towers (0.6 m in diameter and 3 m tall) made of 500 kg of activated charcoal. Due to the enormous surface area provided by the charcoal, a large fraction of the radon would decay before getting to escape the towers. This facility took in LSM air at a rate of $150\,\mathrm{m^3/h}$ and reduced the radon levels by approximately three orders of magnitude from $20\,\mathrm{Bq/m^3}$

to about 18 mBq/m^3. The resulted in a decrease in radon levels inside the NEMO-3 detector from 37.7 ± 0.1 mBq/m^3 to 6.46 ± 0.05 mBq/m^3 [72]. Because of this sharp change in the environmental operating conditions, NEMO-3 data is separated into two phases distinguished by the installation of the anti-radon facility. Phase 1 data concerns those runs taken from the start of the experiment in February 2003 to September 2004 while Phase 2 concerns runs from October 2004 up to January 2011.

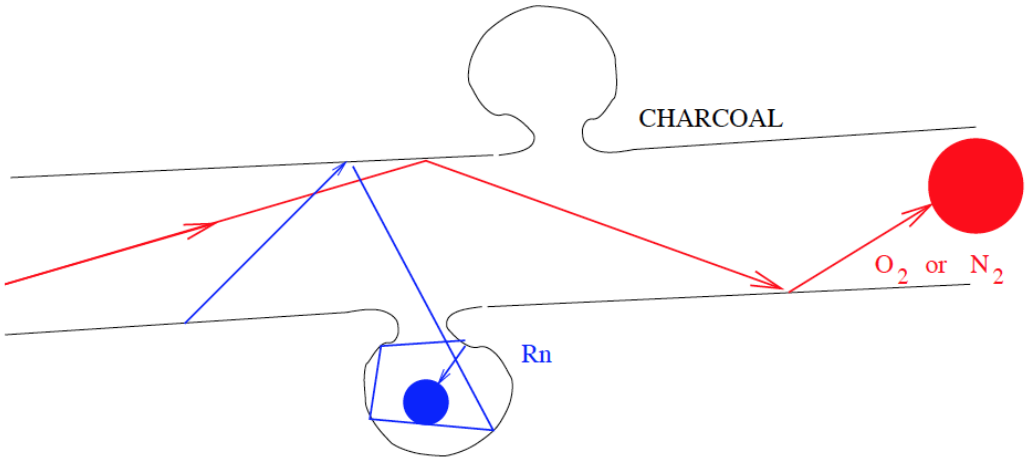

Figure 3.8: An illustration of the radon trapping principle using activated charcoal.

Chapter Four: NEMO-3 Data

The NEMO-3 detector is designed to observe and collect information from various nuclear decays and particle interactions that occur within its volume. Standard NEMO-3 analyses are based on generating simulated Monte Carlo (MC) events to mimic signal and background processes and then compare these against real data. The simulations take into account not just the kinematics of the originating processes but also on how the resultant particles propagate and interact within the NEMO-3 detector. In order to make the data and MC agree, a reconstruction software also ensures that simulated events are subject to the same detector issues affect data in the form of changes in energy resolution or loss of particular calorimetric or tracker components. The general approach taken in this analysis has been to use this rich information set available for each detector event to construct very pure decay channels from which to build time series of the decay rate. These time series can then be analyzed using modern frequency domain techniques to search for periodic variations in the measured decay rates. The ROOT analysis framework [75] is used to either store and/or analyze information at all levels (MC generation, reconstruction, and analysis) of data processing.

This chapter begin with an explanation of how NEMO-3 events are generated (in the case of MC), triggered, and reconstructed. Based on the information attributed to events after reconstruction, the next section explains how topological classifications can be used to identify different particle types present in an event. The following section then explains how more finely detailed cuts are used to produce very pure decay channel data sets. Afterwards, it is shown how the data is scaled to account

for detector efficiency and how a time series is generated from the data.

4.1 Monte-Carlo Simulations

Creating simulated NEMO-3 MC events begins first by using the DECAY0 software [76] to generate the resultant particles emitted in nuclear decay events. This software can handle the common decays types associated with all of the potential background isotopes in NEMO-3 as well as the generation of the more complex decays of the source isotopes in both $2\nu\beta\beta$ and $0\nu\beta\beta$ modes. These generated event particles follow proper branching ratios, temporal spacing, and kinematic behavior such as having accurate energy and angular dependence distributions attributed to them at this stage.

These generated event particles are then passed to the GEANT 3.21 [77] software which contains a full detector model through which the particles can propagate through and interact according to their full and differential cross sections. Processes including energy loss, scattering, and secondary particle emissions all simulated to help to build a complete picture of all the possible decay topologies that naturally occur within the detector. Any particles that interacts with a reactive detector component will result in proper charge readout signals to recreate accurate raw data that mimics how true data events are recorded. This allows for an identical trigger and reconstruction process to then be applied to the raw data regardless of whether its MC or real data. This MC generation is broken down into manageable sized chunks to allow for parallel processing of files in the later reconstruction and analysis phases. For every one million generated events, the simulation outputs the relevant raw detector data into a ROOT file. Depending on the desired statistics for a MC channel, this can result in tens or hundreds of individual MC files.

Since the simulated events must correspond in time with the status of the detector, the MC events must be attributed to the discrete acquisition periods known as "runs." For each run, specific information regarding the overall quality of the detector and the data acquisition during the time span of the run is saved into the NEMO-3 database. Regardless of the total number of MC events generated in a given set, they are separated into run periods based on the length of these runs (so that longer runs are assigned more events than shorter runs). This is one of the essential differences between data and MC files. Data files contain events corresponding only to the run period in which they were collected whereas MC files contain events which are distributed into all run periods. This information is critical for the reconstruction software to keep MC events on the same footing as true data events on a run-to-run basis.

4.2 Event Trigger and Reconstruction

When an event occurs in the detector, whether real or simulated, it must first satisfy a number of conditions to be recorded. The primary trigger for an event readout is a PMT signal passing a threshold corresponding to approximately 150 keV in energy. This is due to the fact that the calorimetric signal is the fastest element in the detector and determines the zero or start time for tracking chamber Geiger cells. Once readout is triggered, all PMT channels are in fact opened to read in and store the integrated charge values. This capture also generally has the previous 80 ns stored and included.

Using the initial PMT signal as the start time there are four other times recorded for each Geiger cell: T_{C1}, T_{C2}, T_A and T_α. The first two times are recorded when signals are detected on each of the cathode rings. The last two are anode times with the first being recorded if the threshold is reached within 6.14 μs after the start

time and the latter being recorded if the threshold is reached between $6.14 - 704\,\mu$s after the start time. This secondary anode trigger time is chosen to detect potential delayed alphas which result from a $^{214}Bi -^{214} Po$ decays (these are discussed in more detail in section 4.3).

A reconstruction program known as NEMOR takes in the raw data from a triggered event and uses it to build a topological description of the particles involved. This means using the recorded hits in Geiger cells and scintillator blocks to build fully three dimensional particle tracks and potentially associate them to scintillators. Since the particles travel in a volume with a 25 G magnetic field the track curvatures are also computed to determine the charges of the particles that created them. The charge collection from PMTs coupled to hit scintillator blocks is also converted to an energy deposit with proper accounting for the energy resolution (and changes therein) of each individual calorimeter module.

In addition to the topological information for an event, the reconstruction software is also responsible for making sure that the complete status of the detector is represented in both real and MC events to properly account for changes in the detector's efficiency. This requires that NEMOR connects to the NEMO-3 database where valuable run properties and calibration info are stored. From here NEMOR obtains the run information including but not limited to the following parameters.

- Run status, a flag which denotes the general quality (good or bad) of a run and also accounts for conditions such as high radon contamination, recent calibration runs or detector component shutdowns, lack of laser calibration data for a given time period, and other issues that may affect the data quality.

- Run timing information such as start and stop time stamps, run lengths, and run dead times.

- Calibration constants for PMT, scintillator, and Geiger cell responses and re-weighting factors.

As an example, the reconstruction needs to read in from the database if certain regions of the calorimeter or tracker were inactive (perhaps due to maintenance or repair). True data events that interacted in these regions of the detector would certainly not be recorded so in a similar fashion the reconstruction has to ignore any MC events, assigned to that run period, which interact in the same regions. This will be discussed further in 4.6 where the detector efficiency will be shown as a function of the run period at different stages of the analysis (triggering, reconstruction, and event selection).

4.3 Particle Identification

Once events have been reconstructed the full strength of the NEMO technique is revealed in its ability to identify, with high fidelity, the various particles that compose an event such as electrons, positrons, alpha particles, and gamma rays. The key to this lies in the use of the tracking chamber and calorimeter hits to distinguish between different topologies that are characteristic of the different particles due to their various charges, masses, and interactions.

The Hereward analysis software accepts the reconstructed output from NEMOR and uses various topology analysis modules to label event particles by type and then store relevant information such as the particles energy, track length, curvature, and so on. These modules are described in detail below along with event displays showing how they can be used in identifying background processes.

The Electron Finder

The Electron Finder module in Hereward identifies electrons and positrons as particles which have tracks that can be traced to an associated scintillator block in which an energy deposit was registered. This deposit should be entirely contained within a single, isolated block since electrons will, at the energies typical of nuclear decays, only travel a few centimeters into a block before losing all of their energy to scintillation light. Furthermore, since electrons and positrons are charged but very light particles the 25 G magnetic field should be sufficient to separate the two particle types by the curvature of their respective tracks.

The Alpha Finder

Alpha particles are over 7000 times more massive than electrons and carry twice the electric charge. This results in vastly different particle track characteristics as they travel through the tracking chamber. The increased charge means that alphas interact more strongly in the tracker gas and thus lose energy faster leading to short tracks with maximal lengths (at energies typical of alpha decays) of about 35 cm. The increased mass of alphas means that the magnetic field that cause significant deflections in electrons leads to barely perceptible levels of curvature in alpha tracks. The Alpha Finder thus identifies alpha particles as those which create short straight tracks. Although alpha particles are easily distinguished as background events they are important in measuring specific decay channels which can be used to measure the activities of particular background-causing isotopes. The most relevant example is the so-called "BiPo" process which involves ^{214}Bi decaying into ^{214}Po via a high energy ($Q_\beta = 3.27\,\mathrm{MeV}$) beta transition. This energy is sufficient for the beta transition to induce significant contributions to the search for $0\nu\beta\beta$ decay. Luckily, the ^{214}Po

daughter then decays via alpha emission with $T_{1/2} = 164.3\,\mu$s and this alpha can be used for tagging such BiPo events. An example of such an events consisting of a prompt curved electron track (shown as in red) followed by a short delayed alpha track (in green) is illustrated in figure 4.1.

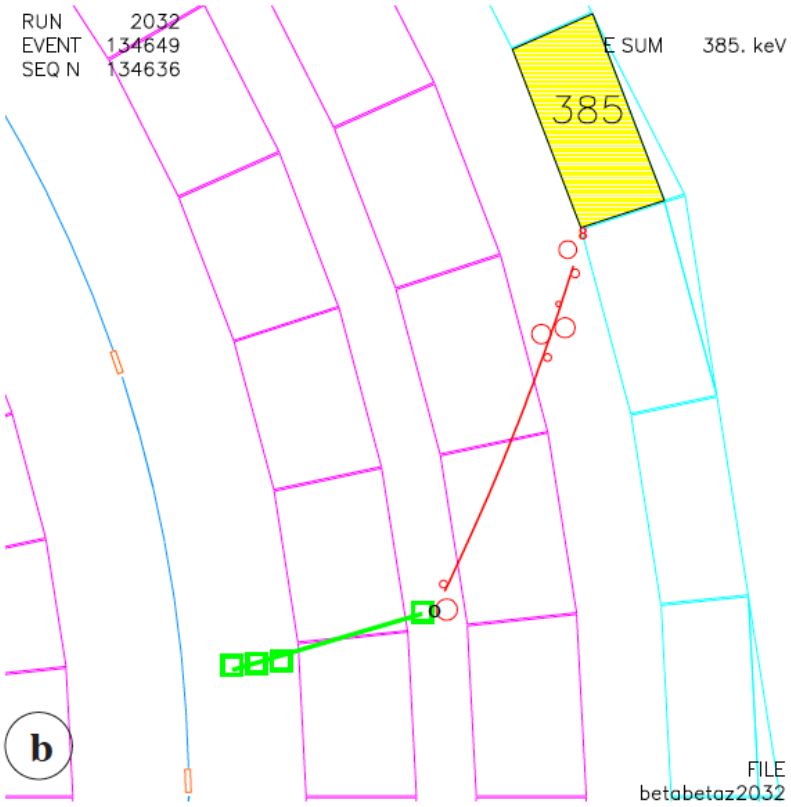

Figure 4.1: An illustration of a NEMO-3 BiPo event originating in the tracker volume. The long curved red track corresponds to the electron from the ^{214}Bi decay while the short straight green track corresponds to the delayed alpha resulting from the ^{214}Po decay.

The Gamma Finder

Gamma particles, being neutral, produce no ionizing tracks within the NEMO-3 tracking volume but they can partially deposit their energies inside of calorimeter blocks via Compton scattering with an electron inside a scintillator. Since this isn't a

form of continuous energy loss the scintillator blocks only have a certain probability for a gamma to interact within them. The NEMO-3 block dimensions were partially chosen in order to give a good efficiency for tagging gammas in events and thus a 0.5 MeV gamma has a 60% of depositing energy within a block. Gamma events are thus identified as isolated calorimeter hits with no associated tracks. The qualifier "isolated" is important for avoiding events where a gamma may register hits within two blocks and thus complicate measurement of the true gamma energies. An example of what isolated and non-isolated gamma hits look like in NEMO-3 are shown in 4.2 and 4.3 respectively.

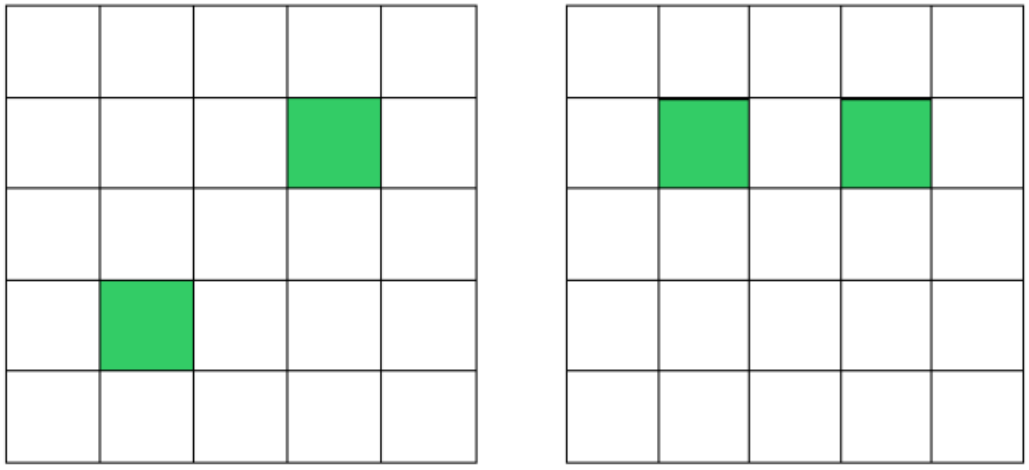

Figure 4.2: An illustration of two cases where calorimeter hits (shown in green) are considered isolated and thus correspond to acceptable gamma events.

4.4 Time of Flight

In addition to identifying particle types in an event, another important criteria for identifying backgrounds is event origin. Since a true $\beta\beta$ decay can only originate from the NEMO-3 source foils, being able to determine whether an event decay vertex

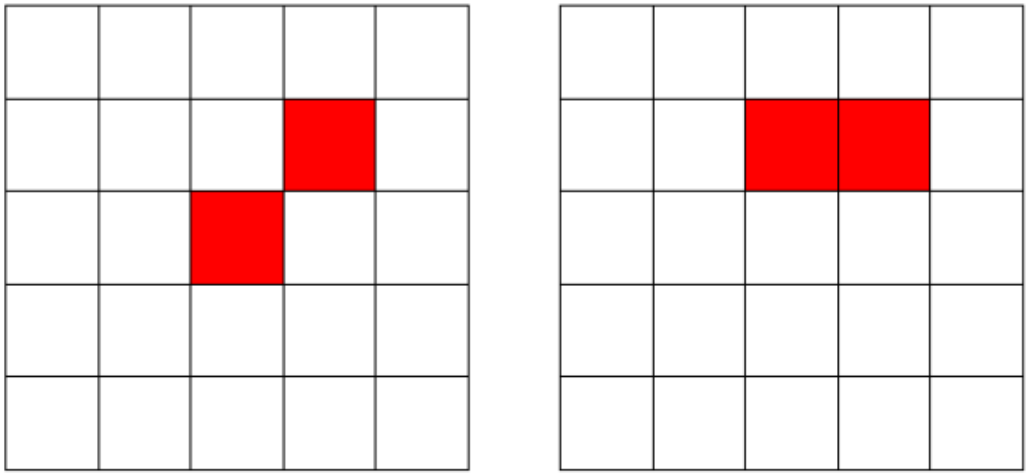

Figure 4.3: An illustration of two cases where calorimeter hits (shown in red) are considered non-isolated and thus correspond to unacceptable gamma events.

resides inside the foil or not is an important rejection tool and is done using Time of Flight (ToF) information. The ToF information is used to distinguish two cases.

1. Internal: The event is due to two particles originating from a common vertex which propagate outwards to the calorimeter walls.

2. External: The event is due to a particle which first interacts in one calorimeter and then it, or a resultant particle, activates a second calorimeter on the other side of the foil.

Beginning with a hypothesis for each case, a probability can be constructed and used to discriminate between events by cutting those with a high probability of having external origin and a low probability of having an internal origin. The construction of these probabilities is described below.

Internal Probability

If one assumes, under the internal event hypothesis, that the two particles originated from the same decay vertex within the source foils one can calculate the probability of this being true based on the measured calorimeter hit times t_i^{meas} for $i = 1, 2$. This is known as the internal probability and is used in the analysis to cut events with low probability of having originated within the NEMO-3 source foils.

Since the assumption is that the particles were created simultaneously, then taking the difference between the measured time and ToF, for each particle, should give their time of emission and this should be nearly the same for the two particles. In other words, The difference between the emission times calculated for each particle should be small. To begin with calculating this probability, the ToF is given, in natural units, as,

$$t_i^{tof} = \frac{l_i}{\beta_i}, \tag{4.4.1}$$

where l_i is the measured track length (in the case of electrons) or the straight-line distance between the hypothesized vertex and hit calorimeter element (in the case of gammas) and β_i is the ratio of the particles velocity to the speed of light. For photons $\beta_i = 1$ but for electrons, with measured calorimeter energy E_i and mass m_e, it is given by

$$\beta_i = \frac{\sqrt{E_i(E_i + 2m_e)}}{E_i + m_e}. \tag{4.4.2}$$

The time of each particle's emission is then estimated as

$$t_i^{int} = t_i^{meas} - t_i^{tof} = t_i^{meas} - \frac{l_i}{\beta_i}. \tag{4.4.3}$$

Due to the approximately Gaussian nature of the distribution of this variable a χ^2 test can be used with

$$\chi^2_{int} = \frac{(t_1^{int} - t_2^{int})^2}{\sigma^2_{t_i^{int}} + \sigma^2_{t_2^{int}}} \tag{4.4.4}$$

where $\sigma^2_{t_i^{int}}$ is the variance in t_i^{int}. This variance is a quadrature sum of uncertainty contributions from the particles speed (determined by its energy), track length, and detection time and the full expression is given by

$$\sigma^2_{t_i^{int}} = \left(\frac{\partial t_i^{int}}{\partial t_i^{meas}}\right)^2 \sigma^2_{t_i^{mean}} + \left(\frac{\partial t_i^{int}}{\partial \beta_i}\right)^2 \sigma^2_{\beta_i} + \left(\frac{\partial t_i^{int}}{\partial l_i}\right)^2 \sigma^2_{l_i}. \tag{4.4.5}$$

For electrons which interact immediately upon entering a scintillator the uncertainty in their path length can be neglected. For gammas on the other hand, the uncertainty in path length is much larger but there is no uncertainty in its speed. These approximations reduce the above expression to the following two,

$$\sigma^2_{t_i^{int}} \approx \begin{cases} \sigma^2_{t_i^{mean}} + \left(\frac{t_i^{tof} m_e^2}{E_i(E_i+m_e)(E_i+2m_e)}\right)^2 \sigma^2_{\beta_i}, & \text{for electrons,} \\ \sigma^2_{t_i^{mean}} + \sigma^2_{l_i}, & \text{for gammas.} \end{cases} \tag{4.4.6}$$

The probability that an event has internal origin is finally given by

$$P(\chi^2_{int}) = 1 - \frac{1}{\sqrt{2\pi}} \int_0^{\chi^2_{int}} x^{-\frac{1}{2}} e^{-\frac{x}{2}} dx. \tag{4.4.7}$$

External Probability

As discussed previously, external events occur when an outside particle results in two separate interactions in two different, opposite side scintillators (whether the same particle results in both interactions or a secondary particle is created resulting in the second interaction). The calculation of the probability then proceeds in a very similar fashion but with a slight modification. Previously the χ^2 variable was taken based on the relative difference between the two estimated emission times of the particles. In this instance the difference in the two measured times of should equal the total ToF of the particle(s) so that the χ^2 depends on the relative difference of these two quantities. Using a total Tof given by

$$t^{tof} = \frac{l_1}{\beta_1} + \frac{l_2}{\beta_2}, \tag{4.4.8}$$

where the l_i and β_i are defined as before then the χ^2 is given by

$$\chi^2_{ext} = \frac{\left((t_1^{meas} - t_2^{meas}) - t^{tof}\right)^2}{\sigma^2_{t_i^{int}} + \sigma^2_{t_2^{int}}}. \tag{4.4.9}$$

Notice the $\sigma^2_{t_i^{int}}$ remain the same as in the internal probability hypothesis (equation 4.4.6) and the calculation of $P(\chi^2_{ext})$ is done using equation 4.4.7. An example of possible events that can be determined to have external origins are shown below in figures 4.4 and 4.5. The first shows an event where a gamma can Compton scatter off an electron near the surface of the scintillator thus ejecting it so that it crosses the detector (and foil) to deposit its remaining energy on the opposite wall calorimeter. The second depicts an event in which a gamma Compton scatters in one scintillator and continues into the detector where it Compton scatter a second time in the source foil and ejects an electron which reaches the opposite wall calorimeter. As in the case of so-called BiPo events described in section 4.3, these would not mimic a true $\beta\beta$ signal event but are important in measuring various backgrounds in NEMO-3.

4.5 Event Selection

The HEREWARD analysis program aggregates the different PID modules and the ToF information along with other sub-modules designed to analyze different NEMO-3 event topologies. It also communicates with the NEMO-3 database to get a full description of the detector status for each run period. The inputs to the HEREWARD program are the output ROOT files from the reconstruction software. The program loops through each event in a given reconstruction file (recall that MC events are distributed into different runs based on run length but for data these events all correspond to a single run period) and applies a set of user-defined cuts based on which particle types are required in the event and what topological cuts they mast satisfy.

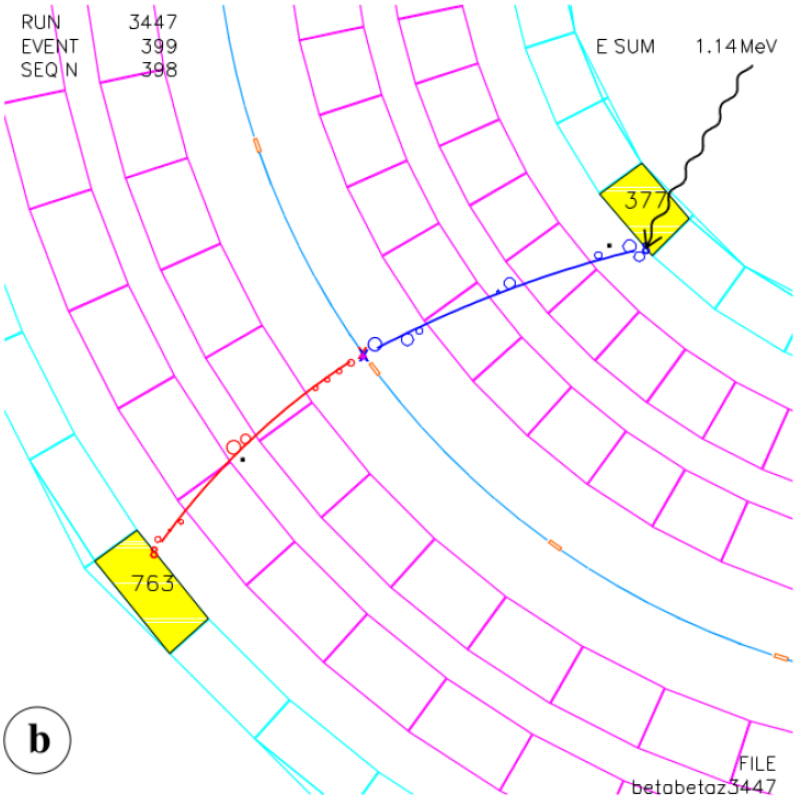

Figure 4.4: An illustration of a NEMO-3 crossing electron event with external origins according to ToF information. This top-down view shows calorimeter blocks represented as rectangles, with hit blocks in yellow, and different particle tracks represented by blue or red lines. The black lines are superimposed to show the expected path of a gamma particle.

This next section describes how such cuts are defined in order to build a very pure set of $\beta\beta$ decay events originating from any of the ^{100}Mo source foils. Using this $\beta\beta$ channel over other possible isotopes was chosen due to the fact that ^{100}Mo provides much higher statistics relative to other isotopes (since it accounts for nearly 70% of the total mass of $\beta\beta$ decay isotopes) and also provides a much cleaner channel with the highest signal to background ratio after final event selection.

The full set of NEMO-3 data spans nearly eight years worth of observation time. This was divided into two phases which differed by the installation of a radon tent in the later phase to drastically reduce the radon induced backgrounds in the detector.

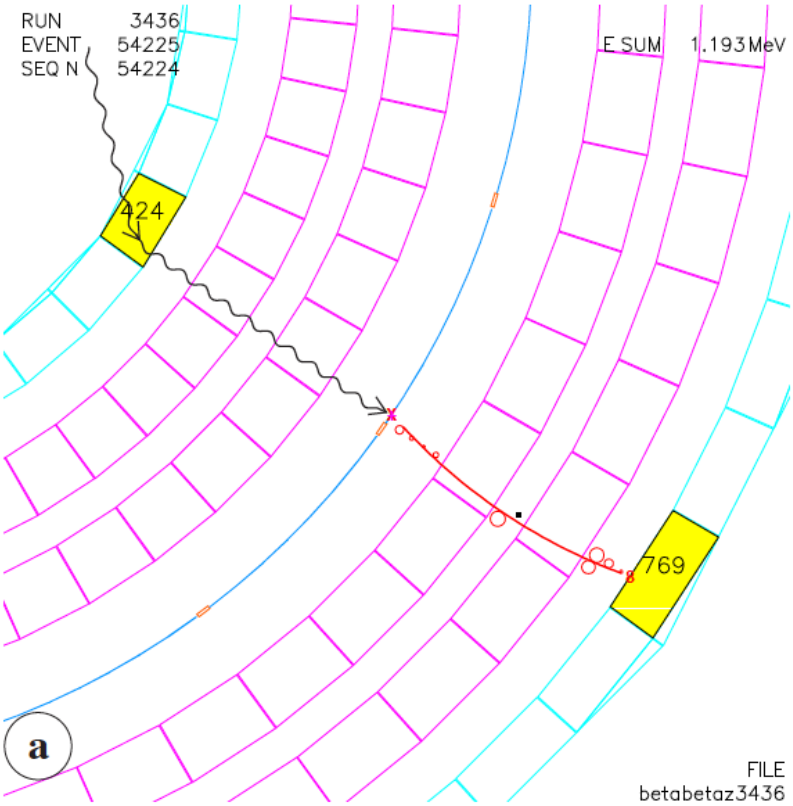

Figure 4.5: An illustration of a NEMO-3 electron-gamma event with external origins according to ToF information.

From these two data sets, runs were selected that were qualified as having a "good" status (where status is a general descriptor applied to each run which depends on various run properties that affect overall detector performance). These two phases and their lengths are summarized below in table 4.1.

Phase	**Runs**	**Dates**	**Span (yrs)**
P1	1869 - 3391	February 15th, 2003 - September 20th, 2004	1.5942
P2	3435 - 9060	October 24th, 2004 - November 1st, 2010	6.0195
P1+P2	1869 - 9060	February 15th, 2003 - November 1st, 2010	7.7079

Table 4.1: Summary of the time span of the NEMO-3 data sets.

From this point a series of event selection criteria, presented next in section 4.5, are applied to the data in these runs to extract only those events which appear to originate from desired decay channels. The events that pass all of the selection cuts produce a very pure sample where the ratio of signal to background events (S/B) has been shown to be 76 in P2 data [78] and 40 in P1 data [79].

A blinded analysis approach was taken in actually constructing and analyzing the final decay rate time series to search for periodic variations. The blinding procedure is discussed in more detail in section 5.2 of the next chapter but it is briefly mentioned here as the two data taking phases were un-blinded separately. Since the P1 data has significantly higher noise (due to the lower S/B ratio) and also spans a much shorter time it is much less sensitive to detection of hidden periodic modulations. For this reason it served as the first data set on which to un-blinded the analysis for final cross-checking of any potential issues. The P2 data only was then used to produce the final analysis results in the search for periodic modulations of $\beta\beta$ decay rates.

Two Electron ^{100}Mo

In a true $\beta\beta$ decay event (which does not result in an excited nuclear state) there should be only two electrons emitted from a common vertex within the source foil of the desired isotope under consideration. The tracking and calorimeter information is used to extrapolate to more fine event details used in the selection process. As an example,tracks can be extrapolated to judge events based on where they impacted the scintillator blocks or how well the vertices calculated from each track agree with one another. The following list of requirements is used to maximize the number of ^{100}Mo $\beta\beta$ decay signal events relative to the number of background events.

- The event is in a good quality run (PMTs are well calibrated, no recent detector

shutdowns, etc.)

- The event has exactly two particles identified as electron and exactly two tracks
- The event has no particles identified as alphas
- The event has no particles identified as gamma rays with energies $\geq$ 150 keV
- Each electron impacts a different scintillator block and only on the front face of the block
- Each electron hits a block where the PMTs have good status and good calibration flags for that run period
- Each electron calorimeter hit is isolated and must have energy deposits $\geq$ 200 keV
- None of the electrons register a hit in the petal blocks nearest the foil
- Electron tracks intersect the foil with their vertices in the same ^{100}Mo foil (any sector except 13 due to Geiger noise)
- Electron vertices must not be within a designated "hot spots" of high radioactive contamination
- Electron vertices must not differ by more than 4 cm in both the XY and Z planes
- Electron vertices must also be within foil limits in Z ($|Z| \leq 120$ cm)
- Electrons must fire Geiger hits within 50 cm of the vertex on the foil
- The sum of the electron track lengths must be $\geq$ 60 cm

- The internal probability of the event is $\geq 4\%$ and external probability is $\leq 1\%$
- If the electrons are on the same side of the foil, there can be no opposite side calorimeter hits

An example of a good $\beta\beta$ decay candidate events is shown in figure 4.6 and shows two electrons originating from a common vertex in the ^{100}Mo source foil each creating well reconstructed, negatively curved tracks that end in isolated calorimeter blocks with sufficient energy deposits.

To calculate the rate of $\beta\beta$ decays for a given run period, the total number of such events passing all selection criteria in that run is divided by the total length of that run in seconds. That is, for the i^{th} run, the measured decay rate is given by

$$R_i = \frac{N_i^{\text{selected}}}{\Delta T_i} \tag{4.5.1}$$

where ΔT_i is the duration of that run. For all of the runs that have accepted events, various distributions are shown in figures 4.7, 4.8, and 4.9 for the number of selected events per run, the length per run, and the calculated rate per run, respectively.

4.6 Detector Efficiency

The rates calculated in the above manner do not account for detector efficiency changes. Although all the runs are considered to be of good quality, the detector efficiency still changes from one run to the next since, over time, certain detector components will age and become obsolete in terms of their usefulness. For example some PMTs stop behaving as expected and need to be excluded for the remainder of runs. Regardless of the cause, sometimes two successive runs of identical length

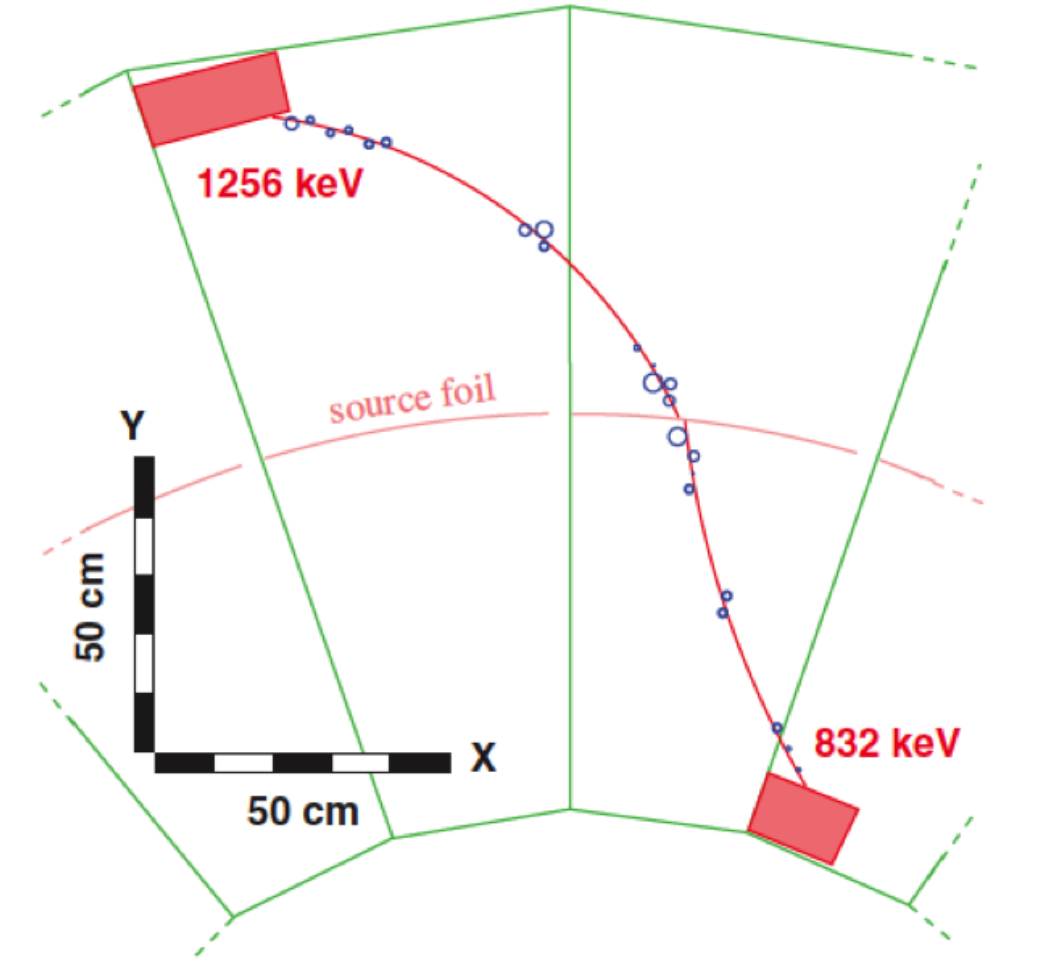

Figure 4.6: NEMO-3 event display showing a candidate ^{100}Mo $\beta\beta$ decay event with two electrons originating from a common vertex in the source foil and creating characteristic electron tracks in the tracking volume before depositing their energies in two isolated scintillator blocks.

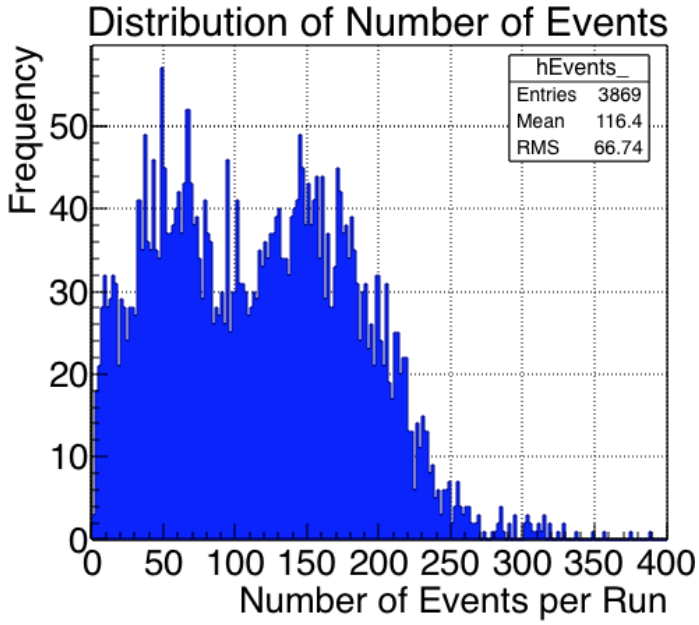

Figure 4.7: Distribution of the number of selected ββ decay events per run for P2 runs.

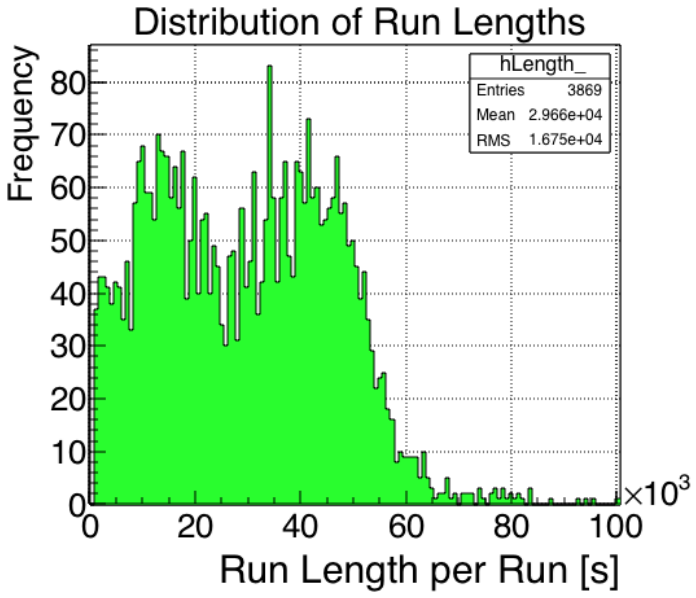

Figure 4.8: Distribution of the length per run for P2 runs.

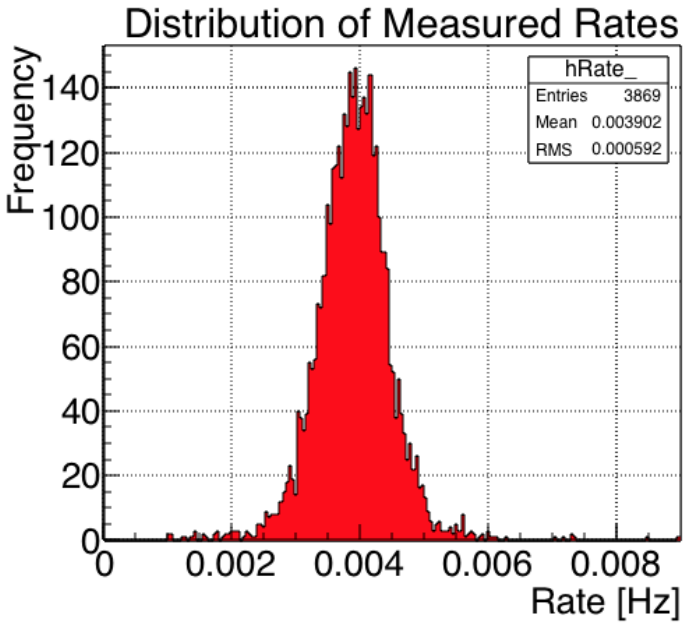

Figure 4.9: Distribution of the rate of ββ decay events per run for P2 runs.

might still record significantly different number of ββ events simply because the overall detection efficiency has changed from one run to the next.

The detector efficiency is found by generating a known number of MC events for a given run and then passing these events through the full trigger, reconstruction, and event selection procedures all while accounting for the same detector conditions as the real data experienced. The efficiency at each stage can be calculated as the ratio of the number of events remaining after processing over the number of events before processing. The total efficiency, which is used for scaling the data, is a product of the efficiencies at each step and thus is given by the number of events which pass the selection criteria divided by the number of total MC events initially generated.

Efficiency Scaling

For the i^{th} run the total detector efficiency for that period of time is given by,

$$\epsilon_i = \frac{N_i^{\text{selected}}}{N_i^{\text{generated}}}. \tag{4.6.1}$$

The error is taken as the binomial error given by

$$\Delta\epsilon_i = \sqrt{\frac{\epsilon \times (1-\epsilon)}{N_i^{\text{generated}}}}. \tag{4.6.2}$$

This efficiency quantity differs from one search channel to the next or one isotope to the next as it is highly dependent on both the topologies being searched for and what sectors of the detector they originate in. This detector efficiency as a function of run is shown in figure 4.10.

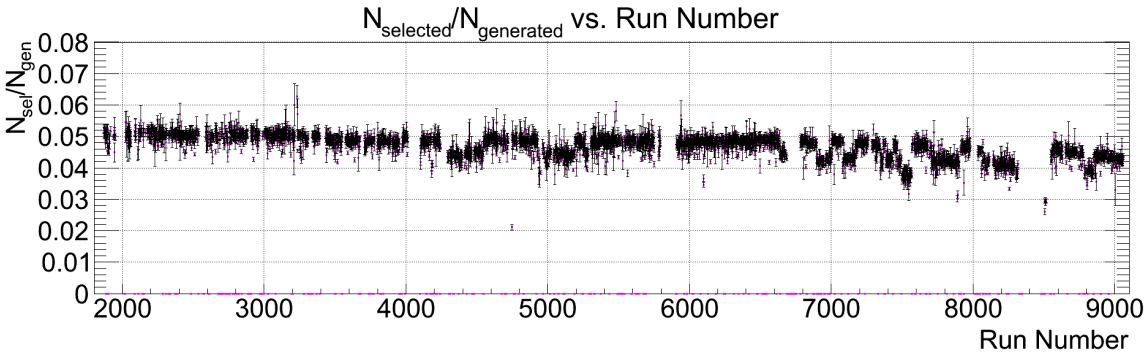

Figure 4.10: An illustration of how the detector efficiency changes as a function of the run index (called the run number). Since later runs have a larger index this shows how the detector efficiency evolves in time over the lifetime of the detector.

Since run number is just an index that increases with subsequent runs, this plot shows how the detector efficiency evolved over the course of NEMO-3's lifetime. As expected with aging equipment there is an overall negative trend in the efficiency as a function of time. Towards the end of NEMO-3's life there are also occasional large drops in efficiency as whole portions of the detector suffered issues (such as HV board replacements or PMT failures) which prevented some components from being

used in event detection or analysis. Even if the geometrical acceptance changed due to such effects, as long as the rest of the detector was fully operational the run was still deemed to be of good quality for analysis purposes. Once the efficiency is known for each run, the rate values can be scaled to account for for it. Since the measured decay rates, R_i for each run, should also scale like the number of MC events then

$$\epsilon_i = \frac{N_i^{\text{selected}}}{N_i^{\text{generated}}} = \frac{\mathrm{R}_i^{\text{measured}}}{\mathrm{R}_i^{\text{true}}}, \tag{4.6.3}$$

then one can calculate the true rate of $\beta\beta$ decays as

$$\mathrm{R}_i^{\text{true}} = \frac{\mathrm{R}_i^{\text{measured}}}{\epsilon_i}. \tag{4.6.4}$$

Using these efficiency factors to scale the measured $\beta\beta$ decay rates shown in figure 4.9 produces the new distribution shown in figure 4.11. For completeness and since they will be important in subsequent sensitivity studies (see section 5.2), the distribution of the errors for the scaled rate values is shown as well in figure 4.12.

4.7 Decay Rate Time Series

To build a time series of this decay rate, each rate value is assigned to a time corresponding to the midpoint of the run (this is obtained by taking the time stamp denoting the run start and adding to that half of the run length). Since the length and time between runs is not uniform and there are also long periods of detector shutdown or unacceptable runs, what results is a very unevenly sampled time series with many gaps. The error in the counts is taken by summing in quadrature the standard error due to Poisson statistics on the number of observed events and the error due to the efficiency scaling term. The error in the time assigned to the acquired rate is taken to be the half-length of the run. The resultant decay rate time series is shown below in 4.13.

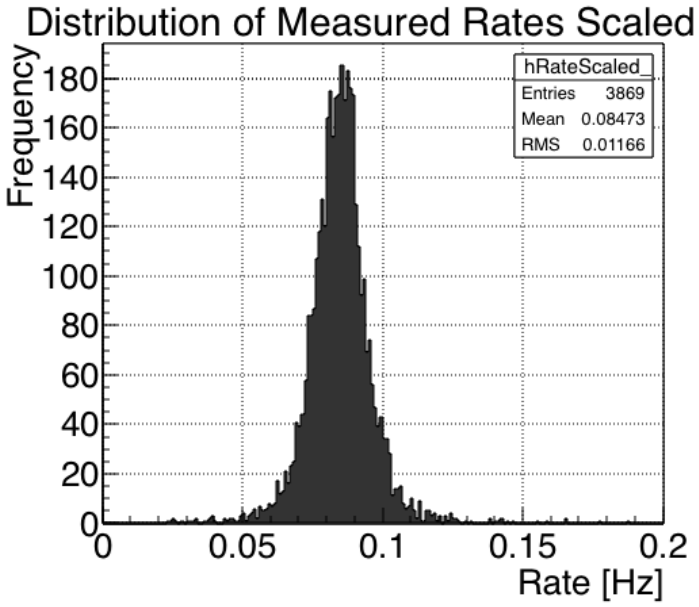

Figure 4.11: Distribution of the efficiency-scaled rate of ββ decay events per run for P2 runs.

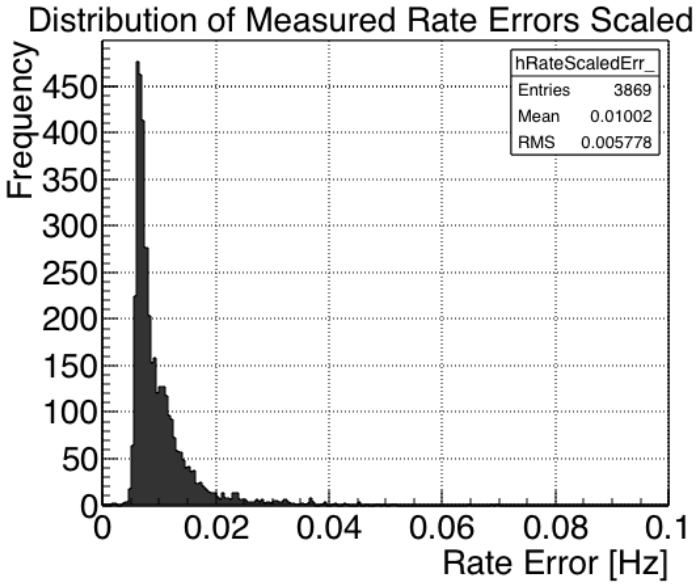

Figure 4.12: Distribution of the efficiency-scaled errors on the rate of ββ decay events per run for P2 runs.

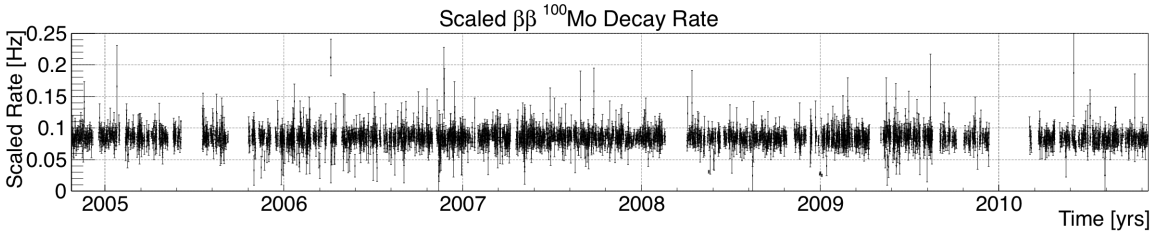

Figure 4.13: An illustration of the efficiency-scaled ββ decay rates versus time for the P2 ^{100}Mo data set.

Chapter Five: Analysis Technique

The general strategy in analyzing the decay rate time series to search for periodicities involves transforming into the frequency domain to decompose the data into its spectral frequency components. The classical method of doing this is known as the periodogram technique in which a quantity known as the "power" is calculated for each frequency that ones desires to sample in a given range. Frequencies that appear with a large power denote a stronger presence in the time series. This technique and its more modern variants are the focus of this chapter as they pertain to the analysis of NEMO-3 $\beta\beta$ decay rates.

The first section of this chapter will introduce the transformation into the frequency domain and construction of the classical periodogram technique as well as its extension in the Lomb-Scargle and then the Generalized Lomb-Scargle technique. A simple example of this technique's application is also shown with a "toy model" data set. Finally the technique is applied to NEMO-3 data for the $2\nu\beta\beta$ decay of ^{100}Mo .

5.1 Frequency Domain Analysis

In analyzing a time series of data one can chose to do so in either the time domain or the frequency domain with the help of the Fourier Transform. In general it is considered that time domain analysis works best for studying random phenomena whereas frequency domain techniques are best suited for studying periodic processes. One of the more commonly encountered problems in the latter case focuses on how to detect these periodic signals embedded within a time series. A well known approach to

this problem is to generate a periodogram allowing one to study the power spectrum of the time series. This essentially breaks down a time series into its component frequencies and denotes those which are strongly present in the data by attributing a large power to them. The details of this technique, are the focus of this section.

The periodogram technique (often also referred to as a power spectrum analysis technique) is a well known classical tool for searching for periodic signals within a time series but a common shortfall was that it was originally designed to work only with evenly spaced data. In many real life applications data must be taken at sporadic intervals and detectors may suffer periodic shutdown periods for maintenance and calibration which introduce gaps into the data taking times. This is a very common issue in Astronomy where weather, telescope viewing times, calibration runs, and more all affect the data taking process. In order to deal with this Jeffrey Scargle, based on work by Nicholas Lomb [80], introduced a variation of the periodogram technique now known as the Lomb-Scargle periodogram [81]. This technique was further generalized to include an offset term and properly account for weighted data by M. Zechmeister and M. Krster [82].

Although developed with particular intentions for use in astronomy, the Lomb-Scargle technique has found use in many fields which require a robust and well proven method for analyzing variability in a time series. As mentioned in Chapter 3, many analyses searching for periodicities in nuclear decay rates have employed similar power spectrum analysis techniques. Additionally, experiments such as the the Super-Kamiokande neutrino observatory [83] and the Sudbury Neutrino Observatory (SNO) [84] have used similar techniques to search for periodic variations in solar neutrino fluxes and the DAMA/LIBRA experiment [68] has also employed a version of it to show evidence of annual modulations in its data. The basics of the technique

are shown in the next section along with the details of the full Lomb-Scargle and Generalized Lomb-Scargle periodograms.

The Classical Periodogram

To begin, an arbitrary time series is defined which mimics a discretely sampled data set: $X(t_t); i = 1, 2, ..., N$. A Discrete Fourier Transform can then be applied to this data to go from the time domain to the frequency domain via

$$FT_X(\omega) = \sum_{j=1}^{N} X(t_j) \exp(-i\omega t_j) \tag{5.1.1}$$

The periodogram can now be constructed by computing, for each sample frequency, the quantity

$$\begin{aligned} P_X(\omega) &= \frac{1}{N}|FT_X(\omega)|^2 \\ &= \frac{1}{N}\left|\sum_{j=1}^{N} X(t_j)\exp(-i\omega t_j)\right|^2 \\ &= \frac{1}{N}\left|\left(\sum_{j=1}^{N} X(t_j)\cos(\omega t_j)\right)^2 + \left(\sum_{j=1}^{N} X(t_j)\sin(\omega t_j)\right)^2\right| \end{aligned} \tag{5.1.2}$$

The above is also often referred to as the power at the chosen sample frequency ω and thus sometimes the terms power spectrum and periodogram are used interchangeably. In fact the power spectrum is technically a theoretical quantity defined as an integral over continuous time whereas the periodogram is an approximation based on summing over finite amounts of discrete data. If the initial time series $X(t_i)$ does in fact contain a sinusoidal component of some frequency ω_0, then when one calculates the value of the power at or near that frequency, that is $P_X(\omega_0)$, the factors $X(t)$ and $\exp(-i\omega t)$ are in phase and contribute to a large value of the power. In other words, when a distribution is made of P calculated at various values of ω, a large value of P near a

particular ω (as a narrow, tall peak in the spectrum) would indicate the presence of a sinusoidal component in the data.

If it is further imposed that the data points are evenly sampled so that $t_j - t_i = \Delta t$ is constant then it can arbitrarily be taken that $\Delta t = 1$ so that $t_j = j$ and $X(t_j) = X_j$. In doing so the second equation above reduces to

$$P_X(\omega) = \frac{1}{N}\left|\sum_{j=1}^{N} X_j \exp(-ij\omega)\right|^2 \tag{5.1.3}$$

Various properties of the periodogram will be discussed in the next section after introducing the modified form known as the Lomb-Scargle periodogram.

The Lomb-Scargle Technique

The Lomb-Scargle periodogram is constructed by making a slight modification to the classical periodogram so that sine and cosine terms are weighted separately. This involves redefining $P_X(\omega)$ from above as

$$P_{LS}(\omega) = \frac{1}{2}\left\{\frac{\left(\sum_{j=1}^{N} X(t_j)\cos[\omega(t_j-\tau)]\right)^2}{\sum_{j=1}^{N}\cos^2[\omega(t_j-\tau)]} + \frac{\left(\sum_{j=1}^{N} X(t_j)\sin[\omega(t_j-\tau)]\right)^2}{\sum_{j=1}^{N}\sin^2[\omega(t_j-\tau)]}\right\} \tag{5.1.4}$$

Where is the τ is defined as

$$\tan(2\omega\tau) = \frac{\left(\sum_{j=1}^{N}\sin(2\omega t_j)\right)}{\left(\sum_{j=1}^{N}\cos(2\omega t_j)\right)}. \tag{5.1.5}$$

The periodogram can be normalized so that the distribution of powers has unit mean by making the simple replacement $X(t_j) \to [X(t_j) - \bar{X}]$ and introducing an overall

factor that depends on the sample variance σ^2 where

$$\bar{X} = \frac{1}{N}\sum_{j=1}^{N} X(t_j) \tag{5.1.6}$$

is the sample mean and the sample variance is given by

$$\sigma^2 = \frac{1}{N}\sum_{j=1}^{N}[X(t_j) - \bar{X}]^2. \tag{5.1.7}$$

In this case the final form of $P_{LS}(\omega)$ becomes

$$P_{LS}(\omega) = \frac{1}{2\sigma^2}\left\{ \frac{\left(\sum_{j=1}^{N}[X(t_j) - \bar{X}]\cos[\omega(t_j - \tau)]\right)^2}{\sum_{j=1}^{N}\cos^2[\omega(t_j - \tau)]} + \frac{\left(\sum_{j=1}^{N}[X(t_j) - \bar{X}]\sin[\omega(t_j - \tau)]\right)^2}{\sum_{j=1}^{N}\sin^2[\omega(t_j - \tau)]} \right\}. \tag{5.1.8}$$

Like the classical periodogram, the Lomb-Scargle periodogram has three very useful properties: (1) it has a very simple statistical behavior, (2) it is time translation invariant, and (3) it is mathematically equivalent to the least-squares fitting of sinusoids to the data. This first property will be further delved into below.

The statistical distribution of the periodogram is one of its most alluring features due to how easily and well understood it is. The fundamental property that makes this so is the fact that if $X(t)$ is pure Gaussian noise (no signal present), the the powers $P_{LS}(\omega)$ follow an exponential distribution. This means that if the substitution $Y = P_{LS}(\omega)$ is made, then the probability distribution is given by

$$p_Y(y)dy = Prob(y < Y < y + dy) = \exp(-y)dy. \tag{5.1.9}$$

The cumulative distribution function can then be calculated as

$$\begin{aligned} CDF_Y(y) = Prob(Y < y) &= \int_0^y p_Y(y')dy' \\ &= 1 - \exp(-y). \end{aligned} \tag{5.1.10}$$

This implies that $Prob(Y > y) = \exp(-y)$ which gives the statistical significance of progressively larger observed powers. In other words, as the observed power increases, the probability that it is due to chance (fluctuations in the Gaussian noise) decrease exponentially.

Consider now the maximum value (largest peak) in the power spectrum by letting $Y = max_n P(\omega_n)$ where n indexes the various sampled frequencies used to construct the power spectrum and runs from 1 to the total number of sampled frequencies M. In this case, $CDF_Y(y)$ must be raised to the power M (for each frequency sampled) so that the above probability now becomes

$$\begin{aligned} Prob(Y > y) &= 1 - CDF_Y(y) \\ &= 1 - [1 - \exp(-y)]^M [Y = max_n P(\omega_n)]. \end{aligned} \tag{5.1.11}$$

This implies that searching more frequencies brings with it a statistical penalty in that a larger power is required to yield the same probability as M is increased. Note, this probability is sometime also referred to as the false alarm probability since it gives the probability that random fluctuations due to noise are detected as a signal.

At this point, a natural extension is to interpret of the significance of a peak in terms of a confidence level (C.L.) which can be defined from the probability above as

$$\begin{aligned} C.L. &= [1 - Prob(Y > y)] \times 100 \\ &= [1 - \exp(-y)]^M \times 100. \end{aligned} \tag{5.1.12}$$

So that a probability of $Prob(Y > y) = 0.01$ corresponds to a peak peak with significance given by a 99% confidence level ($C.L. = 99\%$).

The last issue discussed here concerns the estimation of the detection threshold for a given statistical significance. In other words, what is the necessary power of a peak in a PSD such that detection can be claimed at a predetermined C.L.? For this,

consider the false alarm probability p, corresponding to that C.L. via equation 5.1.12, and recall equation 5.1.11). This relation can be rearranged to solve for the value of the LS power, $y_{threshold}$, such that anything larger would be statistically significant at or above the desired C.L. This is derived below:

$$\begin{aligned} p = Prob(Y > y) &= 1 - [1 - \exp(-y)]^M [Y = max_n P(\omega_n)] \\ [1 - \exp(-y_{threshold})]^M &= 1 - p \\ \exp(-y_{threshold}) &= [1 - (1-p)^{1/M}] \\ y_{threshold} &= -\ln[1 - (1-p)^{1/M}]. \end{aligned} \tag{5.1.13}$$

As mentioned previously, M acts like a statistical penalty for sampling a larger number of frequencies so as M is increased, so too is the threshold power required for detection at a chosen C.L. In general M is often taken to be twice the number of data points since it is assumed that the number of independent frequencies is equal to the number of data points.

The Generalized Lomb-Scargle Technique

In order to generalize the Lomb-Scargle periodogram to account for data weights (uncertainties) and an offset term, recall first that the Lomb-Scargle periodogram technique is equivalent to the least-squares fitting of sinusoids to a given data set. In [81], it is shown that if one begins with a model fit function,

$$X_{fit}(t) = A\cos(\omega t) + B\sin(\omega t), \tag{5.1.14}$$

and then seeks to minimize the mean square difference between this model and one's data according to

$$E(t) = \sum_{j=1}^{N} [X(t_j) - X_{fit}(t_j)]^2, \tag{5.1.15}$$

one finds that this is equivalent to maximizing a function which is identical to that for $P_{LS}(\omega)$ (see equation 5.1.4). Suppose one now begins with a model function that includes an offset term,

$$X_{fit}(t) = A\cos(\omega t) + B\sin(\omega t) + C, \tag{5.1.16}$$

and one now proceeds using a χ^2 minimization taking data errors, σ_j, into account according to

$$\chi^2(\omega) = \frac{\sum_{j=1}^{N}[X(t_j) - X_{fit}(t_j)]^2}{\sigma_j^2} = W\sum_{j=1}^{N} w_j[X(t_j) - X_{fit}(t_j)]^2, \tag{5.1.17}$$

where

$$w_j = \frac{1}{W}\frac{1}{\sigma_j^2} \text{ and } (W = \sum_{j=1}^{N}\frac{1}{\sigma_j^2}) \tag{5.1.18}$$

are the normalized weights. It is then shown in [82] that, in a similar approach as that used by Scargle in [81], one can minimize this function by maximizing,

$$\begin{aligned} P_{GLS}(\omega) &= \frac{\chi_0^2 - \chi^2(\omega)}{\chi_0^2} \\ &= \frac{1}{XX\cdot D(\omega)}[SS\cdot XC^2 + CC\cdot XS^2 - 2CS\cdot XC\cdot XS], \end{aligned} \tag{5.1.19}$$

where

$$\chi_0^2 = W \cdot XX \tag{5.1.20}$$

$$D(\omega) = CC \cdot SS - CS^2 \tag{5.1.21}$$

$$XX = \sum_{j=1}^{N} w_j [X(t_j) - \bar{X}]^2 \tag{5.1.22}$$

$$XC = \sum_{j=1}^{N} w_j [X(t_j) - \bar{X}] \cos(\omega t_j) \tag{5.1.23}$$

$$XS = \sum_{j=1}^{N} w_j [X(t_j) - \bar{X}] \sin(\omega t_j) \tag{5.1.24}$$

$$CC = \sum_{j=1}^{N} w_j \cos^2(\omega t_j) - [\sum_{j=1}^{N} w_j \cos(\omega t_j)]^2 \tag{5.1.25}$$

$$SS = \sum_{j=1}^{N} w_j \sin^2(\omega t_j) - [\sum_{j=1}^{N} w_j \sin(\omega t_j)]^2 \tag{5.1.26}$$

$$CS = \sum_{j=1}^{N} w_j \cos^2(\omega t_j) \sin(\omega t_j) - [\sum_{j=1}^{N} w_j \cos(\omega t_j) \times \sum_{j=1}^{N} w_j \sin(\omega t_j)] \tag{5.1.27}$$

$$\bar{X} = \sum_{j=1}^{N} w_j X(t_j). \tag{5.1.28}$$

Since time-translation invariance still holds, it is possible to once again introduce a time reference factor, $\hat{\tau}$, such that the equation for $P_{GLS}(\omega)$ reduces to the following simpler form (which is very similar to the expression for $P_{LS}(\omega)$)

$$P_{GLS}(\omega) = \frac{1}{XX} \left\{ \frac{XC_{\hat{\tau}}^2}{CC_{\hat{\tau}}} + \frac{XS_{\hat{\tau}}^2}{SS_{\hat{\tau}}} \right\}, \tag{5.1.29}$$

where

$$\tan(2\omega\hat{\tau}) = \frac{2CS}{CC - SS} \tag{5.1.30}$$

and the subscript $\hat{\tau}$ in each of the sine and cosine terms denotes replacing the argument with $\omega(t_j - \hat{\tau})$ instead of ωt_j.

A convenient feature of the LS periodogram technique is that the powers are exponentially distributed with unit mean which allows for simple calculations of the false alarm probabilities and C.L. values. In order for the same to hold true for the GLS periodogram, the $P_{GLS}(\omega)$ much be properly normalized to follow a similar distribution as the Lomb powers. In [82] it is noted that this can be done with the substitution,

$$\begin{aligned} Z(\omega) &= \frac{N-2}{3} \ln \frac{\chi_0^2}{\chi^2(\omega)} \\ &= \frac{N-2}{3} \ln \frac{1}{1-P(\omega)}, \end{aligned} \tag{5.1.31}$$

so that the probability distribution once again follows an exponential form according to

$$Prob(Z > z) = \exp(-z). \tag{5.1.32}$$

One can then follow the exact same prescription as before to calculate the false alarm probability and assign C.L. values to peaks in the GLS periodogram.

Toy Model Example

To illustrate the technique an arbitrary time series is constructed on which to apply it. The function $X(t_j)$ is generated by randomly choosing values from a Gaussian with unit mean and a width of 10% and then assigning these to arbitrary times t_j. Since this technique is intended to work on unevenly sampled data some randomization is added into the temporal spacing between points and some points or groups of points are also removed arbitrarily to create uneven gaps in the time series. The resultant tailored time series will mimic true NEMO-3 data much more closely.

The Lomb-Scargle periodogram is then constructed by calculating the power for each frequency in a large sample set. In general, these frequencies are limited from

below by the full range of the data ($\omega_{min} = 2\pi/\frac{1}{2}T_{max} = 4\pi/t_n - t_0$) and limited from above by the time between data points ($\omega_{max} = 2\pi/2T_{min} = \pi/t_{j+1} - t_j$). For this example,this range was subdivided into 1000 evenly spaced frequencies at which to calculate the Lomb power ($P_{LS}(\omega)$). As discussed in the previous section, corresponding confidence levels (C.L.) can then be calculated for each peak which can be used to construct a distribution of C.L. values as a function of sample frequency. Figure 5.1 shown below illustrates the examples time series along with its constructed PSD and distribution of associated C.L. values over the range of sampled frequencies. Since the time series was purely Gaussian random values, there should be no underlying periodic modulations in the signal. This is verified by the lack of any significantly large peaks in the PSD.

A modulation can now be introduced into this same time series of the form

$$X'(t_j) = X(t_j) + \bar{X} \times A \times sin(2\pi t_j/T) \tag{5.1.33}$$

Where $\bar{x}$ is the average of the $X(t_j)$ values, A is the normalized amplitude of the modulation relative to the mean, and T is the period of the modulation (left in arbitrary units for this example). These variables are then set to arbitrary values to demonstrate the detection of this modulation. If $T = 30$ and $A = 0.05$ (A 5% modulation amplitude) then the resultant time series along with its PSD and C.L. distribution is shown below in figure 5.2. The presence of a large peak in the PSD with a power ≈ 13 located at $\omega = 0.032975$ can be seen. This corresponds to a period $T_{measured} = 1/\omega = 30.3260$ which differs from the true value of T by about 1.09%. Furthermore, this peak corresponds to a statistically significant peak at the C.L. of 99.9994%.

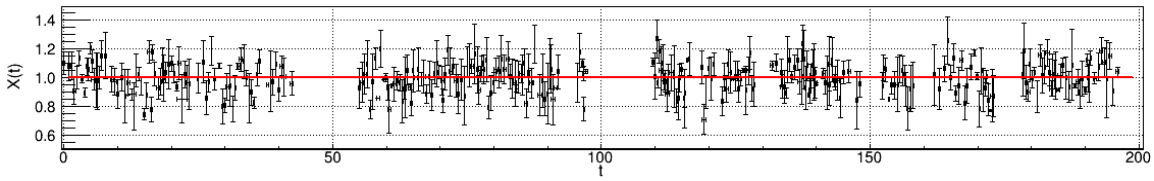

(a) Sample Time Series

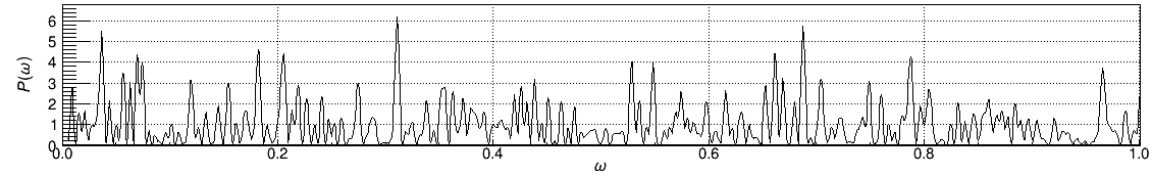

(b) Sample PSD

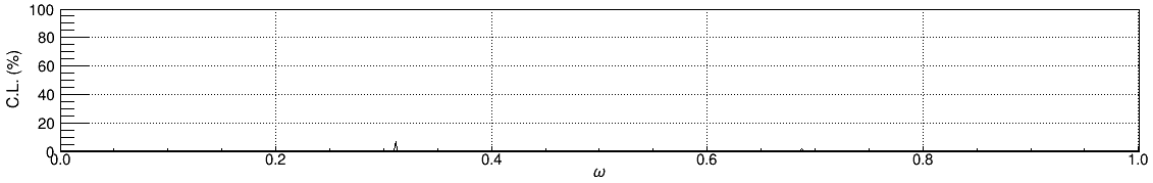

(c) Sample C.L. Distribution

Figure 5.1: An illustration of how the LS periodogram technique is applied is demonstrated by using it on an arbitrary unevenly sampled time series. The time series is generated by randomly sampling values from a Gaussian distribution of unit mean (hence the best fit line to the data is given by the horizontal red line at $X = 1$). Since this time series should have no periodic component to it, no statistically significant peaks appear in its PSD.

5.2 ββ Decay Rate Analysis Results

The analysis of NEMO-3 data was kept blinded until all stages of the approach were verified and approved and the final frequency search parameters were established. This was done by either avoiding the construction of the final time series and using just the information of the scaled rate distributions when possible or by scrambling the scaled rate values with respect to the times of their corresponding runs. The latter approach destroyed the temporal ordering of the data so that any underlying

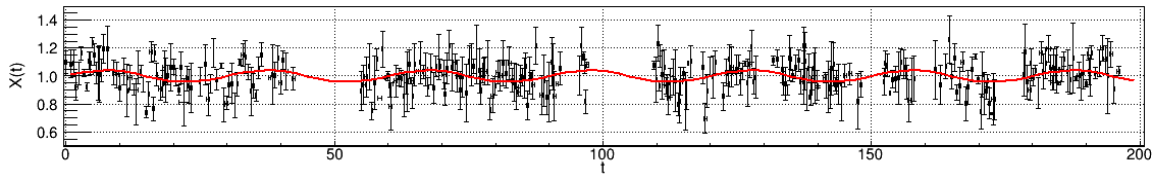

(a) Sample Time Series

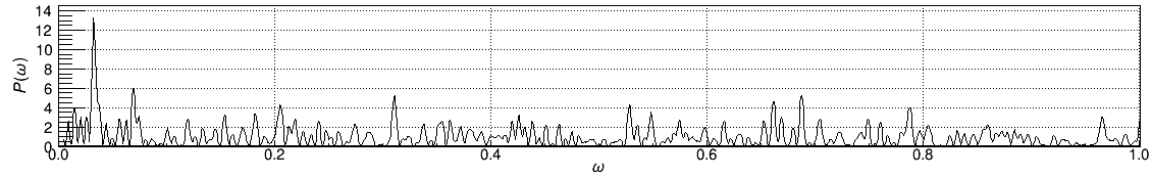

(b) Sample PSD

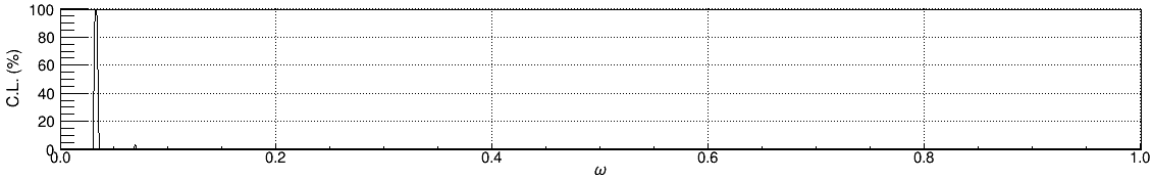

(c) Sample C.L. Distribution

Figure 5.2: The previously shown example of the LS periodogram technique is now repeated after introducing a sinusoidal modulation into the time series (with modulation shown in red). This produces a statistically significant peak to appear in the PSD at a frequency matching that true values to within a couple percent

periodicities were washed out of the data. Once ready, this temporal scrambling was simply omitted when constructing the final scaled decay rate time series. As mentioned in section 4.5, the first data set which was un-blinded and analyzed was the P1 data for ^{100}Mo $\beta\beta$ decay rates. Application of the LS and GLS techniques on the blinded and then un-blinded P1 data sets revealed two issues which were subsequently corrected before analysis of the un-blinded P2 data.

The first issue, noticed in both the blinded and un-blinded P1 data sets, had to do with a specific set of outlier data points which caused incongruous results between the LS and GLS techniques. Although the LS powers calculated for these P1 data

sets followed the expected exponential distribution with unit mean, the GLS powers were much larger than unity on average and follow more a linear distribution. This resulted in a highly erratic periodogram in which almost all peaks were assigned very high C.L. values (large significance) at or very near 100%. In general, most outlier runs with rates which deviate from mean have correspondingly large errors so that the GLS technique doesn't weigh them highly in calculating the periodogram values. The problem occurs when runs have highly inconsistent rates **but** very small uncertainties. Since the GLS periodogram technique is equivalent to a least-squares fitting of sine-waves to the data, this failure can be understood in the same way that fits can fail to converge when the data has highly weighted points that don't agree with any variations of the fit parameters. When such runs were removed from the time series, the LS and GLS results once again agreed and both returned sensible values for periodogram powers. In order to remove this class of runs a cut was made on an unsigned χ value given by

$$\chi_i = \frac{(R_i - \bar{R})}{\sigma_i}, \tag{5.2.1}$$

where R_i is the rate value of the i^{th} run, σ_i is its uncertainty, and $\bar{R}$ is the average rate value over all the data. This is essentially a measure of how far removed a run is from the rest of the data in units of its uncertainty. Various values of χ between 2 and 200 were tested as values on which to cut runs from the P1 times series. This means that runs with χ values at or larger than the cut value were removed. The results of testing various cut values are shown in table 5.1.

Small scale studies showed that the detection sensitivity of the data was largely unaffected so long as only 10% or less of the data points were removed at random (non-consecutive points) from the time series. Furthermore, the studies also showed that even the next-to-least stringent cut, at $\chi = 100$, was sufficient to restore the

χ Cut Value	Runs Cut	Runs Kept	Percentage of Data Kept
2	323	587	64.5%
5	65	845	92.6%
10	33	877	96.4%
20	21	889	97.7%
50	17	893	98.1%
100	16	894	98.2%
200	2	908	99.8%

Table 5.1: Summary of the results of cutting runs with various χ values.

agreement between the LS and GLS techniques. With the above considerations, the final cut value to be applied to P2 data prior to un-blinding was chosen at $\chi = 10$. In the P1 data such a cut removed less than 5% of the runs. Although both P1 and P2 data sets contain these kind of outlier runs, the P1 data set suffers from a much larger population of such runs. The same cut applied to P2 data only eliminated a total of 4 runs and kept about 99.9% of the data. Although an investigation was undertaken in order to understand why certain runs had such irregular values, no concrete evidence was found (with the limited time available) which would point to particular run or detector properties as the culprit.

The second issue, notice with un-blinded P1 data, was that linear trends in the data, whether by chance or due to a systematic effect, were found to produce a large peak in the LS and GLS periodograms at the smallest sample frequency ($f_{min} = 0.083063\,\mathrm{yrs}^{-1}$). This feature was reasonably well contained only in this end-point of the periodogram meaning that the removal of the linear trend would not affect the search at other frequencies. To achieve this, the time series was fitted with a linear

function and then divided by the resulting function to produce a normalized decay rate time series with mean rate value equal to one and no linear trend. Re-applying the LS and GLS techniques to the de-linearized P1 data verified that the peak at f_{min} disappeared.

With these two issue solved, the un-blinding of the P2 data proceeded after applying applying the χ value cut and de-linearizing the data. Both the LS and GLS technique were applied to this normalized time series to search for periodic modulations. The total data set consists of 3865 runs. An oversampling factor of two was chosen meaning that $7730 = 2 \times 3865$ different frequency values were sampled. These frequencies are evenly distributed in the range $[0.08306, 356.25]\,\mathrm{yrs}^{-1}$ and were chosen based on the maximum and minimum modulation periods that should be feasibly detectable with the given data set. Periods that are shorter than the average time between runs will not be detectable with data set. This lower bound on sample periods sets an upper bound on the sample frequencies at about $f_{max} = 1/(2 \times \bar{\Delta T_i}) \approx 1\,\mathrm{day}^{-1} = 365.25\,\mathrm{yrs}^{-1}$. Similarly, modulation periods that are longer than the total span of the data set, approximately 6.02 years, will not be contained as a complete wave form within the data. Although still detectable, the sensitivity begins to drop when when only partial waveforms are present in the data (see section 5.2 for sensitivity studies). the upper limit on the period is thus taken as twice the span of the data so that the minimum sample frequency is $f_{min} = 1/(2 \times \mathrm{span}) \approx 1/12.04 = 0.08306\,\mathrm{yrs}^{-1}$. This still allows for the detection of previously claimed periodicities (see section 2.4) in the data from BNL decay rates, DAMA/NaI, and Super-Kamiokande. The results of this search are shown below in figure 5.3 and follow the same format as the toy model example shown in the previous section; the time series (normalized and with secular trends removed), followed by

the periodogram (made using both the LS and GLS techniques), and the distribution of confidence level values for each PSD peak.

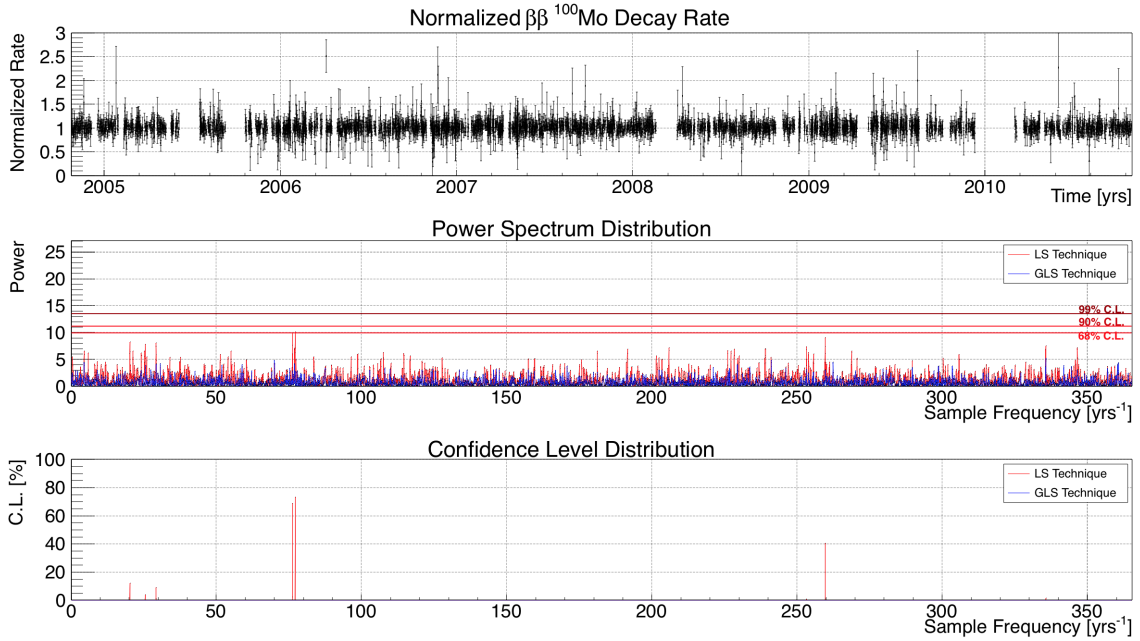

Figure 5.3: Results of applying the GLS and LS periodogram techniques to the ββ decay rate time series of P2 ^{100}Mo data in the full frequency range. The upper plot shows the time series that was analyzed. The middle plot shows the periodogram for the LS technique in red and the GLS in blue. The lower plot shows the C.L. values for each peak in the periodograms with red and blue again corresponding the the LS and GLS techniques respectively.

The results of the periodogram analysis are summarized in table 5.2.

	LS Results	**GLS Results**
Max Power	10.13	5.16
Max Power Frequency	$77.18\,\mathrm{yrs}^{-1}$	$335.68\,\mathrm{yrs}^{-1}$
Max Power Confidence Level	73.37%	0.00%

Table 5.2: Summary of results from applying the LS and GLS technique to the ββ decay rates for P2 ^{100}Mo data in the frequency range $[0.08306, 365.25]\,\mathrm{yrs}^{-1}$.

Both techniques produce periodograms with no highly significant peaks ($C.L. >$

90%). Furthermore, the largest peak in each periodogram correspond to different frequencies, which can be considered as another indication that their significance is purely due to statistical fluctuations rather than a true periodic trend. Although convenient, the simple approach of calculating the significance of peaks based on the expected behavior of the PSD is not the most robust as it assumes a certain distribution of powers *a priori*. The next section, 5.2, explains a more widely accepted approach based on MC techniques. An extension of this is also used in section 5.2 to estimate detection sensitivities to different periodic signals. These studies are then used to set limits in terms of real-world parameters such as the amplitude of a potential modulation with at a specific frequency.

In order to check the validity of the claims made by Sturrock and others, which were summarized in section 2.4, the data was re-analyzed in the same frequency range that those authors used. In the power spectral analyses performed by the authors in [55] [69] and [70], the largest peaks were found at $1\,\mathrm{yrs}^{-1}$, $11.17\,\mathrm{yrs}^{-1}$, $11.47\,\mathrm{yrs}^{-1}$, and $12.5\,\mathrm{yrs}^{-1}$. Upon re-analyzing the P2 $\beta\beta$ decay rate of ^{100}Mo in 7730 frequencies between $[0.08306, 20]\,\mathrm{yrs}^{-1}$, no significant powers are found at the above frequency values noted by Sturrock et al. The LS and GLS powers and corresponding C.L. values summarized in table 5.3. The same plots as shown in figure 5.3 were also re-created but with the periodogram and C.L. distributions corresponding to the new frequency range. This is shown in figure 5.4 with vertical magenta lines denoting the specific frequencies claimed by Sturrock et al.

Null Hypothesis Significance Testing

Monte Carlo (MC) data sets were generated re-evaluate the significance of the previous results and study the sensitivity of the data to detection periodicities with

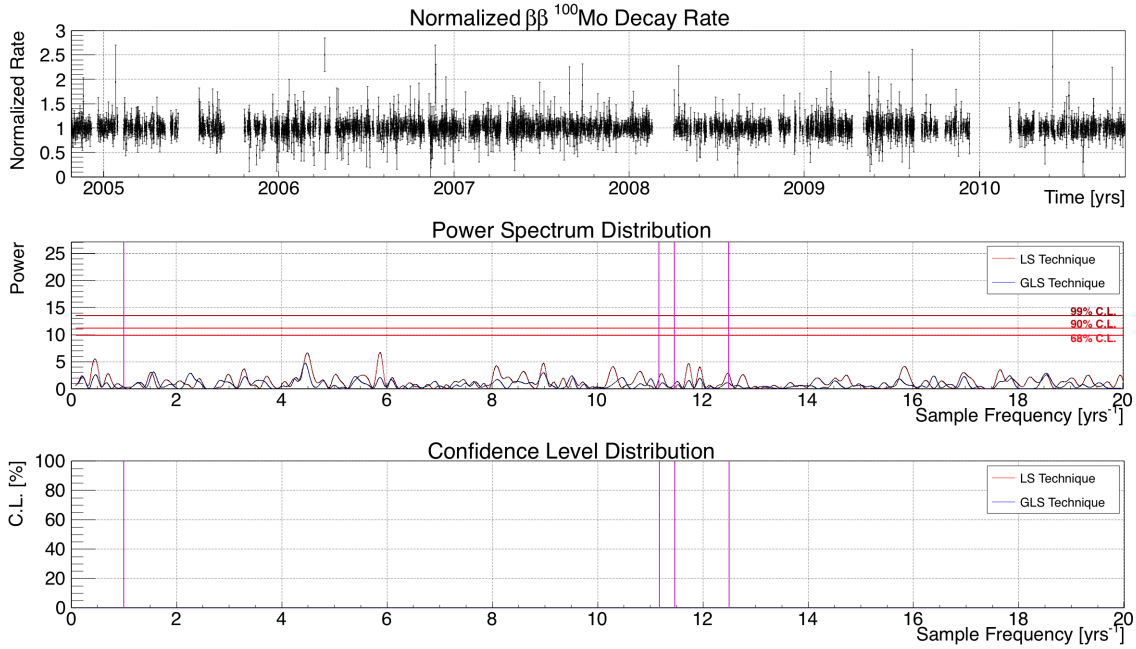

Figure 5.4: Results of applying the GLS and LS periodogram techniques to the ββ decay rate time series of P2 ^{100}Mo data in the reduced frequency range. The time series remains the same but the periodogram and C.L. distributions reflect this new range of sample frequencies. The vertical magenta lines denote the frequencies of interest cited in analyses by Sturrock et al.

various parameters (amplitudes, frequencies, and phases). The true NEMO-3 data distributions of the scaled rate values and their errors (shown previously in figures 4.11 and 4.12 respectively) are used to randomly generate similar data and assign these "pseudo-data" values to identical times as in the true data. In this way the MC time series have the same temporal structure but the random nature of the rate values means that they should have no underlying periodic structure. The pseudo-rate values are pulled from a Gaussian distribution with mean and sigma taken from fitting the true scaled rates distribution. Similarly, the pseudo-rate errors are taken from a Landau distribution with most-probable-value and sigma taken from fitting the true scaled rate errors distribution.

In order to re-assess the statistical significance of the LS and GLS results, 10,000

Frequency [yrs^{-1}]	**LS Power**	**LS C.L.**	**GLS Power**	**GLS C.L.**
1.000	0.296	0.000%	0.0002	0.000%
11.17	1.807	0.000%	0.0002	0.000%
11.47	0.220	0.000%	0.0007	0.000%
12.50	2.702	0.000%	0.0008	0.000%

Table 5.3: Summary of results from re-applying the LS and GLS technique to the $\beta\beta$ decay rates for P2 ^{100}Mo data in the frequency range $[0.08306, 20]\,\mathrm{yrs}^{-1}$. Rather than denoting the largest powers in the periodograms, the powers and C.L. values are given for frequencies corresponding to those where Sturrock et al. have claimed large powers in [55] [69] and [70].

such MC time series are generated with no modulation. This is done by randomly sampling values form a Gaussian distribution with the same mean and RMS as the real scaled rates. In the case of the errors, which more closely follow a Landau distribution, the Landau MPV (most probable value) and sigma were used to randomly sample and assign error values to the data. These time series constituted what is known as the "null-hypothesis" (no periodic modulation) data sets. These were then processed in the same manner as the true data, applying both the LS and GLS techniques, to determine the probability that a randomly chosen time series would produce a false positive detection at a certain confidence level. For each of the 10,000 data sets, a distribution of the largest LS and GLS powers can be found in figures 5.5 and 5.6.

Considering the largest LS (GLS) power observed in the data, 10.13 (5.16), there are approximately 20.17% (100%) of null hypothesis data sets with maximal LS (GLS) power above this value. This means that the significance of the largest LS (GLS) power in the data can be estimated to be at the 79.83% C.L. (0% C.L.). For the LS technique, the simple estimate of the C.L. and the MC-based estimate differ by about 8% where as in the case of the GLS technique they agree completely since even the

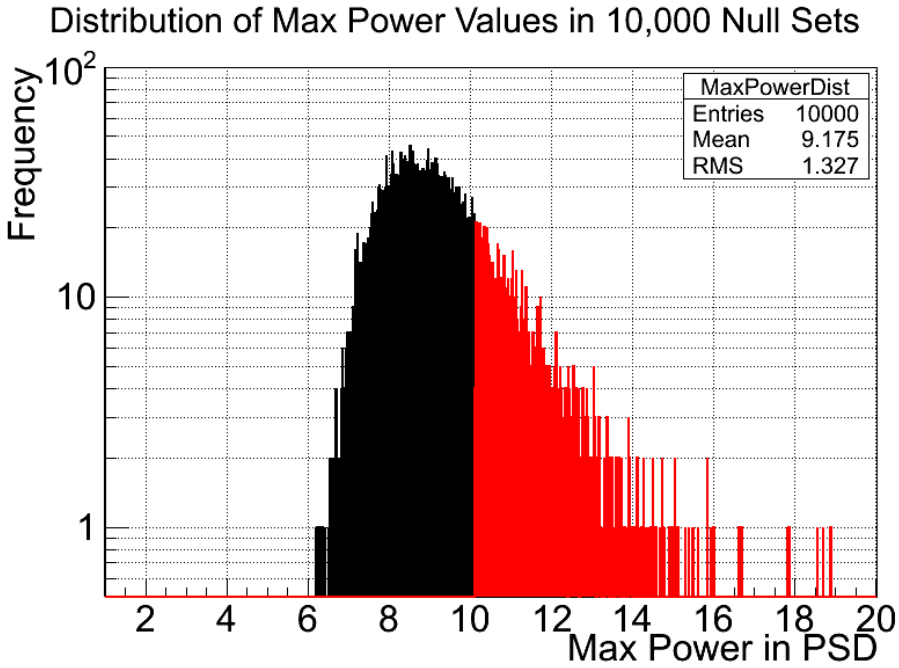

Figure 5.5: A distribution of the maximal LS powers in 10,000 randomly generated MC null hypothesis data sets (no applied modulations). The data sets with maximal power greater than the maximum LS power observed in the data are shown in red and constitute 20.17%. This means the significance of the observed maximum LS power in the data is at the 79.83% confidence level.

maximal power has such low significance.

Sensitivity

A similar approach of using MC time series is also employed to study the sensitivty of NEMO-3's data to detecting a periodic modulation. Rather than analyzing MC data sets which consist of purely random Gaussian noise, a modulation of the rate values is applied so that the data is sampled from a distribution that looks like

$$R(t_i) = N(1 + A \times \sin(2\pi f t_i + \phi)), \tag{5.2.2}$$

where N represent a normalization constant to match the mean of the un-modulated data, A represents a fractional or relative amplitude (which will be denoted in terms

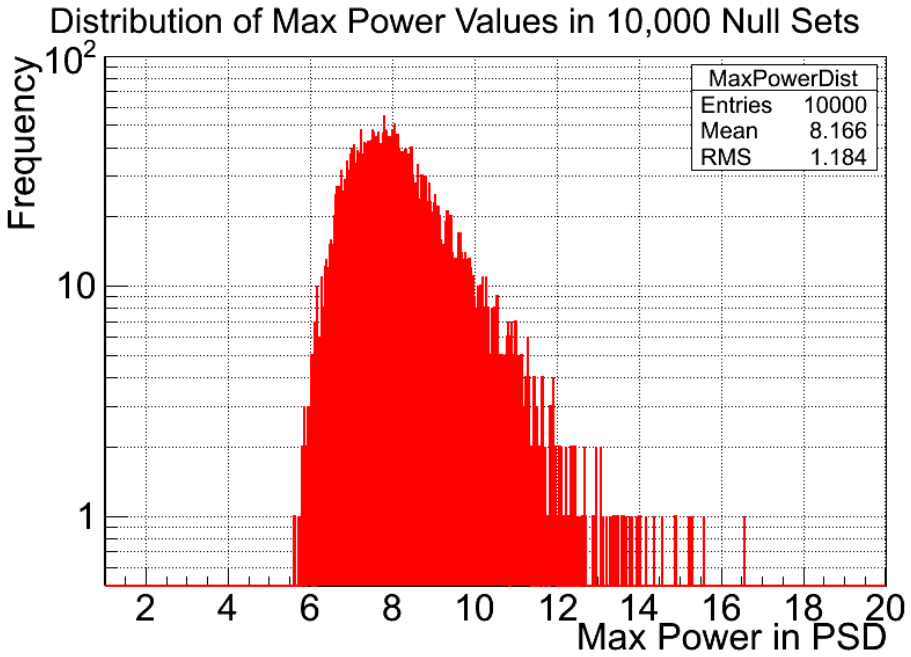

Figure 5.6: A distribution of the maximal GLS powers in 10,000 randomly generated MC null hypothesis data sets (no applied modulations). The data sets with maximal power greater than the maximum GLS power observed in the data are shown in red and constitute 100%. This means the significance of the observed maximum GLS power in the data is at the 0% confidence level.

of a percentage relative to the mean value) for the applied modulation, f is the frequency of the applied modulation, and ϕ is the modulation phase. It is important to note that the phase component of the applied modulations only becomes important when the frequency is very small (the period is very large) meaning that only very few complete wave-forms fit within the span of the data. Otherwise the phase introduces a inconsequential shift since the periodogram has many wave-forms present in calculating the power at a given frequency. Because of this, only the (A,f) parameter space is truly probed in depth in the sensitivity studies. This results in a much simpler analysis of a two dimensional space. The phase parameter is then varied, in significant increments, only when considering low frequencies to see how sensitivity contours are shifted in this 2D space.

Since the LS and GLS techniques are computationally intensive due to the large number of sample frequencies searched, applying them repeatedly over a large phase space of A and f values requires a significant investment of computing resources. For this reason, input modulation frequency values are divided into three regions of interest: low range, mid range, and high range. These ranges were chosen to study the sensitivity to specific periodicities that might be expected. For example, the low range values include modulations with periods in the range of 10-15 years which might be expected if solar synodic rotation rates are influencing the data [70]. Similarly, the mid range values include periodicities with yearly variations such as those claimed in [52]. Lastly, the high range values could be useful in capturing short term variations due to immediate environmental effects such as daily temperature changes. In each range the spacing between adjacent modulation frequency values is also changed to keep the number of trials manageable. These ranges for A and f are summarized below in the table 5.4. All of the input modulation ranges for A and f were optimized by first testing things over a larger range of values, and large binning, to determine where the important transitions happened.

	Amplitude (A) [%]		**ΔA [%]**	**N Values**
	0.5 - 4		0.1	36
	Frequency (f) [$\mathbf{yrs^{-1}}$]	**Period (T) [yrs]**	**Δf [$\mathbf{yrs^{-1}}$]**	**N Values**
Low Range	0.03 - 0.1	10 - 33.3	0.005	15
Mid Range	0.15 - 2	0.5 - 6.66	0.05	38
High Range	15 - 360	0.0028 - 0.067	15	24

Table 5.4: Summary of the various frequency ranges and spacings used for the injected modulation signals.

In total the phase space consisted of 2,772 values ($36 \times (15 + 38 + 24)$). Because each modulation will result in slightly different results from one set of pseudo-data to the next, a total of 100 of MC time series are used for each point in the parameter space. Thus the technique was executed for a total of 277,200 iterations. Every iteration resulted in a periodogram where the largest power was returned along with its corresponding significance and detection frequency. A contour plot was then constructed for each MC data set in which the significance, denoted by the z-axis value (or color), was plotted as a function of input modulation parameters. The results at each bin were then averaged over the 100 total MC data sets to smooth out statistical fluctuations in the peak significance level. The resultant sensitivity plots, broken down by frequency regime, are shown in figure 5.7 for the LS technique and in figure 5.8 for the GLS technique.

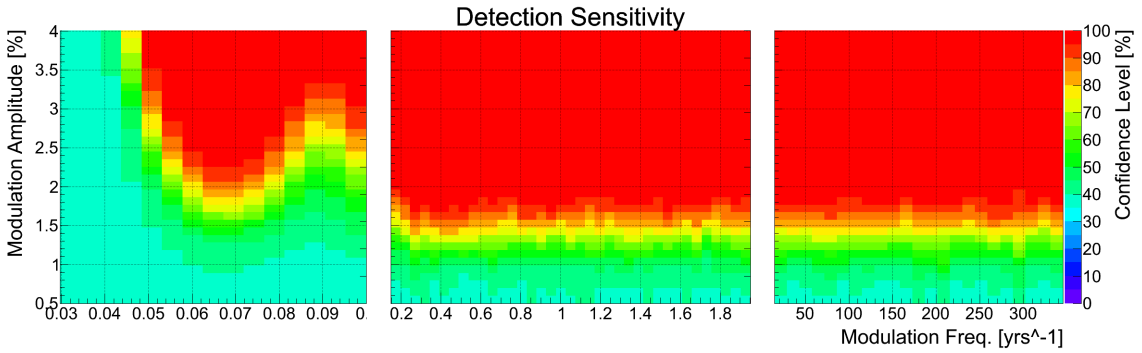

Figure 5.7: An illustration of how the LS detection sensitivity changes as the input modulation parameters A and f are varied (for three different frequency regimes - low, mid, and high). The Z-axis, color, at each point denotes the significance (in terms of C.L. value) of the largest peak, averaged over 100 periodograms.

As expected, it becomes easier to claim detection for a signal, with high confidence, as the modulation amplitude is increased. For detection at or above the 90% confidence level it can be seen that a lower limit modulation amplitude can be set for most of the frequencies (particularly in the mid and high regimes). This limiting

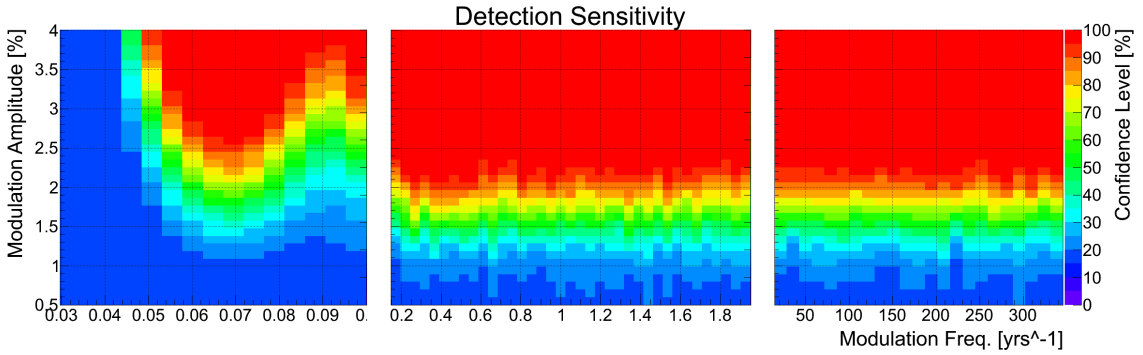

Figure 5.8: An illustration of how the GLS detection sensitivity changes as the input modulation parameters A and f are varied (for three different frequency regimes - low, mid, and high). The Z-axis, color, at each point denotes the significance (in terms of C.L. value) of the largest peak, averaged over 100 periodograms.

amplitude for the $\beta\beta$ decays of ^{100}Mo P2 data occurs at about the 1.7% and 2.1% modulation amplitude levels for the LS and GLS techniques respectively. In other words, the NEMO-3 data would should be able to reasonably detect a periodic modulation at the 90% C.L. if it has a relative amplitude of at least 1.7% when using the LS technique alone or 2.1% when using the GLS technique. The reason for the difference in the limiting amplitudes for the two techniques has to do with the fact that one, the GLS periodogram, weighs the data according to its uncertainty while the other, the LS periodogram, does not. This means that runs which have much larger uncertainties than the average run are almost ignored in the periodogram construction in the GLS technique so that it is effectively using fewer runs. Since the sensitivity to detection scales with the number of data points in the times series this results in a reduced sensitivity for the GLS technique for the LS technique.

The response of the sensitivity with respect to the modulation frequency is mostly flat for all of the mid and high range frequency values but this changes in the low range regime. In the low frequency regime there is a peak in the detection sensitivity at a particular frequency of about $0.07\,\mathrm{yrs}^{-1}$ which corresponds to a period of about

14.3 years (nearly 2.4 times the span of the data set). At these periods the data set is only capturing a part of the full modulation waveform and it is expected that the phase of the modulation begins to play an important role. For this reason the detection sensitivity in the low frequency regime was re-tested for various phase values and the results are discussed in more detail in section 5.2.

A logical follow up inquiry would be to ask if, in the case of detection at high significance such as 90%, does the detected frequency match the true input modulation frequency that was applied to the MC data. To study this, every point in the previous sensitivity plots at which a detection had a C.L. value at or above 90%, the relative error between the true and measured frequency values was calculated. Plots were then made showing the same (A,f) parameter space bit with the Z-axis or color now representing the relative error define as

$$\%\text{Error} = 100 \times \frac{|f_{\text{true}} - f_{\text{detected}}|}{f_{\text{true}}}. \tag{5.2.3}$$

The resultant detection error plots are shown in figure 5.9 for the LS technique and in figure 5.10 for the GLS technique. The plots indicate that at the boundaries of the 90% C.L. contour the detection error is high, mainly for mid and low frequencies, but it drops drastically for signals with higher C.L. values (at higher modulation amplitudes).

Phase Dependence at Low Frequencies

The modulation function applied to the pseudo-data time series in the above studies also included a phase term but it was set to zero in all previous instance of applied modulations. From heuristic arguments, as long as the time series contains many full cycles of the periodic modulation within the time span, the phase should not significantly affect the detection sensitivity of the LS technique. When dealing with very

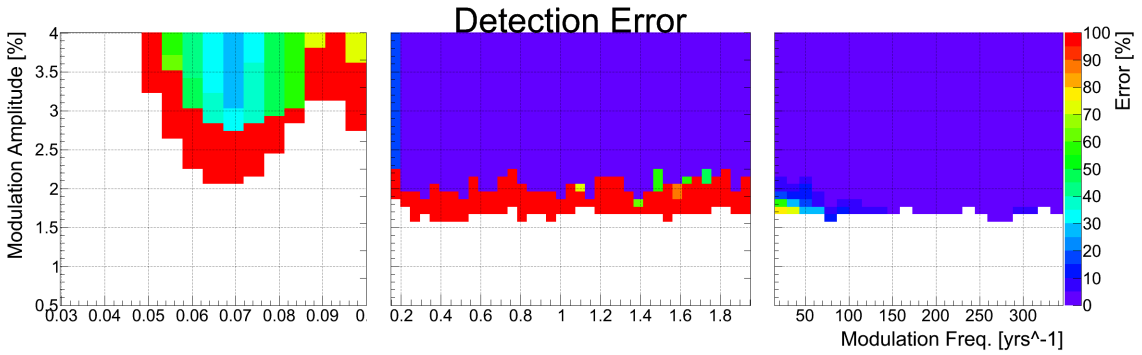

Figure 5.9: An illustration of how the relative detection error, for the LS technique, changes as the input modulation parameters A and f are varied (for three different frequency regimes - low, mid, and high) in the case where the largest periodogram peaks averaged C.L. values at or above 90%. The Z-axis, color, at each point denotes the relative error between the detected and true modulation frequencies.

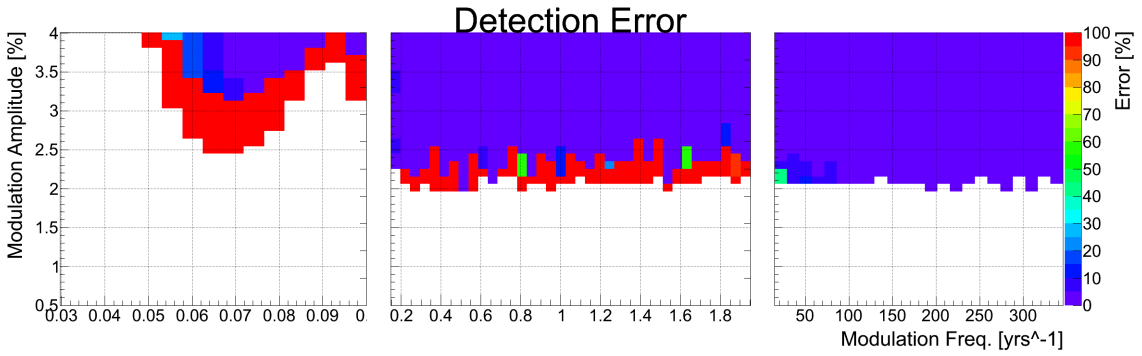

Figure 5.10: An illustration of how the relative detection error, for the GLS technique, changes as the input modulation parameters A and f are varied (for three different frequency regimes - low, mid, and high) in the case where the largest periodogram peaks averaged C.L. values at or above 90%. The Z-axis, color, at each point denotes the relative error between the detected and true modulation frequencies.

low frequency (long period) signals however, it is possible that the phase becomes an important parameter in the detection of a modulation. For this reason, the sensitivity studies were repeated for different phase values but only in the low frequency regime (though it was verified that non-zero phase values do not affect the mid frequency regime at all).

Since this new modulation form introduces a third parameter into the parameter space, the resultant sensitivity plots would have to be altered which would inhibit direct comparisons with previous results. For this reason, only four different (non-zero) phases ($\phi = \pi/4,\ \pi/2,\ 3\pi/4,\ \text{and}\ \pi$) were tested in the low frequency regime. This allows for direct comparison of the zero phase sensitivity plot alongside the various non-zero phase plots. The results are shown in figures 5.11 and 5.12 for the LS and GLS technique respectively.

These plots illustrate that the modulation phase value shifts the sensitivty contours in the low frequency regime so that at a particular frequency, one phase value may significantly aid in the detection of a modulation while a different phase value may inhibit detection. Consider, for example, a modulation with $f = 0.09\,\text{yrs}^{-1}$ which can only be detected at amplitudes greater than or equal to about 3.1% (using the LS technique) if $\phi = 0$. If instead $\phi = \pi$, the sensitivty to detection at the same frequency increases significantly, down to a modulation amplitude of about 1.7%.

Regardless of the shifts in the sensitivity contours as the modulation phase is varied, the low frequency regime also reveals a general cut-off value for the modulation frequency at which the detection sensitivity seems to be strongly suppressed. This is most apparent for the LS technique where detection seems very unlikely, if not impossible, for modulation frequencies below about $0.04\,\text{yrs}^{-1}$ (periods greater than 25 years). The GLS technique however does appear to still show some sensitivity at

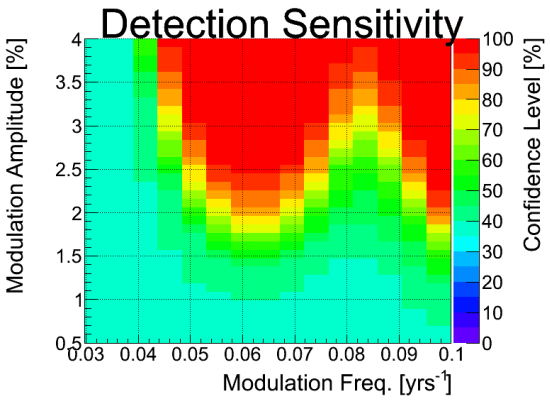

(a) $\phi = \pi/4$

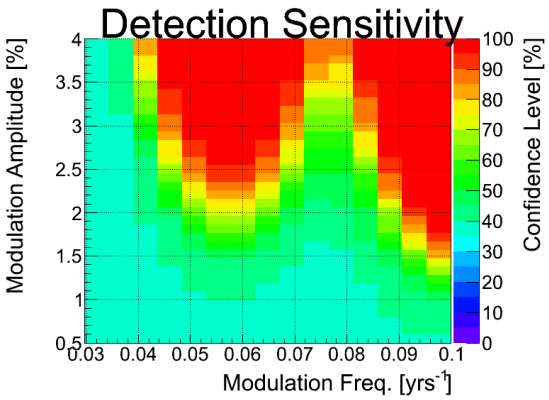

(b) $\phi = \pi/2$

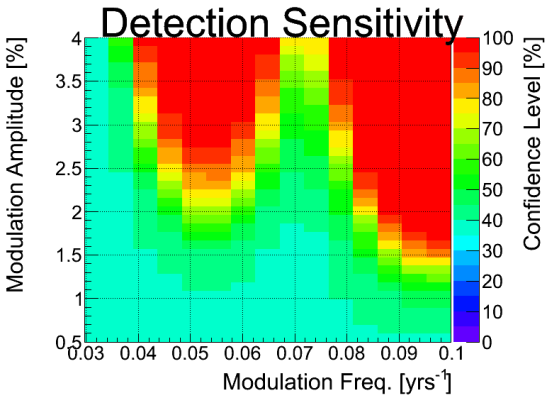

(c) $\phi = 3\pi/4$

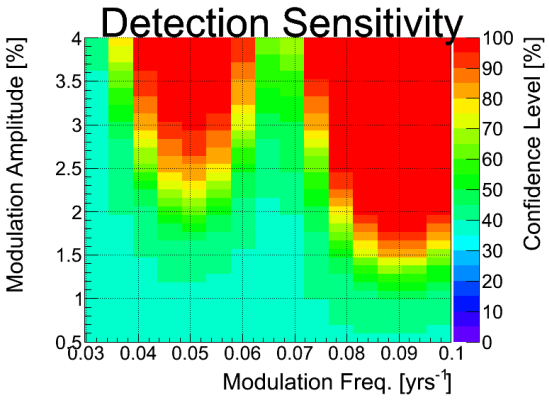

(d) $\phi = \pi$

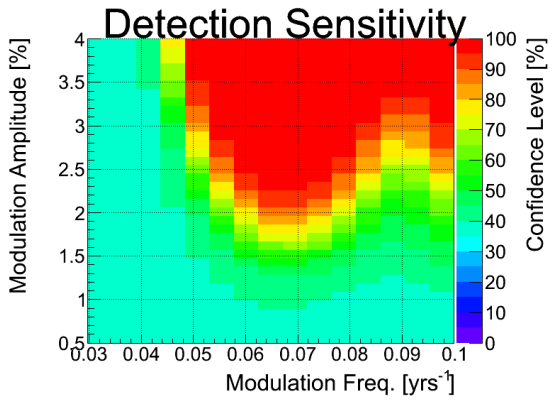

(e) $\phi = 0$

Figure 5.11: An illustration of how the modulation phase can shift the LS sensitivity contour in the low frequency regimes.

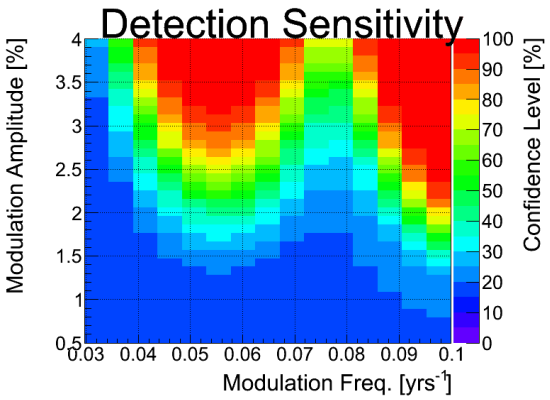

(a) $\phi = \pi/4$

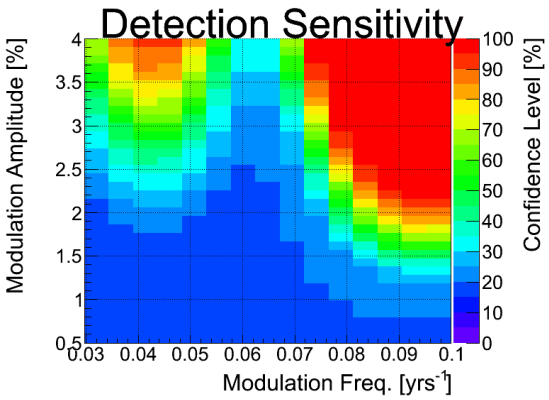

(b) $\phi = \pi/2$

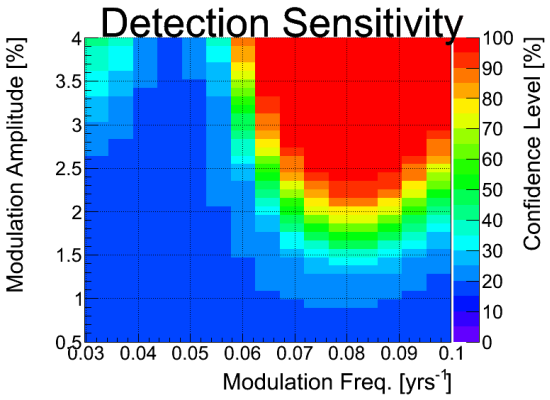

(c) $\phi = 3\pi/4$

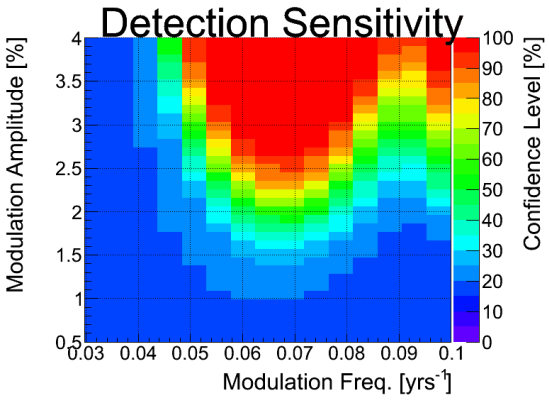

(d) $\phi = \pi$

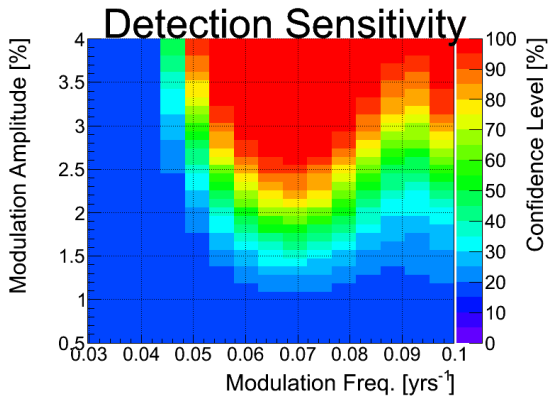

(e) $\phi = 0$

Figure 5.12: An illustration of how the modulation phase can shift the GLS sensitivity contour in the low frequency regimes.

or below this value but at significantly higher modulation amplitudes and only for specific modulation phase values.

Systematic Effects

Although the NEMO-3 MC and the entirety of the analysis procedure used to select events and build the $\beta\beta$ decay rate time series were designed to take into account all possible detector effect there are nonetheless uncertainties that remain regarding the performance of the detector and analysis tools. This section will explain the sources of these uncertainties and try to quantify their effects by once again using the sensitivity studies as a basis for analysis.

In standard NEMO-3 analyses which measure the $2\nu\beta\beta$ decay and search for the $0\nu\beta\beta$ decay of a particular isotope it has been well documented that the largest source of uncertainty is still due to the acceptance and efficiency of the detector in selecting events. This was observed and quantified during special runs in which sources of ^{207}Bi were inserted into the detector for calibration purposes. These sources are often used as "standard candles" for absolute energy calibration since they emit two characteristic conversion electrons at well defined energies of 482 keV and 976 keV. In addition to their use in energy calibrations, ^{207}Bi can also undergo a double conversion process (0.2%) and these coincident electrons can be used to study the response of the detector to two electron topologies.

The activities of these sources were first measured, to very high precision, using high-purity germanium (HPGe) detectors. Once inserted into the detector, these same sources also had their activities re-measured using the NEMO-3 detector. The events which were recorded in these runs were analyzed in an identical manner to the two electron event selection analysis presented in the previous chapter. A difference

of 5.5% was noted in the activities measured by the HPGe detectors and the NEMO-3 detector [85] which is taken as an uncertainty in the two electron event selection efficiency which is used to scale the data.

The other primary systematic considered in this analysis is the number of background events that enter into the rate calculation for the $\beta\beta$ decay of ^{100}Mo . As previously mentioned, recent analyses which measured the $2\nu\beta\beta$ half-life of ^{100}Mo found a signal over background ratio of 76. Suppose this ratio is taken to be true for all P2 runs individually. Then for each run i with S_i as the number of signal events, B_i as the number of background events, and $T_i = S_i + B_i$ as the total number of selected events, the percentage of background events expected in the run is given by

$$\text{Percent Background} = 100 \times \frac{B_i}{T_i} = 100 \times \frac{B_i}{S_i + B_i} = 100 \times \frac{1}{S_i/B_i + 1}. \qquad (5.2.4)$$

Using the approximation that S_i/B_i is constant and equal to 76 this gives the percentage of background events in each run to be equal to approximately 1.3%. This value is taken as a systematic uncertainty on the calculated rate for each run.

These systematic uncertainties can be applied when the scaled decay rate values are being calculated on the basis of the run efficiency and raw rate values. This is done via the introduction of a Gaussian smearing term

$$X_{\text{syst}} = X(1 + g\sigma) \qquad (5.2.5)$$

where X is the variable which is being smeared, g is randomly generated from a Gaussian distribution of zero mean and unitary width, and σ is the size of the systematic uncertainty being applied. Thus in the case of the uncertainty in the two electron selection efficiency, $X = \epsilon_i$ and $\sigma = 0.055$.

After each smearing has been applied, the distribution of the scaled rate values is produced and the new values of the mean and sigma are taken to generate a new

set of MC times series corresponding to the application of the particular systematic uncertainty. These new MC data sets are then used to calculate new sensitivity contours to determine how they shift as a result of the systematic effects. Those which correspond to the systematic uncertainties in the selection efficiency are shown in figures 5.13 and 5.14 for the LS and GLS techniques respectively. Those which correspond to the systematic uncertainty in the number of selected signal events are shown in figures 5.15 and 5.16 for the LS and GLS technique respectively.

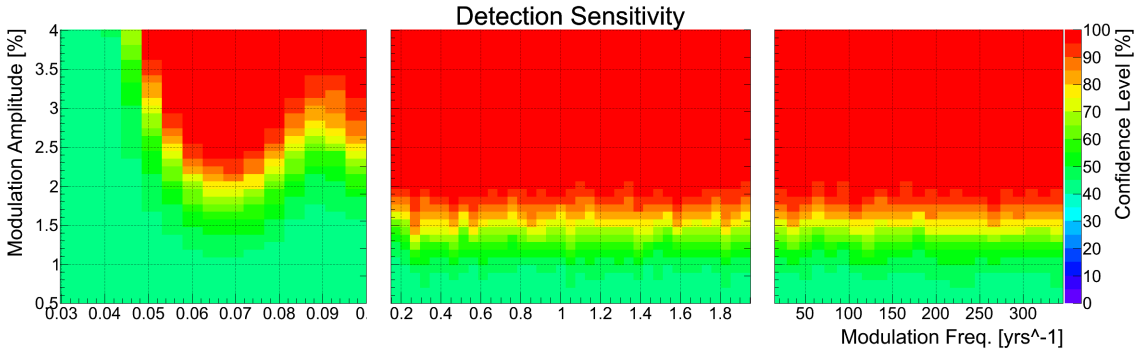

Figure 5.13: An illustration of how the LS detection sensitivity contour changes when the selection efficiency values are smeared by a 5.55% systematic uncertainty and the MC data sets are re-generated.

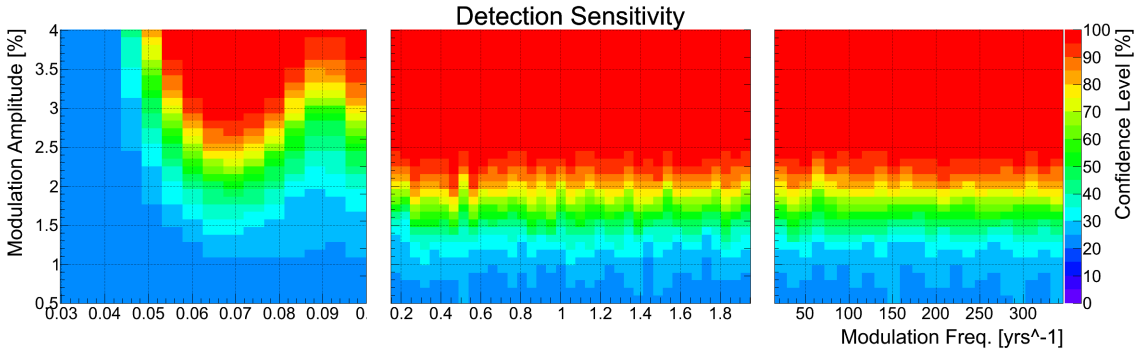

Figure 5.14: An illustration of how the GLS detection sensitivity contour changes when the selection efficiency values are smeared by a 5.55% systematic uncertainty and the MC data sets are re-generated.

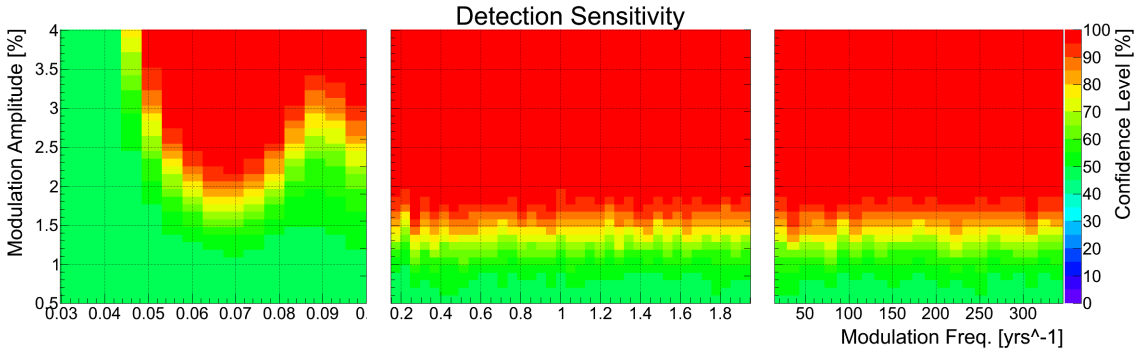

Figure 5.15: An illustration of how the LS detection sensitivity contour changes when the number of selected events per run are smeared by a 1.3% systematic uncertainty and the MC data sets are re-generated.

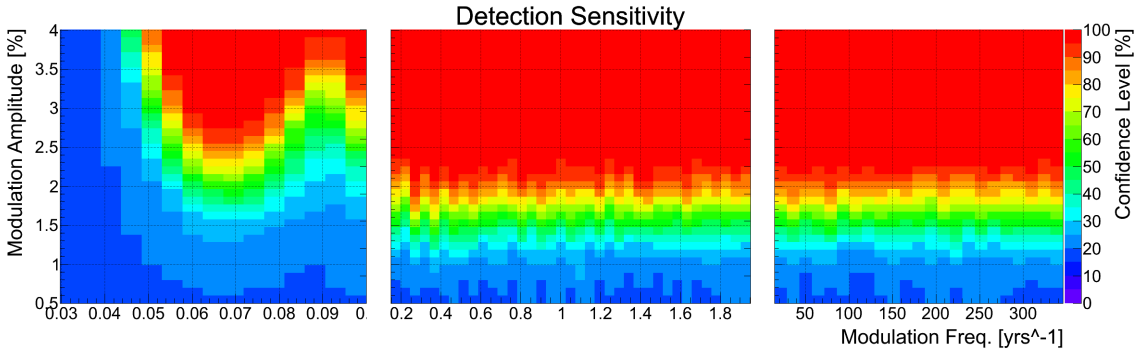

Figure 5.16: An illustration of how the GLS detection sensitivity contour changes when the number of selected events per run are smeared by a 1.3% systematic uncertainty and the MC data sets are re-generated.

These contours can be compared with those generated from MC data with no systematic smearing effects applied. In those results, the threshold amplitude established for detection at or above the 90% C.L. (in the mid and high range regimes) was determined to be about 1.7% and 2.1% for the LS and GLS techniques respectively. After applying efficiency systematic uncertainties these values shift to be about 1.75% and 2.2% for the LS and GLS techniques respectively. The systematic uncertainty due to the number of potential background events being selected in each run, however, resulted in imperceptible changes in the sensitivity contours relative to the modulation

amplitudes that were probed (which were spaced at 0.05% increments).

Chapter Six: The SuperNEMO Detector

6.1 Detector Description

The SuperNEMO Detector is a next generation neutrinoless double-beta decay detector and successor to NEMO-3. It will share the same design philosophy as its predecessor and employ the proven technique of combining tracking and calorimetric detector volumes around thin foils made of candidate $\beta\beta$ isotopes. One of the primary ways of pushing the limits on neutrinoless double-beta decay half-lives is by increasing the total observed isotope mass. To do this, SuperNEMO will unfurl the toroidal geometry of NEMO-3 into a planar design and multiply the number of full detector modules in order to observe 100 kg of $\beta\beta$ isotopes. In addition to the increased mass, improvements in every aspect of the detector performance will drive the sensitivity of SuperNEMO to measuring $0\nu\beta\beta$ half-lives on the order of 10^{26} years. After many years of intense research and development, the first SuperNEMO detector module, known as the Demonstrator, is under construction in the LSM lab that housed the NEMO-3 detector and is projected to begin taking data in early 2017.

In the next section a broad detector description will be presented highlighting the main differences and similarities to NEMO-3. The three sections that follow will then delve into the main components the detector: the source foils, the tracking volume, and the calorimeter. Afterwards, improvements in the radiopurity and background suppression will be discussed (the latter of which involves the anti-radon facility and detector shielding). In the final section, a summary of all the improvements in SuperNEMO relative to NEMO-3 will be given and projected to the increase in

sensitivity of the detector.

6.2 General Design and the SuperNEMO Demonstrator

While NEMO-3 observed about 10 kg of source material contained in a toroidal detector, SuperNEMO will need to accommodate ten times as much $\beta\beta$ source material without compromising the foil surface density. Since any increase in foil thickness would alter the intrinsic energy spectra of the $\beta\beta$ decay, the foil must increase in area instead. Rather than making a larger detector, SuperNEMO will instead "un-roll" the NEMO-3 geometry into a planar form and multiply the total number of detector modules. This allows for 100 kg of source material to be divided into 20 independent detector modules housing 5 kg each. Aside from providing a straight forward approach to increasing the mass of observed $\beta\beta$ isotopes, this gives SuperNEMO added flexibility in allowing data collection to begin as soon as each module is ready. As future modules are built, they can also take advantage of improvements in various technologies such as source enrichment, scintillator production, PMT performance, etc.

Each SuperNEMO module will be approximately 4 m high, 6 m long, and 2 m in depth and follow the NEMO-3 design principle of sandwiching a source foil frame in between tracking and calorimetry volumes and then wrapping the detector in a magnetic coil as well as passive shielding elements (as shown in figure 6.1). The Demonstrator will be the first such detector module and is designed to reach the level of sensitivity of NEMO-3 within just two years of run time. In order to achieve this, the Demonstrator will have slightly more source material with a total of 7 kg.

Just as in NEMO-3, this isotopic source will be formed into thin foil strips that will be vertically hung on a support frame structure. The primary $\beta\beta$ isotope in SuperNEMO will be ^{82}Se , chosen due to its enrichment feasibility as well as its sufficiently large $Q_{\beta\beta}$ (2995 keV) value. In addition, the modularity of SuperNEMO allows for successive module to house other interesting sources such as ^{150}Nd and ^{48}Ca if significant breakthroughs occur in their enrichment processes.

The tracking volume of a SuperNEMO detector module will contain 2034 open octagonal drift wire cells once again operating in Geiger mode. The gas mixture that fills this volume will be similar to what was employed in NEMO-3 with helium being the primary working medium, ethyl alcohol as the quenching medium, and argon and water vapor to stabilize cell performance and help with aging effects. There will be 18 total layers of tracking cells, nine layers on either side of the foil. The distance between the foil and the calorimeter wall will be about 50 cm on each side.

The calorimeter main walls, those which directly face the source foil, will be made up of 520 optical modules (OMs) which again are composed of plastic scintilltor blocks coupled to low radioactivity PMTs. Just as with NEMO-3, there are also additional OMs that cover the remaining top/bottom (known as the veto wall or v-wall) and side edges (known as the x-wall) of the detector. There will be 128 v-wall OMs and 64 x-wall OMs bringing the total number of SuperNEMO calorimeter OMs to 712.

The final elements of a SuperNEMO detector module consist of the same types of shielding elements used in NEMO-3. The first of these is a large solenoidal coil surrounding the detector to once again produce a 25 Gauss magnetic field within the tracking volume for particle discrimination and background rejection. This is then enclosed by various layers of passive shielding elements to reduce the influence of external radiation on the detector. The location of the Demonstrator in the LSM

facility (the same location as the NEMO-3 detector) once again ensures that the cosmic ray flux around the detector environment is very low.

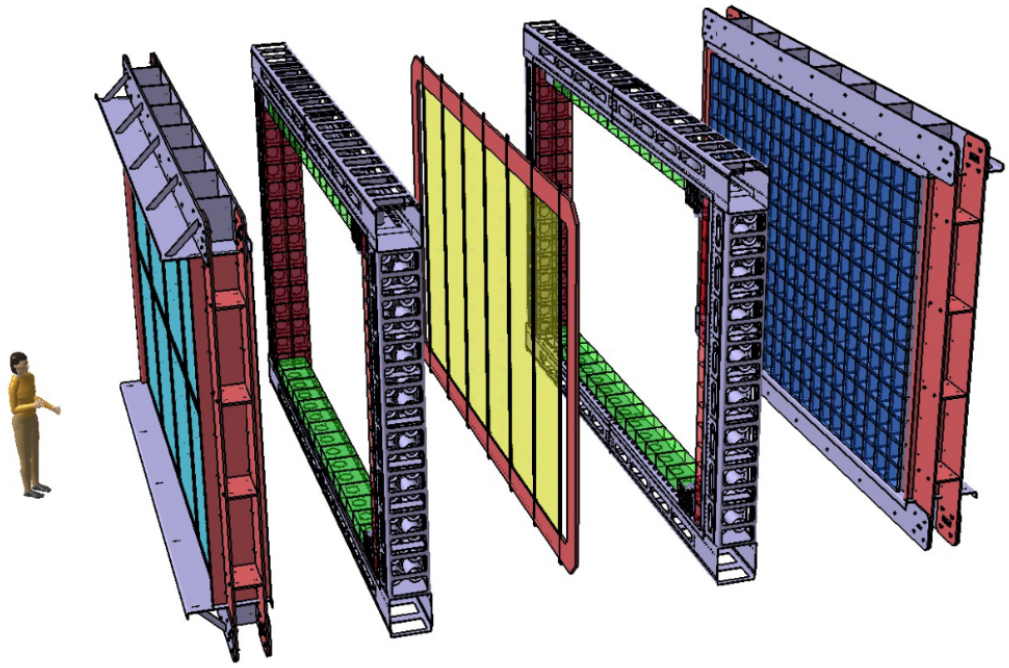

Figure 6.1: An exploded illustration of the SuperNEMO Demonstrator showing the central source frame surrounded on either side by tracking and calorimeter volumes.

6.3 The Source Foils

The SuperNEMO source frame is approximately 3 m high and 5 m wide but the total coverage of source material is closer to 2.7 m by 4.9 m. In order to contain 5 kg of $\beta\beta$ material (7 kg in the Demonstrator) in this area, the foil density must be 40 mg/cm^2 (53 mg/cm^2). The foil is divided into 36 strips which measure 2.7 m long and 135.5 mm wide (125 mm if the strip is located on the outer edge of the frame). Gaps between certain foil strips will allow radioactive sources to be lowered into the detector via wires attached to a plumb bob (discussed in a later section). An illustration of the

SuperNEMO source frame is shown in figure 6.2.

A main focus of the R&D efforts surrounding the source foils has been directed towards the reduction of internal radioactive impurities. The most detrimental contaminations for SuperNEMO come from the isotopes ^{208}Tl and ^{214}Bi which have decay energies near the signal region for $0\nu\beta\beta$ decays. One of the constraints required for SuperNEMO to reach its target sensitivity is that the activity of these contaminants must be limited to less than 2 μBq/kg for ^{208}Tl and less than 10 μBq/kg for ^{214}Bi . In order to verify that each foil strip meets this criteria, a special detector, known as the BiPo detector [86], was designed to search for signature decays as ^{214}Bi and ^{212}Bi decay to ^{214}Po and ^{212}Po via by a beta emission followed very shortly thereafter by a delayed alpha decay (with half-lives of 164 μs and 300 ns respectively). The detection of the electron plus delayed alpha gives a very pure channel to measure the background contamination levels in SuperNEMO source foils.

As was the case for composite foils in NEMO-3, the source foils will be made by taking enriched ^{82}Se powder and mixing with an organic glue to create a paste. This paste will then be applied on or around a support material and be allowed to cure. Since the radioactive contaminations mentioned above can be found in any of the components used to make the foil strips, a lot of effort has gone into screening the materials used and redesigning the foil strip construction technique to eliminate as much background contamination as possible. The two candidate foil strip construction techniques are described in the next section.

Foil Design Techniques

Two different groups are currently developing techniques to create source foil strips for SuperNEMO with the desired physical specifications and low background require-

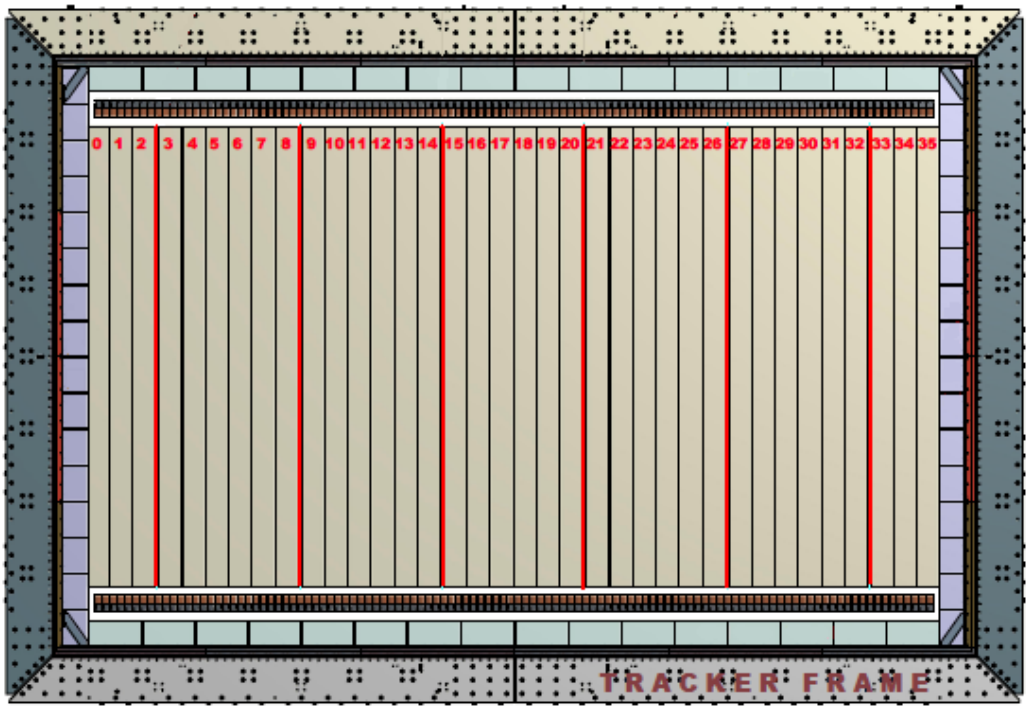

Figure 6.2: An illustration of a SuperNEMO source frame showing the division of the foil into 36 strips. The six vertical red lines denote where a gap exists for the introduction of radioactive calibration sources which will be lowered into the detector via wires attached to plumb bobs.

ments. The first of these groups is from ITEP in Moscow, Russia (who were involved in the production of NEMO-3 source foil strips) while the second is from the Laboratoire d'Annecy-le-Vieux de Physique des Particules (LAPP) in Annecy-le-Vieux, France. Both foil production techniques begin in a similar fashion with enriched and purified ^{82}Se powder being mixed with an organic glue to create a paste. This glue is made of polyvinyl alcohol (PVA) mixed with distilled water and has been measured to be very radiopure. The main difference between the two foil production techniques then comes in how this paste, known as source paste from here for the sake of brevity, is turned into thin foil strips.

The ITEP foil production method continues to apply the proven technique established in NEMO-3. This means that the ^{82}Se and PVA paste is loaded into a syringe

and uniformly applied into a Mylar backing film. Just as in NEMO-3, this backing film is created by irradiating a 12 μm Mylar sheet with an ion beam to create microscopic holes that allow the paste to cure. Once the paste has been spread onto the backing film, another film is applied on top to sandwich the paste giving it tensile strength while allowing it to remain flexible.

Although Mylar as a material is generally very radio-pure, it is suspected that the process of converting raw Mylar films into backing films via ion beam irradiation introduces significant amounts of unwanted radioactive contaminants. This lead the LAPP group to search for a foil strip production methods that avoid the use of an ITEP-style backing film. The first such attempt was based around trying to embed within the source paste a mesh or netting known as Swisstulle [87]. This fabric is made of nylon6-6 yarn woven into a hexagonal mesh of thickness 0.08 mm and density of 0.7 mg/cm^2. The idea was that this mesh would act as a skeletal frame onto which the paste would cure. The mesh would then provide the necessary strength and rigidity for mounting the strips while minimally interfering with the emitted $\beta\beta$ electrons and with minimal additional mass of possible contaminations. Concerns about exposure of the cured source paste to the tracker gas mixture then lead to the development of a second technique in which the source paste was spread over a Tedlar® surface and allowed to cure into a full size foil strip of the desired density. The foil strip is then peeled free and cut into pads which are placed into pockets created by soldering together two long, narrow (just wider than the pad width) strips of raw Mylar. In total nine pads are combined to create a full source foils strips. This method adds a slight amount of dead space into the foil strips (due to the soldering of the Mylar to make pockets) which necessitates an increase in the foil density but the overall change is less than 5% and has been shown to be negligible.

6.4 The Tracking Volume

The SuperNEMO tracking volume will use open octagonal drift cells which are very similar to those employed in NEMO-3 with the primary difference being a 10% increase in overall cell length. Each cell consists of a central anode wire surrounded by 8-12 ground wires (depending on the number of adjacent cells which may necessitate additional grounding wires to reduce cell cross talk) with cathode pickup rings at each end. Optimization of the cell dimensions, materials, layout, and operation properties has lead to near 100% plasma propagation efficiency and resolutions of 0.7 mm radially and 1 cm vertically. Due to the large number of total wires needed to create the full SuperNEMO tracking volume, a major focus of the tracker R&D was to automate the cell production process to reduce the risk of contamination. To this end, a wiring robot was commissioned which can create tracker cells within a clean room environment.

6.5 The Calorimeter

The SuperNEMO calorimeter is once again composed of a grid-like structure of OMs, made of a PMTs coupled to a plastic scintillator blocks, which surrounds the tracking volume and source foil frame. Since the energy resolution of these OMs plays a large role in the detector's sensitivity to $0\nu\beta\beta$ decays, a major focus of the R&D efforts revolved around improving this parameter. A factor of two improvement in energy resolution was achieved by optimizing the individual OM components (PMT and scintillator) as well as improving how these elements are combined.

SuperNEMO scintillator blocks share a similar composition with NEMO-3 blocks and use polystyrene (PS) as a base material with dopings of PTP and POPOP to

act as the scintillating agent and wavelength shifter respectively. The overall size of each block is considerably larger than any of the NEMO-3 style blocks and the full dimensions are $256 \times 256 \times 194$ mm. These blocks are coupled directly to 8-inch Hamamatsu R5912-MOD PMTs with 8 dynode stages which were chosen for their high quantum efficiency (41% at 00 nm) and low radioactivity. A hemispherical recess, about 5 cm deep, is machined into each scintillator block so that the entirety of the PMT photocathode can make full contact with the block surface when it is glued in place using RTV. The lack of a light guide to interface the PMT and scintillator block is a large contributor to the improvements in light collection, and thus energy resolution, of the SuperNEMO design. Just as in NEMO-3, each block is also wrapped with a layer of thin aluminized Mylar on all surfaces and three layers of Teflon tape around the sides to aid in light collection at the PMT photocathode. Finally, a shield made of pure iron surrounds each OM to provide structural support for the calorimeter walls and to shield the blocks from the magnetic field in which the detector is immersed. An illustration of a typical SuperNEMO main wall OM is shown in figure 6.3. Note that the small step at the entrance face of the block ensures that there are no gaps in scintillator coverage when OMs are placed adjacent to one another (the step essentially leaves room for the iron shields to enclose each OM). This step structure steps is 3 cm which is sufficient to fully absorb electrons up to 3 MeV. The reason for the full depth of the scintillator being nearly twice the 10 cm requirement in NEMO-3 (for efficient γ-ray tagging) is that the larger photocathode radius requires increased distance between the front face of the PMT and the end of the iron shield.

GEANT-4 based optical simulations were used to guide all of the material choices and the optimal wrapping and coupling methods so that an energy resolution of

$(8 \pm 1)\%$ FWHM is achieved for 1 MeV electrons in an average OM (this translates to a resolution of 4% FWHM at 3 MeV which is near the $Q_{\beta\beta}$ value for ^{82}Se). The time resolution of the blocks was also measured and found to be 400 ± 90 ps for 1 MeV electrons. Even with the larger block size, the spatial uniformity (in terms of the impact point of an electron on the block face) was found to be better than 95% for for nearly all produced OMs thus far.

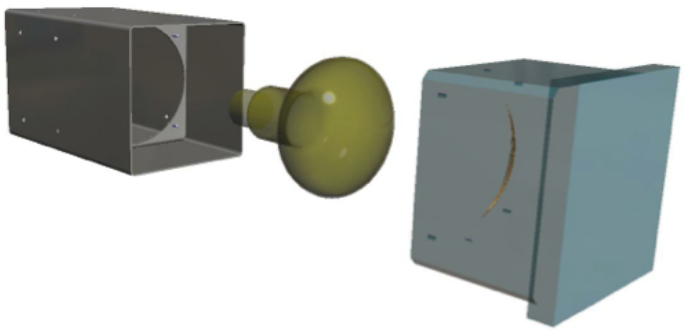

Figure 6.3: An illustration of a SuperNEMO main wall optical module (OM) made of an 8-inch Hamamatsu R5912-MOD PMT coupled to a $256 \times 256 \times 194$ mm polystyrene scintillator block via an RTV. A pure iron shield surrounds each OM for structural support and magnetic field shielding.

Calibrations

A two-fold calibration process will be used for the SuperNEMO detector using two independent systems: The Radioactive Source Deployment system and the Light Injection Monitoring (LI) system. Just as with NEMO-3, the former will be used for direct calibrations of energy and timing properties on a monthly basis while the latter will be used to monitor the day-to-day response of the detector between absolute calibrations.

The SuperNEMO source foil frame has gaps in between foil strips numbered 2 and 3, 8 and 9, 14 and 15, 20 and 21, 26 and 27, and 32 and 33 (see figure 6.2 again for the strip numbering scheme) so that radioactive calibration sources of ^{207}Bi and ^{90}Sr can be lowered into the detector for absolute energy calibrations. A total of 18 sources, three for each of the six inter-foil gaps, will be present during any given calibration run. The sources will be secured to a loop of wire attached to a very pure copper plumb bob. When this weight is lowered into the detector via guiding wires it will come to rest at a position near the bottom of the detector such that the three sources are spaced uniformly along the vertical axis of the source foil frame. This even spacing between the three sources on a single loop as well as between succesive loops places the sources in optimal positions for uniformly illuminating the main calorimeter walls. Since this method avoids the need for the calibration tubes and windows of NEMO-3 a significant reduction in radioactive contamination is achieved. Furhtermore, the entire process of introducing and removing the radioactive sources has been automated with the use of stepper motors that control various valves and wheels. This greatly reduces the risk of outside contamination and also means that the process of calibration is less intrusive and time consuming.

The LI system takes up the role of the laser survey system used in NEMO-3 and injects UV light into each OM via fiber optical cables to monitor the response of the calorimeter to within 1% and to periodically perform linearity tests with higher light levels. Rather than using UV lasers as the source of light, which were found to be too unstable for the precision required in SuperNEMO, SuperNEMO will instead use UV light emitting diodes (LEDs). This necessitated a large amount of R&D and testing to ensure the the system can meet all the goals desired for monitoring the detector. The development and testing of the LI system is a large part of the work covered in

this thesis and is described in full detail in the next chapter.

6.6 Radiopurity

When searching for a process as rare as $0\nu\beta\beta$ decay, even the smallest of radioactive contaminations become hugely important. A major focus of the SuperNEMO R&D thus focused on reducing the level of background contaminations by an order of magnitude or more. An aggressive screening program has thus been employed to select only the most radiopure materials for use in the detector. A number of high purity germanium (HPGe) detectors have been used to measure the activity of (or set limits on) most detector components and a radiopurity budget has been established based on the mass of each component to keep the overall levels of ^{208}Tl and ^{214}Bi below the desired thresholds.

In addition to radioactive contaminations in the source foils and in detector componenets themselves, a major background for NEMO-3 was due to the presence of radon in the detector which is a highly diffusive gas whose progenies, including the pernicious ^{214}Bi , can deposit themselves on the tracker wires or the surface of the foils. The radon itself can orignate from emanation, contamination, or diffusion and SuperNEMO has invested significant R&D efforts to tackle all sources of radon. The ultra low levels of radon required for SuperNEMO necessitated the development of new radon emanation chambers and a new radon concentration line with sensitivities to much smaller concentrations of radon. These systems have also beeun used to study various seals and glues in order to choose those which offer the least permeability to radon gas.

6.7 Performance

Each of the improvements to individual detector components have all added up to significantly increase the sensitivity of SuperNEMO in searching for $0\nu\beta\beta$ decay. An overview of the results of the full R&D program is presented in table 6.1 along with the projected sensitivtiy on the $0\nu\beta\beta$ half life and the corresponding effective neutrino mass.

Detector Parameter	**NEMO-3**	**SuperNEMO**
Isotope	^{100}Mo , ^{82}Se , ^{130}Te ...	^{82}Se
Mass	10 kg	100 kg
Energy Resolution	14-17% @ 1 MeV	8% @ 1 MeV
^{214}Bi in foils	300 µBq/kg	10 µBq/kg
^{208}Tl in foils	20 µBq/kg	2 µBq/kg
^{222}Rn in tracker	5 mBq/m^3	0.15 mBq/m^3
$T^{0\nu}_{1/2}$ Sensitivity	10^{24} yr	10^{26} yr
$\langle m_{\beta\beta} \rangle$ Sensitivity	$0.3 - 0.7$ eV	$0.05 - 0.1$ eV

Table 6.1: Summary of NEMO-3 and SuperNEMO detector parameters.

The SuperNEMO Demonstrator is under construction in the LSM laboratory at this time. As of this writing, two out of four of the tracker sections and one main wall of the calorimeter have been transported to and installed in the lab. The projected start date for data taking is in early 2017.

Chapter Seven: The Light Injection Monitoring System

7.1 Introduction

The Light Injection (LI) Monitoring System has been designed to serve a similar role for SuperNEMO as the Laser Calibration System did for NEMO-3. It will work in tandem with the Source Deployment System to monitor the day-to-day behavior of each individual calorimeter channel. The primary goal of the system is to provide sub-1% precision in tracking the response of SuperNEMO calorimeter optical modules (OMs) but, as in NEMO-3, the system will also be periodically used to test the linearity of OMs up to higher energies than achievable with the radioactive calibration sources alone. Although much of the R&D for the system has been finished, some details or specific dimensions have yet to be finalized. These are noted in the text and estimations are provided when possible.

The first section of this chapter will describe the design and goals of the system and its individual components. The next will explain the difficulties in and results of optimizing the optical performance of the system including the overall light transmission and uniformity across all channels. The following section discusses the results obtained when monitoring a test calorimeter OM using a test bench setup at the University of Texas at Austin. Lastly, details are given regarding the remaining R&D required before the final implementation of the system.

7.2 Design Principles

The LI System has been designed to inject UV wavelength light from light-emitting diodes (LEDs) into each of the main-, x-, and v-wall OMs employed in SuperNEMO. The heart of the system is housed in a custom made light-tight electronics rack with dimensions 56.83 cm wide by 82.30 cm deep by 233.68 cm high (a model of which is shown in figure 7.1). This rack is divided into three equal vertical sections by internal shelving. The central section will house the main LED driving unit known as the "pulser box". The front panel of this pulser box will remain visible to display the status of the system (via LED indicators) and to give access to the pulser box power switch, the serial port for PC-to-pulser box communications, and the BNC output trigger of the pulser box. The sections above and below this will house the various reference OMs used for calibration and monitoring of the LED outputs. These sections will contain doors to allow access to the reference OMs in the event of maintenance needs or the addition/replacement of components. Small patch panels will be installed above these doors to transmit the HV and signal cables required by the reference OMs. The back wall of the rack will consist of light-tight feedthroughs for the fiber bundles used to transport the UV LED light (produced in the pulser box) to each SuperNEMO OM.

The pulser box can support driving up to 20 LEDs in groups of 5, 10, or 15 pulsing at a time. Since each SuperNEMO module will have a total of 712 optical modules each with two calibration channels, a total of 1424 fiber optic lines will be needed between the LI system LEDs and the detector. In addition to this, 80 additional fiber optic channels are needed, four per LED, so that each LED can be monitored by each of the four reference OMs. This requires that each LED be coupled to a bundle of at least 76 individual fiber optic cables. In order to account for spares in

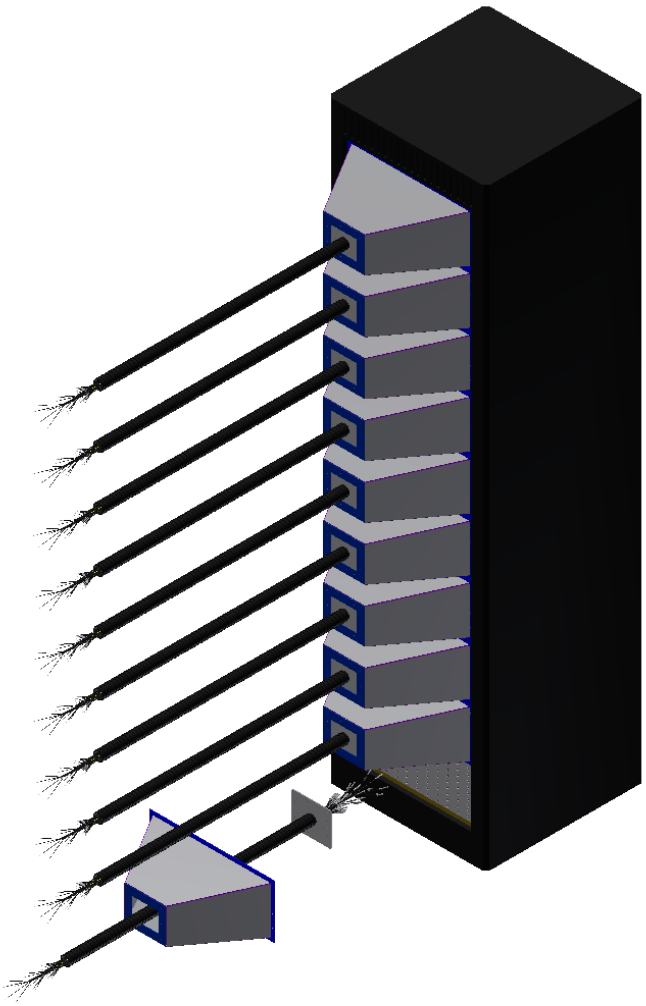

Figure 7.1: A computer generated drawing of the LI system rack that will house the main components. This three-quarter rear view shows where the fiber bundles will exit the rack to be brought into the detector. Many of the finer details including the doors, patch panel, and pulser box front panel were not included in this early design template.

case of damaged fibers, this number has been increased to 84 per bundle giving rise to a total of 1680 channels.

A basic schematic overview of the system is shown below in figure 7.2. The fiber bundles will be continuous from the LED until they reach the inside of the detector shielding elements at which point they will distributed to each OM. Individual fibers remain continuous until they reach the rear iron end cap of a given OM where specially developed radio-pure connectors transition the light from the long fibers into 50 cm long "pig-tail" pieces, glued into the OM scintillator blocks at the time of assembly, which inject the light into the OM. The fibers are shielded from physical harm as well as ambient light through the majority of their journey via corrugated plastic tubing. Special feedthroughs are used during the routing to ensure that all transitions between detector volumes are radon-tight.

As for the fibers that inject UV LED light into the reference OMs, these are made identically to the calorimeter OM fibers (i.e. they have the same length and also feature a short "pigtail" connected via an identical connector) so that the light levels detected are similar in magnitude. Since these fibers remain entirely within the LI rack though, the excess length is coiled up and no additional protection is required.

Goals and Constraints

As mentioned previously the LI system has two main goals:

1. Response Monitoring - The gain of a PMT can vary slightly with environmental conditions (such as temperature), fluctuations in applied high voltage, or age related effects. Similarly, scintillator properties, although more stable, can also vary over time. To monitor this behavior, UV LED light is injected via optical fiber to excite scintillation light and trigger a response in each OM similar to

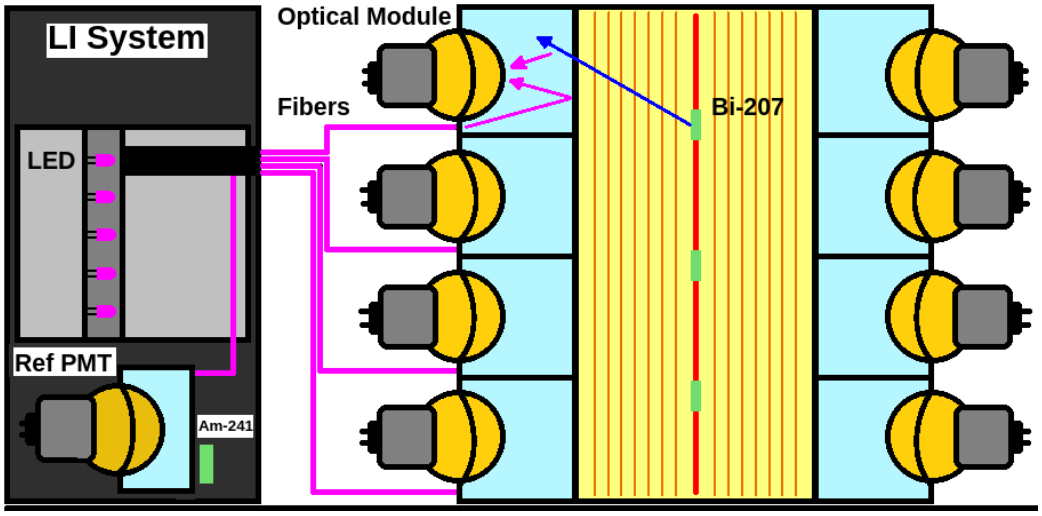

Figure 7.2: A schematic representation of the LI system. The pulser is shown driving the LEDs that then inject their light, via fibers, to individual SuperNEMO calorimeter optical modules. A monitor PMT shown with the LI system will track the LED light levels against a reference ^{241}Am source.

what would be expected from a real detector event. For each OM, this response is compared to a baseline value established with the most recent calibration run using the Source Deployment System. The LI system will do this on a daily basis to track deviations in the response of each OM at the 1% level.

2. Linearity Testing - Almost any PMT is subject to non-linearity effects when the incident light levels get too large, as could be the case when detecting high energy particles. While the Source Deployment System can use ^{207}Bi and ^{90}Sr to calibrate OMs up to 3 MeV, higher energies require higher light levels to be injected into each OM. To mimic these high energy events and note the start of non-linear effects, the LI system will be required to provide a tunable source of light extending to such higher light levels.

The above goals can be used to impose certain requirements on the light delivered to each OM. These constraints determine the basic challenges in designing and opti-

mizing the system. In order to achieve monitoring accuracy at the 1% level the light output of each UV LED must be known to at least the same level or better using a reference OM coupled to its own calibration source (which can be observed constantly since it is external to the detector). To stimulate the desired response range in the calorimeter OMs the UV LEDs have to produce enough light to compensate for losses due to non-uniform fiber bundle illumination, transmission along the fibers, and fiber-to-fiber connectors. Studies of SuperNEMO OMs have shown that 1 MeV electrons produce on the order of 1000 photo-electrons. This means that linearity test up to 5 MeV would require light levels of 5000 photo-electrons in each OM. Lastly, in order for each OM to be calibrated to roughly the same level, they must all receive roughly the same amount of LED light. The uniformity of the LI system should be such that the difference between light levels from one OM to another doesn't differs by more than a factor of two.

The LED Pulser Box

The LI system's pulser box drives and controls up to 20 UV LEDs in various group-pulse configurations. Originally developed for and used by the MINOS experiment [88] a few modifications have been made to the system to tailor it for use in monitoring SuperNEMO OMs. The physical box itself has been redesigned so that it is now a small part of the larger LI rack rather than being a purely self-contained system as in MINOS. In its original incarnation the pulser box was sealed to be light-tight and contained all of the electronics, LEDs, light distribution components, and fiber optics needed. The entire box could then be mounted into any standard electronics rack and the rear connector panel would permit fibers bundles to be coupled so extract the light for calibration and monitoring. In the SuperNEMO version of the system, the pulser

box was reduced to its primary essence consisting of the electronic circuitry, LEDs, and the light distribution components. The fiber bundles and reference OMs are then all integrated with the pulser box inside of the dedicated LI rack. The modified pulser box is now 14 inches high, 11 inches deep, and 19 inches wide. It is partitioned into two halves, front and rear, by a vertical wall near the midpoint of its depth. The front half of the pulser box contains the main electronic components and will have a front panel visible from outside the LI rack to for access to input and output triggering, PC serial communications, and the main power switch and LED status indicators. The rear half of the pulser box contains the light distribution elements which couple to the fiber bundles. This compartment will remain open so that the fiber bundles can transition outside the rack via light-tight ports (for routing to calorimeter OMs) while selected individual fibers can be routed to the reference OMs housed within the LI rack. The wall that divides the two pulser box compartments has 20 holes that line up with the LED slots in the circuit boards. The LEDs overhand the ends of their circuit boards and pass through these holes in the partition. The optical light distribution components then surround each LED and are mounted directly onto the partition. Figure 7.3 shows how the basic pulser box elements are coupled together with the partition (shown in blue).

The electronics contained within the front half of the pulser box consists of two LED driver circuit boards, capable of pulsing 10 LEDs each, and one controller circuit board onto which the driver boards are mounted. The controller board contains a PIC16F877 microprocessor [90] as well as a RS232 interface to communicate with a PC via simple ASCII commands. During standard operations, the PC can instruct the system to pulse a particular block of LEDs at a given pulse height, pulse width, and frequency. The microprocessor receives these commands and takes care of the

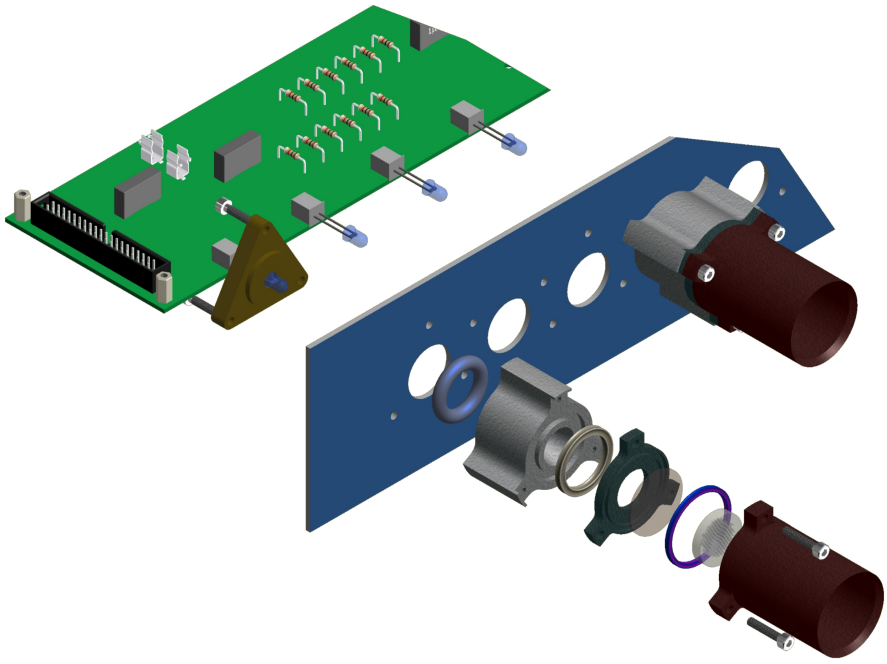

Figure 7.3: An illustration showing the basic components in the LI pulser box and how the are coupled.

actual pulsing of the driver boards.

The driver boards circuitry is shown in figure 7.4 and the manner by which pulses are generated is as follows. A voltage, which determine the pulse height, is supplied by a 10-bit DAC. When the signal at point A goes high, the driver is turned on so that voltage is delivered to the 22 Ω resistor and current is shunted to ground via the left-hand FET. When the signal at B goes low, current can pass thought the LED stimulating the emission of UV light. Some time later the signal at point C goes high which shunts the current to ground via the right-hand FET, thus turning of the LED. The pulse width, or amount of time the LED spends on, is thus determine by the difference in start times for the signals at B and C. This is delay is programmable to values between 15 and 36 ns in 3 ns increments. By varying both the pulse height and width a wide range of pulse sizes can be generated corresponding to a wide range of

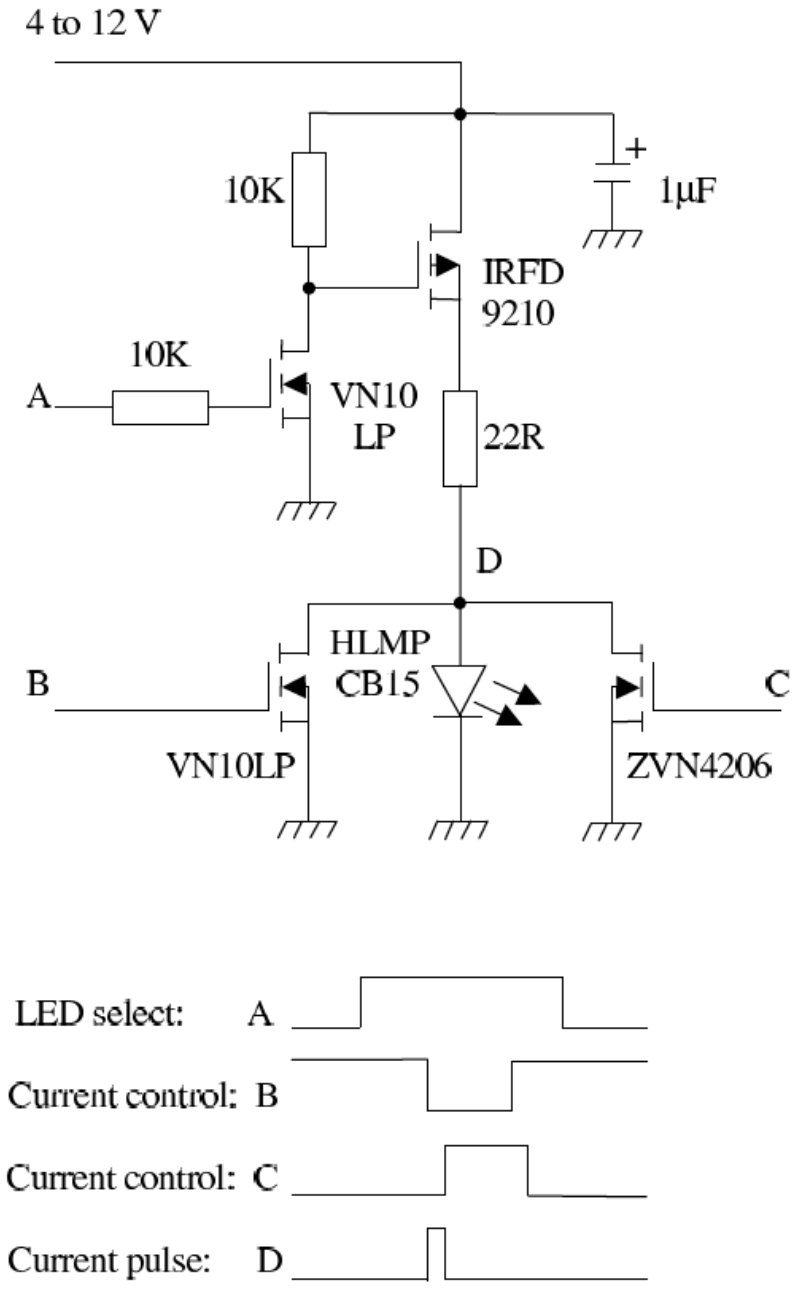

Figure 7.4: An illustration of the LED driver circuit showing the basics of operation.

LED intensities.

UV LEDs

In NEMO-3 the system used to monitor the calorimeter was based on the use of UV lasers instead of LEDs. Each light source has its own advantages and disadvantages in the context of OM monitoring. The advantages of lasers are two-fold:

- Laser intensities are generally much higher than those of LEDs.
- Laser pulses can be much faster than LEDs, thus producing scintillation spectra that better mimic the passage of charged particles.

The advantages of LEDs meanwhile are as follow:

- LEDs, being solid state devices, exhibit much better stability when compared to lasers.
- LEDs can operate at higher repetition rates to speed up data taking.
- LEDs, although less bright, can be tuned via software that adjust the current supply. A laser system requires a series of mechanically actuated filters to vary the intensity which further complicates the system.
- An LED based system does not require moving parts or other components that can wear and lead to more maintenance and shorter lifetimes.
- An LED based system is also cheaper than a corresponding laser based one.

Since the instability of the laser system used in NEMO-3 was known to limit its effectiveness, this was one of the primary motivations for switching to an LED

based monitor system for SuperNEMO. The LEDs used in the LI system are InGaN-based radial through-hole type LEDs, model VAOL-5GUV8T4, produced by Visual Communications Company (VCC) [91]. They have a central wavelength of 385 nm and a half intensity angle of 30 °. They were selected based on various criteria, one of the most important being how uniformly they illuminate our fiber bundles.

As mentioned previously, UV light is used in order to excite the scintillator in a manner similar to a charged particle. For this to happen, the LED output spectrum cannot overlap with the scintillation spectrum which starts at 400 nm. If even part of the LED spectrum overlaps into the scintillation range it can alter the spectrum seen by the PMT which affects its response. This is illustrated in figure 7.5 where a spectrometer was used to study the spectra of two different LEDs before and after passing their light through a small polystyrene scintillator block. On the left, the LED has a lower central wavelength and its spectrum (in blue) doesn't overlap with that of the scintillator (in magenta). Meanwhile, if a higher wavelength is used, corresponding to the plot on the right, the spectra overlap and the scintillation spectrum in particular is now clearly influence by the LED light that was transmitted directly through. The choice of wavelength was also balanced by the fact that as LED wavelengths went lower than 400 nm other properties, such as overall brightness or rise time, would suffer.

Fiber Optics Cables and Connector

To deliver the light emitted from the UV LEDs, a total of nearly 15 m of fiber optic cabling will be used. This cable will be unbroken until it reaches its target OM at which point a specially designed plastic connector will be used to couple the cable to a 50 cm piece (known as a "pig tail") which brings the light through the OM shielding

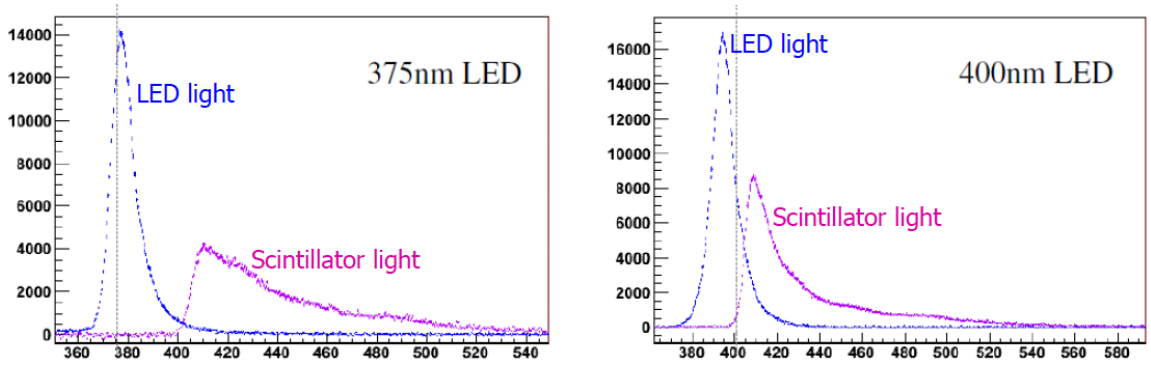

Figure 7.5: An illustration of the effects of the LED spectra on the scintillation response. The left plot shows a UV LED spectrum as well as the spectrum produced by a small scintillator block excited by the LED. The plot on the right shows the same spectra but made using a higher wavelength UV LED. In the latter case it is evident that some LED light is being transmitted through the scintillator thus altering its spectrum.

and injects it into the scintillator block. The fiber optic cable chosen is Eska brand fiber model SK40 [92] which is manufactured by Mitsubishi Rayon Corporation. It consists of a Polymethyl Methacrylate (PMMA) resin core surrounded by a flourinated polymer cladding. The core has a refractive index of 1.49 and diameter of 980 µm. The total diameter of the fiber is 1000 µm.

Once bundled, The fibers are fed through corrugated plastic tubing which protects them (both from external light and from physical harm) as they leave the LI rack and transition to the detector. A soft fabric-based sheath will also be used inside of the plastic tubing to help maintain the bundles in tightly packed formations.

In order to optically couple the long fiber cable to the pig tail piece, a special connector was needed to ensure minimal light losses as this interface. Commercial optical fiber connectors were found to be an issue from both a radiopurity and optical performance point of view. For this reason dedicated connectors were designed which could be molded out of radiopure acetyl co-polymer plastics (often used in other SuperNEMO components). These connectors, shown in figure 7.6, consisted of five parts:

- Two carrier pieces - each end of fiber optic cable to be coupled is glued into a carrier piece using epoxy. The fiber purposely extends beyond the carrier face so that the ensemble can then be fly-cut, after gluing, using a synthetic diamond tipped tool mounted to a high speed flywheel. The carriers are made sufficiently long to allow for partial cutting of the plastic material which ensures a completely smooth and flat face for the best light transmission.

- One bulkhead piece - this is the central piece that mounts onto the transition surface (i.e. the OM end cap). The opening on either end allows the carrier pieces to meet at the center and make good optical contact. The outer surface of the bulkhead is threaded to accept nuts that secure the carriers in place. The bulkhead also has four notches on either end to accept small teeth on each carrier. These prevent the carriers from rotating while the nuts are tightened so that the fiber faces are not scratched or damaged as they are pressed together.

- Two nuts - these have threading to match the outer surface of the bulkhead and when they are screwed in, their inner surface pushes the carriers together to ensure a good physical contact is maintained. Holes are drilled through their ends to allow passage of the fiber.

Light Distribution Components

The light cone is an aluminum cylinder with a longitudinal conical bore hole which is mounted into the pulser box dividing panel such that an LED sits at the apex of the bore hole opposite a fiber bundle attached at the other end. This piece serves three purposes: its inner surface helps to funnel and collimate the LED light towards the fiber bundle to aid in illumination uniformity and brightness, it allows for the

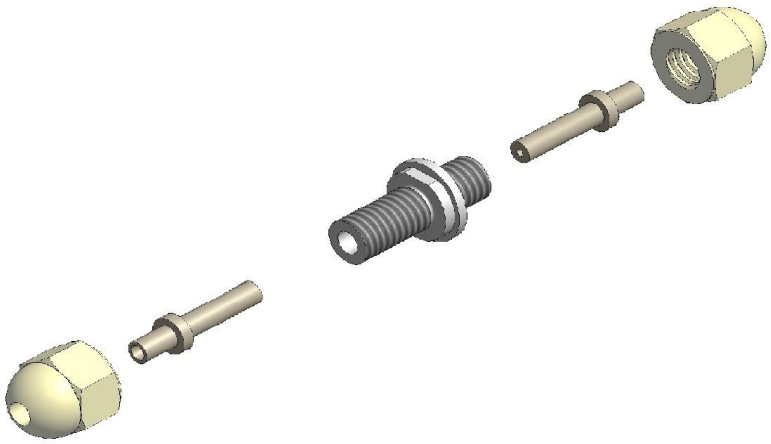

Figure 7.6: An illustration of the custom made fiber optic connectors for the LI system. The central bulkhead is shown receiving a fiber-fitted carrier in each end. The carriers have a special tooth that serve to lock it in place within the bulkhead and two nuts ensure good contact between fiber faces.

mounting of optical filters that may be needed between the LED and fibers, and it acts as the structural support into which the fiber bundles are mounted.

To create the fiber bundles, individual cables are placed into a plastic disk with 84 holes tightly packed into concentric hexagonal rings as shown in figure 7.7. Since 72 fibers are designated for individual calorimeter OMs while 4 are for the reference OMs, eight fibers remain as spares in the event of damage to fibers during installation or maintenance. The hexagonal ring pattern was chosen to maximize compactness of the bundle and thus aid the uniformity of light illumination. The LED light intensity drops off quickly as a function of radial distance from the central axis as will be described in a subsequent section on optical performance. This disk is then inserted into a plastic collar piece which couples to the light cone. The collar piece is filled with epoxy to secure the fibers into the disk and the disk into the collar. Once the epoxy has cured the entire ensemble is fly cut, using the same tool which fly cuts individual fibers, to create a smooth, flat face onto which the LED will shine.

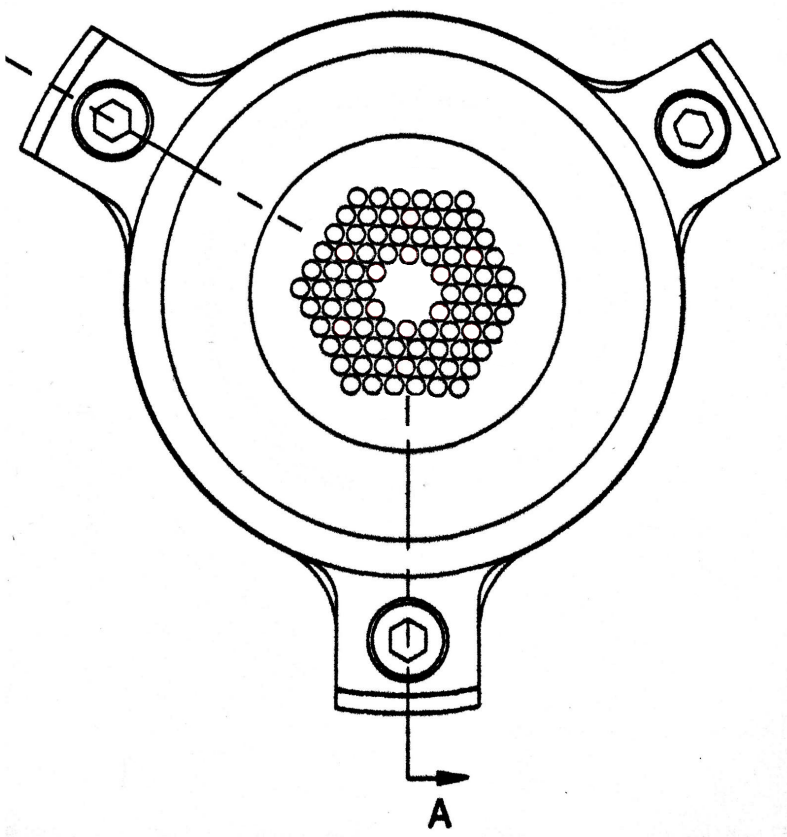

Figure 7.7: An axial view of the fiber bundle face depicting the layout of the 84 fibers. Bundles can be characterized after being made so that the 12 spare fibers are those producing the lowest light levels.

Reference Optical Modules

The last components of the LI system are those making up the reference OMs. These will track the stability of the LEDs by comparing the output UV light against a calibration source of either ^{207}Bi or ^{241}Am . Since these sources are external to the detector they can be of much higher activities and will be constantly monitored by the reference OMs. The final configuration consists of two each of different types of reference OMs for a total of four (though the LI rack was designed with additional space to include other possible reference OMs if better options are found in the future). The first type will be nearly identical to a SuperNEMO main-wall calorimeter

OM to reduce systematic effects during monitoring. The only difference these reference OMs and a main-wall calorimeter OM is that 20 holes (instead of two) will be drilled into the scintillator blocks of the reference OMs to inject light from each of the LI LEDs. These OMs will reside in the lower LI rack compartment, with their entrance face pointing downwards, above a small platform with a recess to hold the calibration sources. This platform will function to secure the sources in place and couple them to the entrance face of the reference OMs. This type of reference OM, using a large scintilltor block and being external to the detector, will be susceptible to much higher rates of background interactions which will overlap the spectra of the calibration sources. For this reason a second type of reference OM will also be used which resembles the one used in the LI test bench (described in section7.4). This one couples a much smaller scintillator and PMT together but the final dimensions, structure, and PMT choice are still being finalized. This will reside in the upper LI rack compartment.

For the large block type reference OMs the calibration sources will be ^{207}Bi , as used in the calibration of calorimeter OMs during source deployment runs. The small reference OMs meanwhile will use ^{241}Am as used during successful test bench runs during evaluation of the LI system's performance.

7.3 Optical Performance

Stimulating the desired dynamic range of SuperNEMO OMs with the LI system requires being able to deliver light levels from hundreds of photo-electrons up to many thousands of photo-electrons. Furthermore, to ensure that monitoring and linearity measurements are carried out to the same accuracy, the calorimeter OMs should receive roughly the same amounts of light. Optical losses need to be minimized

to prevent limitations of our range and uniformity. These arise anytime the UV LED light must be transmitted through a medium or transmitted between different media. The main sources of optical losses are described below along with the techniques that have been used to combat them.

Fiber Optics Cables and Transitions

Typical optical fibers are not optimized for the transmission of UV light and thus attenuation values are generally greater than those given by the manufacturer. To measure the expected light attenuation under similar conditions to actual SuperNEMO LI survey runs, the intensity of the UV LED light was measured across different lengths of LI optical fiber. Pieces were made of lengths ranging from $2 - 20\,\mathrm{m}$ in $2\,\mathrm{m}$ increments and the intensity values of LED light though each piece were plotted as a function of the length. The resultant function was then fitted using an expression of the form

$$I = I_0 \times e^{-x/L}, \tag{7.3.1}$$

where I is the intensity measured, I_0 is the intensity that would be expected at zero fiber length, x is the fiber length, and L is a characteristic attenuation length which gives the value of x such that the intensity would drop by a factor of e. From the fit, a value of $L = 9.699 \pm 0.006\,\mathrm{m}$ is estimated for the characteristic attenuation length of the fiber using the UV LEDs selected for the LI system. The full final length of of fiber that will be used in the system is not finalized but expected to be nearly $15\,\mathrm{m}$ which would lead to a loss of 78.7% of the light due to transmission effects alone. No significant deviations in attenuation have been observed from fiber to fiber so these transmission losses should mainly affect the overall light levels and not the uniformity of light across different OMs.

The other transmission related light loss that is expected is due to the optical connectors used to couple the long fiber cables to the pig tail pieces. A great deal of optimization has gone into the design of the connectors to minimize losses and ensure that variations from one connector to the other are minimal. This changes included redesigns of the connector components themselves (such as the addition of the locking mechanism to secure the carrier within the bulkhead) and optimization of the fly-cutting parameters to improve the surface finish on matching fiber faces. In addition to improving the light transmission across the connectors, these changes also reduced the variation from one connector to the next so that the connectors have a smaller impact on the overall uniformity of light levels being sent through the LI system. The improvements in the optical connectors are summarized in table 7.1 where the transmission percentages (percentage of light transmitted across the connector) for each generation of connectors is shown as well as the spread in this value across testing multiple connectors.

Carrier Design	**Transmission**
First Gen.	$61 \pm 13\%$
Second Gen.	$78 \pm 14\%$
Third Gen.	$84 \pm 8\%$

Table 7.1: Tabulated results of the transmission across a connector relative to its baseline no-connector run for each for each design generation. Not only were there improvements in overall transmission but also in the consistency of the transmission values (as denoted by the reduction in the errors).

Fiber Bundle Illumination

The light produced by most LEDs is passed through a lens characterized by a half-intensity (or viewing) angle which denotes twice the angle, relative to the illumination axis, at which the light intensity drops by 50% compared to the on axis value (at zero degrees). This is important because when trying to illuminate a bundle of fibers with an LED, those fibers which are radially further from the central axis will receive less light than those which are closer. This effect is further compounded by the Fresnel Effect which describes how the intensity of light changes as it cross from one media to another (in this case from air in the light cone into the PMMA that constitutes the fibers). The reflectance, or fraction of power that is reflected at the interface, depends on the polarization of the light and is given by

$$R_S = \left| \frac{n_1 cos\theta_i - n_2\sqrt{1-(\frac{n_1}{n_2}sin\theta_i)^2}}{n_1 cos\theta_i + n_2\sqrt{1-(\frac{n_1}{n_2}sin\theta_i)^2}} \right|^2, \tag{7.3.2}$$

for light polarized perpendicular to the plane of incidence (s-polarization) and

$$R_P = \left| \frac{n_1\sqrt{1-(\frac{n_1}{n_2}sin\theta_i)^2} - n_2 cos\theta_i}{n_1\sqrt{1-(\frac{n_1}{n_2}sin\theta_i)^2} + n_2 cos\theta_i} \right|^2, \tag{7.3.3}$$

for light polarized parallel to the plane of incidence (p-polarization). Here n_1 and n_2 are the indices of refraction of the two media, air and PMMA, and θ_i is the angle of incidence of the light. For an LED, the light is generally unpolarized so that the total reflectance is simply and average of the two expressions above,

$$R = \frac{R_S + R_P}{2}. \tag{7.3.4}$$

The transmittance, or fraction of power transmitted at the interface, is then given by conservation of total energy as

$$T = 1 - R. \tag{7.3.5}$$

It can then be shown that as θ_i is increased, R gets larger and approaches unity while T gets smaller and approaches zero. For our fiber bundle this means that those which are located radially further out from the illumination axis will receive the LED light at a larger angle of incidence and thus transmit less of the light into the fiber. This effect thus compounds with the radial dependence of LED illumination to further exacerbate light losses for fibers at increasing radial distance.

Part of the reason the chosen LEDs were selected was that, compared to other LEDs with similar properties, the VCC LEDs gave the best bundle illumination uniformity prior to making any optimizations. In order to test this, the light distribution components were all assembled and coupled to a test bundle, shown in figure 7.8a, containing 101 total fibers in a pattern of hexagonal rings. Since fibers completely covered the bundle face this test bundle provided a good mapping of the bundle response to LED illumination. The light intensity on the other end of each fiber was measured using a spectrometer and the values were normalized to the brightest fiber(s) in the bundle, normally the central fiber or the fiber(s) very near the center of the bundle. The result of this test is shown in figure 7.8b.

As one would expect the uniformity test shows that the intensities generally decrease moving outwards from the center of the bundle. What made this LED so desirable was the fact that even in this test bundle, only 20 fibers had losses greater than 50% relative to the maximal fiber. This implies that the bundle is uniform to within a factor of two for about 80 of the fibers.

Although this particular LED already provides acceptable levels of uniformity (there were 76 or more fibers with intensities within a factor of two difference) studies are still underway to improve this for the particular bundle configuration that will be used in for the LI system. It was discovered that using the fly cutting machine

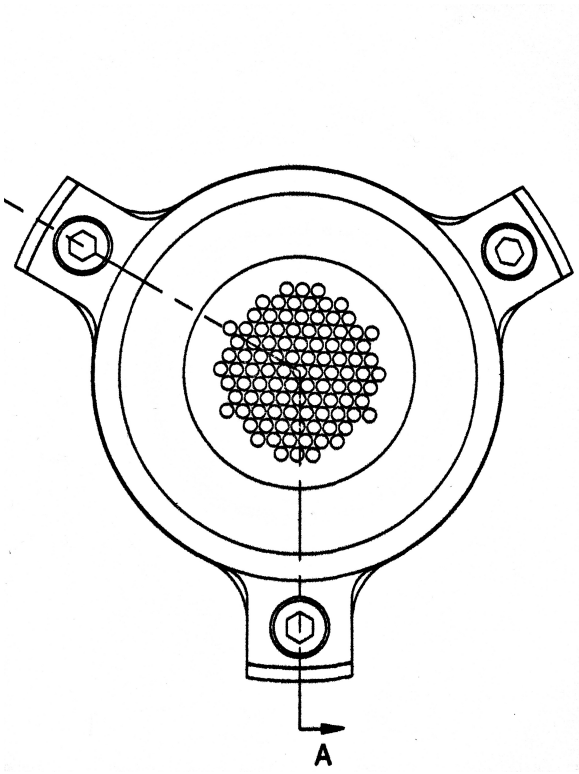

(a) An axial view of the test fiber bundle containing 101 fibers.

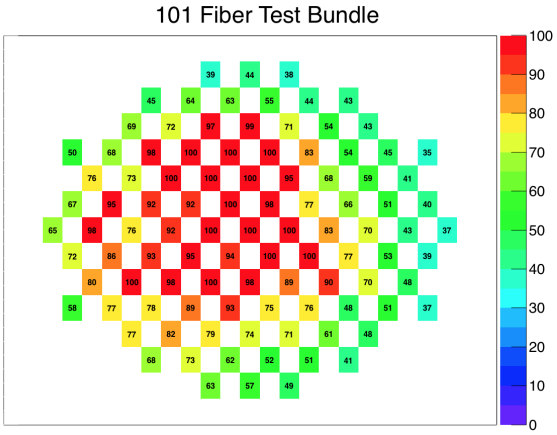

(b) Results of the uniformity test measuring the relative intensity variations from one bundle fiber to the next.

Figure 7.8: The figures above show a fiber bundle is used to test the illumination uniformity of the LEDs. The left figure illustrates how the 101 fibers are organized. The right figure shows how the relative LED light intensity varies from one fiber to another. The values are normalized to brightest fiber(s).

to remove part of the plastic lens material of the LEDs results in an illumination pattern that better matches the ring formation of the fiber bundle. Basically, cutting a small portion of the tip of the LED led to a slight decreases in the relative intensity of central fibers but better uniformity for a ring of fibers. This is demonstrated in figure 7.9 where approximately one quarter of a millimeter was removed from an LED before illuminating the bundle. Now there are only seven fibers with relative light levels below 50%. Four of these are towards the bundle center with only three towards the outside.

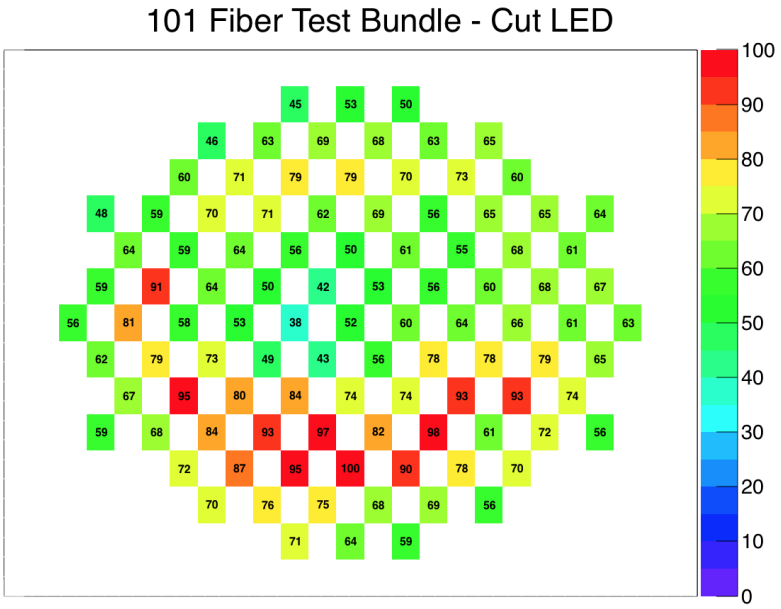

Figure 7.9: Results of the uniformity test measuring the relative intensity variations after a quarter of a millimeter worth of material was removed from the LED face.

Further tests are being carried out to determine the optimal amount of material that should be removed to maximize the uniformity across all 84 fibers that will be in the final LI system bundles.

7.4 Optical Module Monitoring Performance

To test the system's ability to accurately monitor the response of an OM a test bench was setup consisting of a test calorimeter OM and a small makeshift reference OM both contained inside of a light tight box which had feedthroughs to accept fiber optic cables from the LI system. The setup is described in more detail in the subsequent section along with the results of continuously monitoring the test calorimeter OM for extended periods of time.

Test Bench

The test bench used to study the LI system consisted of the following: A dark box containing the test and reference OMs, an electronics rack containing the pulser box system with fibers leading into the dark box, a separate electronics rack to house the necessary electronics for power supply and data acquisition (DAQ), and a computer to control the pulser box and read the data in from the DAQ.

The test calorimeter OM was assembled to be as similar as possible to a true SuperNEMO main wall calorimeter OM but it differed in some key aspects. It consisted of a true SuperNEMO style $256\,\text{mm} \times 256\,\text{mm} \times 194\,\text{mm}$ polystyrene scintillator block coupled to an 8 inch Hamamatsu R5912 PMT. The block was wrapped on the lateral faces with two layers of Teflon tape while the entrance face was covered with $2.5\,\mu\text{m}$ thick aluminized Mylar. Unlike a true production OM, the lateral and rear faces were not also covered with the aluminized Mylar. The rear face was covered partially with additional Teflon tape but also had a piece of black felt overlaying the surface with holes allowing the PMT and fiber optic cable to pass through. One of the most important difference between the test and true OMs however is in the PMT coupling. In a true SuperNEMO OM the PMT is glued into a hemispherical recess

in the scintillator block using a epoxy with index of refraction chosen to maximize the light transmission between the two media. It was desired to leave the test bench OM only temporarily coupled though in order to use the individual components for other studies. For this reason the PMT simply sat in the hemispherical recess with no coupling media and the entire OM was oriented vertically (entrance face downwards) to support the PMT. The OM was supported on two pieces of wood so that the calibration ^{207}Bi source could be inserted underneath the center of the OM's entrance face, as close as possible, to minimize electron energy losses. Early tests with the calibration source and LED light gave estimates of this OM's energy resolution to be approximately 14% FWHM (Full-Width at Half-Maximum) at 1 MeV which is significantly worse than the 9% achievable when properly assembling a true SuperNEMO calorimeter OM. This is due to a reduced light collection efficiency for the test OM but in the end this implies that our monitoring results should only improve when applied to production OMs with better resolution and performance.

The reference OM went through a few prototype designs before a good configuration was found for testing. This model, which was only minimally optimized and thus will not reflect the final design, consisted of a 1 inch Hamamatsu R1398 PMT which had a special plastic mounting piece that fit over the face of the PMT and held a fiber optic cable in line with the axis of the PMT. A small ^{241}Am source disk about 1 cm tall and 1 cm in diameter was placed inside this plastic mounting and sat just below the fiber. In this way, light from both the fiber and the source disk could reach the PMT face but neither of them were directly coupled to the PMT glass. Furthermore, the ^{241}Am source was not directly on axis with the PMT (like the fiber) which further restricted some of the light from reaching the PMT. Regardless of these initial limitations, this reference OM was still able to see enough of the

LED and ^{241}Am source light to carry out its functions at the desired accuracy levels. This implies, once again, that the production model with improved design could also yield improved calibration and monitoring performance.

The two test bench OMs were housed in a light tight dark box, shown below in figure 7.10, containing feedthrough panels to bring in fiber optical light and signal and power cables for the PMTs. All of the necessary electronics to power and process the signals of the two OMs were house in an electronics rack next to the box and a diagram representing the data acquisition (DAQ) system is shown in figure 7.11. For each PMT, the signal was passed first into a linear fan-in/out NIM module which generates two copies of the signal. The first of these, for each PMT, is passed into one channel of an 8-channel discriminator with thresholds set at 10 mV. The outputs from each channel are passed then through a second discriminator which can create a "or" gate if either of the PMT pulses pass the first discriminator. This gate is an 80 ns NIM pulse that can then be supplied to a 12-channel Lecroy 2249 ADC to determine when to integrate the input signal. These input signal come from the second copy of the PMT pulses generated by the linear fan but they are first delayed by about 120 ns worth of cable to fit within the generated gate. Data from the ADC module is then read out to a computer via a JORWAY CAMAC module. The computer software creates histograms of the charge spectra collected from the ADC and saves them into ROOT files for later analysis.

A separate script was used to automate data acquisition and collected 30 minutes long samples repeatedly for any given number of iterations (generally on the order of a few hundred to few thousand runs). This was repeated to study the behavior of the system over timescales on the order of a month or more. Although true LI system will only perform surveys once or twice a day, the continuous surveys taken for these

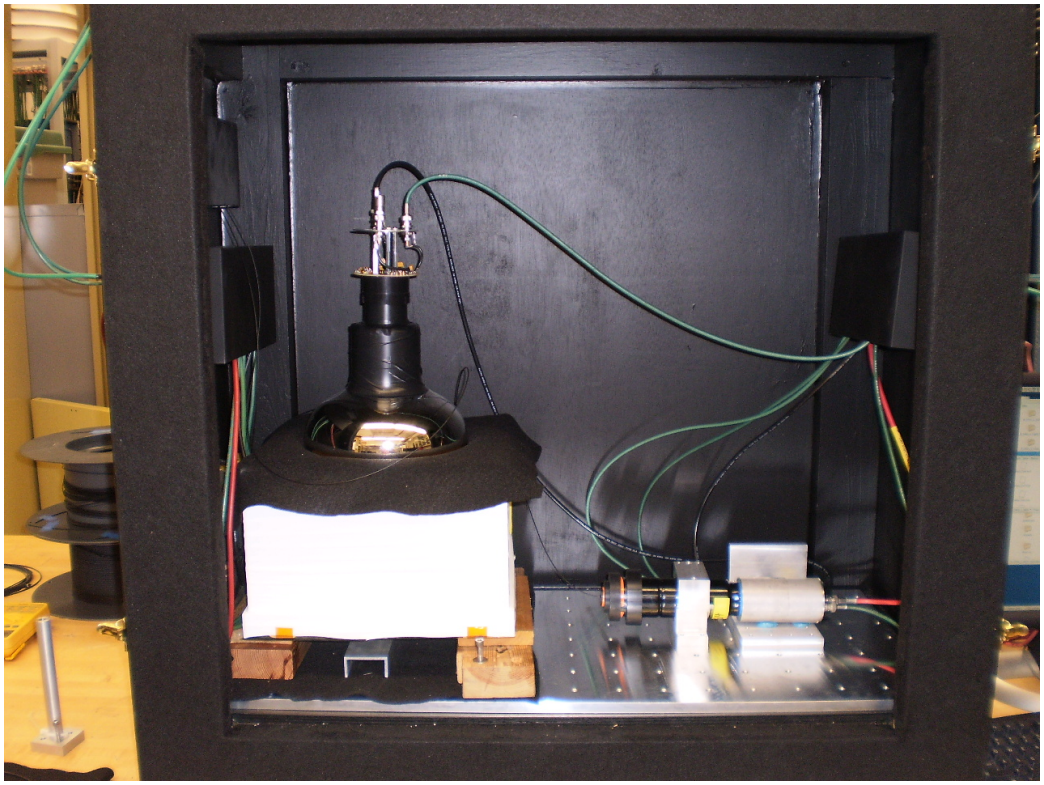

Figure 7.10: A photograph of the test bench dark box setup to study the performance of the LI system. On the right is an approximation of a SuperNEMO 8-inch main wall OM which sits over a ^{207}Bi calibration source and receives LED light via an optical fiber inserted in to the scintillator block. On the left is the reference OM which observes both a fiber from the same LED as well as a small ^{241}Am scintillation source.

tests were chosen to better study the short term fluctuations that affect the system.

A charge spectrum collected by the ADC for each PMT is shown below in figure 7.12 with the test calorimeter OM spectrum on the left and the reference OM spectrum on the right. The histogram is in units of ADC which can be converted to charge using the conversion factor of 0.25 pC per ADC channel as supplied by the manufacturer. In the calorimeter OM spectrum, two peaks can be discerned overlapping with a decaying exponential term. These correspond to the conversion electrons emitted by the ^{207}Bi source. The background here is due to a combination of natural radioactivity, cosmic rays, and γ-rays emitted from the ^{207}Bi source. The remaining

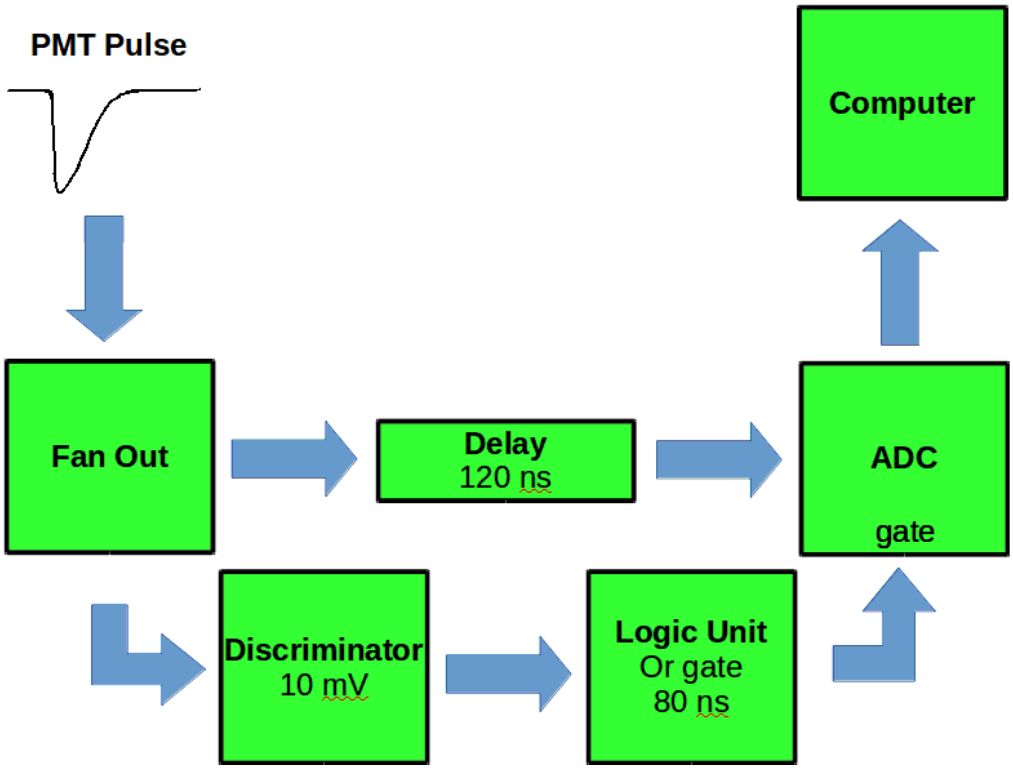

Figure 7.11: A diagram representing the DAQ system for the LI test bench.

right-most peak in this spectrum is from the LED light where the brightness was tuned so that this peak was well separated from the rest of the spectrum. In the reference OM spectrum there are just two well defined peaks. The left-most is due to the α particles from the ^{241}Am source while the right-most is once again due to the LED light. Since the scintillator used for the reference OM was much smaller in this setup there is negligible amounts of background events in this spectrum.

The collected charge spectra are then fitted via ROOT to obtain positions (in terms of ADC units) of each peak: the ^{207}Bi and ^{241}Am source peaks as well as those corresponding to the injected LED light in each OM. Predefined functions in ROOT can be used for the LED and ^{241}Am spectra but a custom fit function [89] is used for the ^{207}Bi spectrum and its overlapping backgrounds. This function is shown in

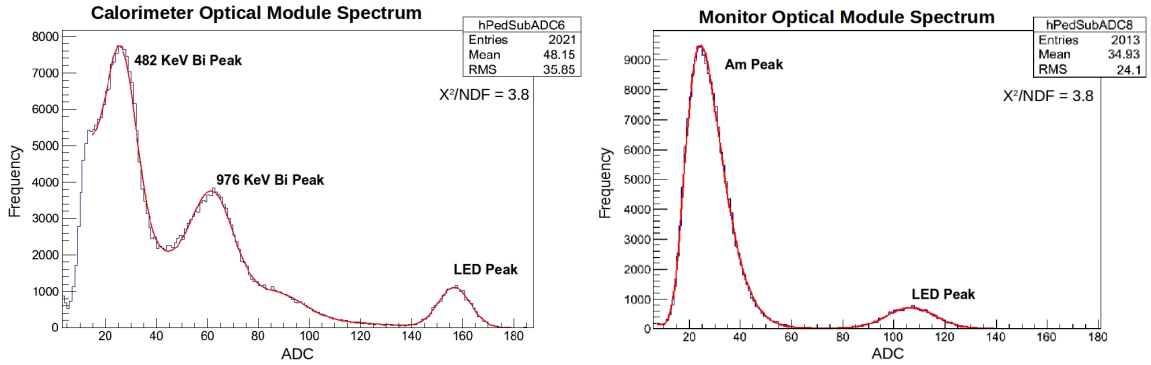

Figure 7.12: These histograms show the charge spectra collected by each OM. The test calorimeter OM histogram (left) shows the characteristic ^{207}Bi spectrum alongside its LED spectrum while the reference OM histogram (right) shows its ^{241}Am and LED spectrum. The red lines in each denote fits to the distribution which are used to get the position of each peak.

equation 7.4.1.

$$\begin{aligned} y = {} & A_1 \left(7.11 \times G(\mu_{1,k}, \sigma_1) + 1.84 \times G(\mu_{1,l}, \sigma_1) + 0.441 \times G(\mu_{1,m}, \sigma_1)\right) \\ & + A_2 \left(1.548 \times G(\mu_{2,k}, \sigma_2) + 0.429 \times G(\mu_{2,l}, \sigma_2) + 0.1057 \times G(\mu_{2,m}, \sigma_2)\right) \\ & + A_{bkg}\ e^{-x/c_1} + c_2 \end{aligned} \tag{7.4.1}$$

Where:

$$G(\mu_{i,\alpha}, \sigma_i) = \frac{1}{\sigma_i\sqrt{2\pi}} \times e^{-(x-\mu_{i,\alpha})^2/2\sigma_i^2} \text{ ; for } i = 1, 2 \text{ and } \alpha = k, l, m. \tag{7.4.2}$$

Here the A_i, A_{bkg}, $\mu_{i,\alpha}$, σ_i, and c_i are free parameters determined by the fit. One can see each peak, denoted by the numbered subscript with $i = 1$ for the 482 keV peak and $i = 2$ for the 976 keV peak, is fitted with a convolution of three Gaussian terms since each peak actually consists of three conversion electrons corresponding to the three shells from which they can originate: the k, l, or m shell of the atom (denoted by the second lettered subscripts above). The energies differ very slightly depending on which shell the electron originated from and each has a slightly different branching ratio as expressed by the coefficient that precedes each Gaussian term above.

Stability and Monitoring

In order to validate the ability of the LI system to monitor the test calorimeter OM at the 1% level it is sufficient to prove that the response of the OM can be predicted to the same level of accuracy using only the LI system. The procedure to do this is as follows:

1. First a baseline calibration point is established using the first LI run (as described above), fitting all of the peaks, and setting the peak position values to be the $t = 0$ data points. This represents a successful ^{207}Bi calibration run in the true detector wherein the state of the calorimeter response is well known.

2. Next, successive runs are taken to continually monitor the system over the course of several several days, weeks, or months. For each of these runs all the peaks are once again fitted and those that are due to the LED in each each OM along with the ^{241}Am peak in the reference OM are used to predict the position of the ^{207}Bi peaks in the calorimeter OM.

3. Finally, the predicted and measured responses are compared by taking the ratio of two ^{207}Bi peak positions in the calorimeter OM. As this is done for successively more runs this provides a measure of how well the system can monitor the response as time increases.

Although there are two ^{207}Bi conversion electron peaks that can be used for calibrating the calorimeter OM the analysis of the monitoring performance focused solely on the 976 keV peak since it was seen to be a better metric for the OM's response (thus from this point on any reference to the ^{207}Bi peak is taken to be the 976 keV peak). As an example of how the calorimeter OM response changes over time, this

976 keV ^{207}Bi peak position is shown as a function of time (over the course of about one month, in figure 7.13. The drift in the response is even smaller than 1% in this time frame.

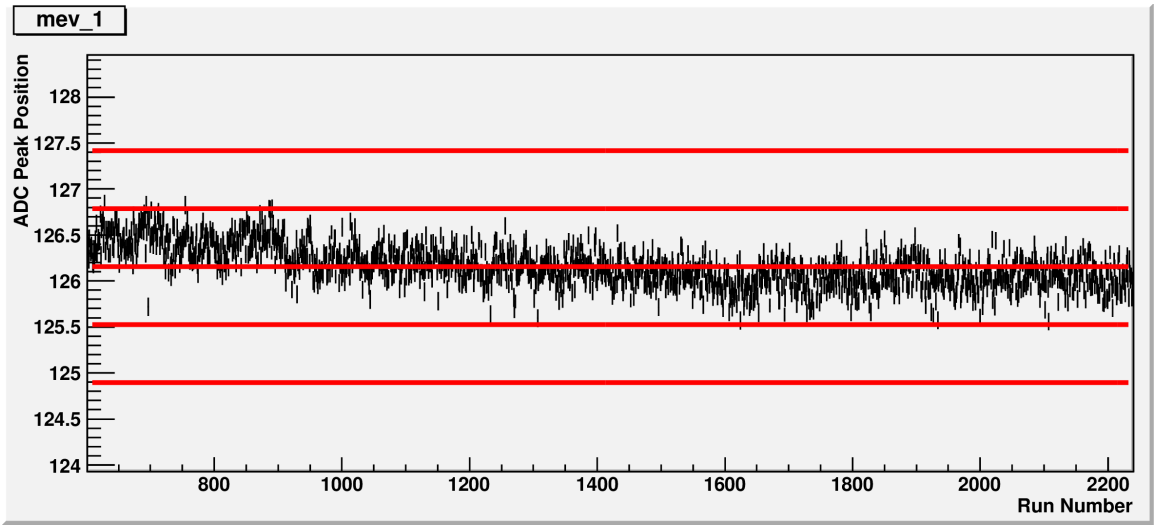

Figure 7.13: A plot of fitted peak position for the 976 keV ^{207}Bi electron versus run number essentially shows the time evolution of the test optical module's response. It is stable to better than 1% over the course of about one month.

Now for the predicted peak position, let the time $t = 0$ peaks be denoted by Bi_0 and LED_0^{calo} for the test calorimeter OM peaks and Am_0 and LED_0^{ref} for the reference OM peaks. Similarly at later times the peak positions will be given by Bi_t, LED_t^{calo}, Am_t, and LED_t^{ref}. The predicted response of the calorimeter OM will be given by Bi_t^{pred} and it is calculated using only the time $t = 0$ values along with the later time values that are inherent to the LI system (namely the later positions of the two LED peaks and the ^{241}Am peak). The equation for determining Bi_t^{pred} is

$$Bi_t^{pred} = Bi_0 \times \frac{LED_t^{calo}}{LED_0^{calo}} \times \frac{LED_0^{ref}}{LED_t^{ref}} \times \frac{Am_t}{Am_0}. \tag{7.4.3}$$

Essentially, the relative changes in the ^{241}Am are used to correct for instabilities in the reference OM's measurement of the LED. Then the relative changes in the LED

as seen by the two OMs is used to predict the change in the ^{207}Bi peak position relative to its starting location. Once we have the predicted value we can construct the time-dependent ratio $r(t) = Bi_t^{pred}/Bi_t$. The results should lie on or near a perfectly flat horizontal line at $r(t) = 1$ (i.e. predictions match data exactly) and should not drift by more than 1%, $0.99 < r < 1.01$, within an acceptable time frame between calibration runs.

As an added challenge for the system, the gain of the calorimeter PMT was periodically changed slightly (by adjusting the high voltage applied within $\pm 100\,\mathrm{V}$ from nominal). Although Small fluctuations in response may be expected due to power supply instabilities or other environmental effects, these forced changes were intended to be much larger to test the system under more stressful conditions. The results of monitoring the prediction ratio, r, over the course of many such induced changes is shown in figure 7.14. The central horizontal red line is a fit to the data points while the red lines above and below are limits on the drift at the 1% level.

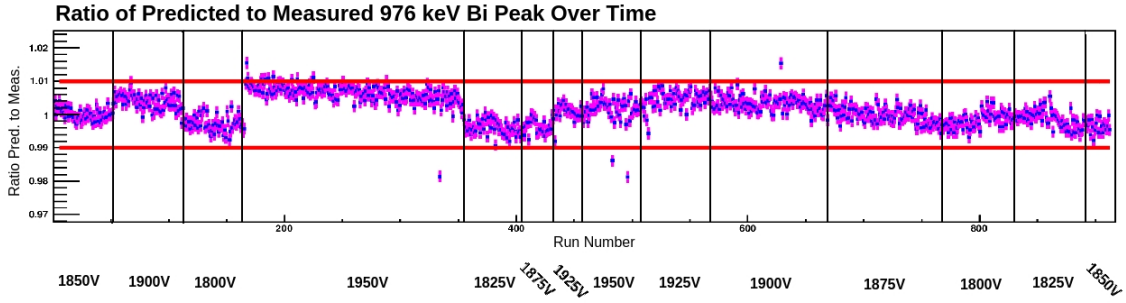

Figure 7.14: A plot of the ratio of the predicted to measured peak position for the 976 keV ^{207}Bi electron shows that our ratio is centered around the central line at $r = 1$ (i.e. the measured and predicted values are equal) and deviates by no more than 1% as designated by the red bounding lines.

Temperature Dependence

In order to understand the degree to which temperature changes might affect the system, thermocouples were distributed in various location in or around our test bench to monitor the ambient temperatures and compare their fluctuations against those of the different LI system components. Three locations were used to collect temperature readings: inside the light tight enclosure housing the calorimeter and reference OMs, inside the pulser box near the LED driver board, and outside the test bench but in the general vicinity of the setup. The latter essentially measured changes in the laboratory's ambient temperature while the former two studies changes near the OMs and LEDs, respectively. These temperature readings were then compared against fluctuations in the different OM responses as given by the various peak positions over time or the main figure of merit, the ratio r. Figure 7.15 shows an example of one temperature measurement (that of the general laboratory area) over time plotted alongside the response of the reference OM (since it seemed to be most affected by temperature) in terms of the LED and ^{241}Am peak positions over time. From the plots it can be seen that fluctuations in both temperature and reference OM response are generally periodic though they are roughly anti-correlated. The period for fluctuations corresponds well with the day/night cycle and the pauses in the periodicity usually correspond to weekends or other times where the lab was mostly unoccupied and undisturbed.

The test calorimeter OM showed identical behavior albeit to a slightly lesser extent and the other recorded temperatures also did not differ greatly from the lab temperature (except perhaps in small overall offsets). In order to better portray the correlations between temperate and OM responses, the relative change in each were plotted versus one another and the results are displayed in figure 7.16).

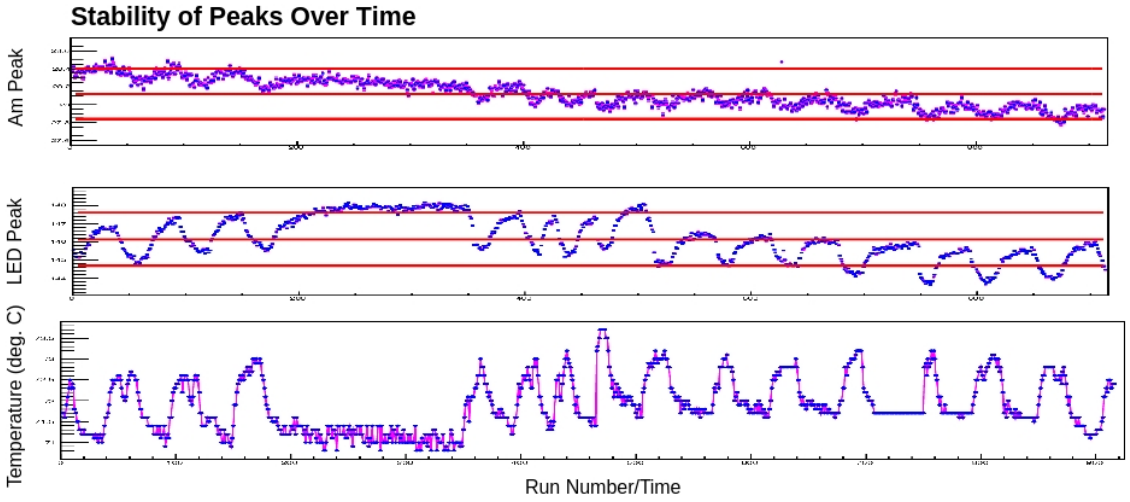

Figure 7.15: The top two plots show fluctuations observed in the two monitor PMT peaks (that of the ^{241}Am and LED) over time while the bottom plot shows the measured lab temperature over the same time period. It is evident that there is a correlation between the ambient temperature and the response of our monitor PMT. Not shown are similar plots for the test calorimeter optical module or the dark box and pulser box temperatures. These show identical behavior to plots shown.

For each plot the Pearson correlation coefficient is given which determines the strength of the correlation between the two plotted variable (A value of closer to 0 would denote a weaker correlation while a value close to ± 1 denotes a stronger correlation/anti-correlation). As evidenced in the previous plot, the Pearson correlation coefficient confirms a strong anti-correlation between the LED peak position and lab temperature (with $R = -0.95$) and also a milder correlation between the ^{241}Am peak position and lab temperature (with $R = -0.54$).

The most important question however is whether or not the temperature affects the ability of the LI system to predict the response of the calorimeter OM. Recall that the metric for testing this was the ratio r between the predicted and measured ^{207}Bi peak position. If the correlation is studied between temperature and this variable we see that the correlation is very weak ($R = 0.21$).

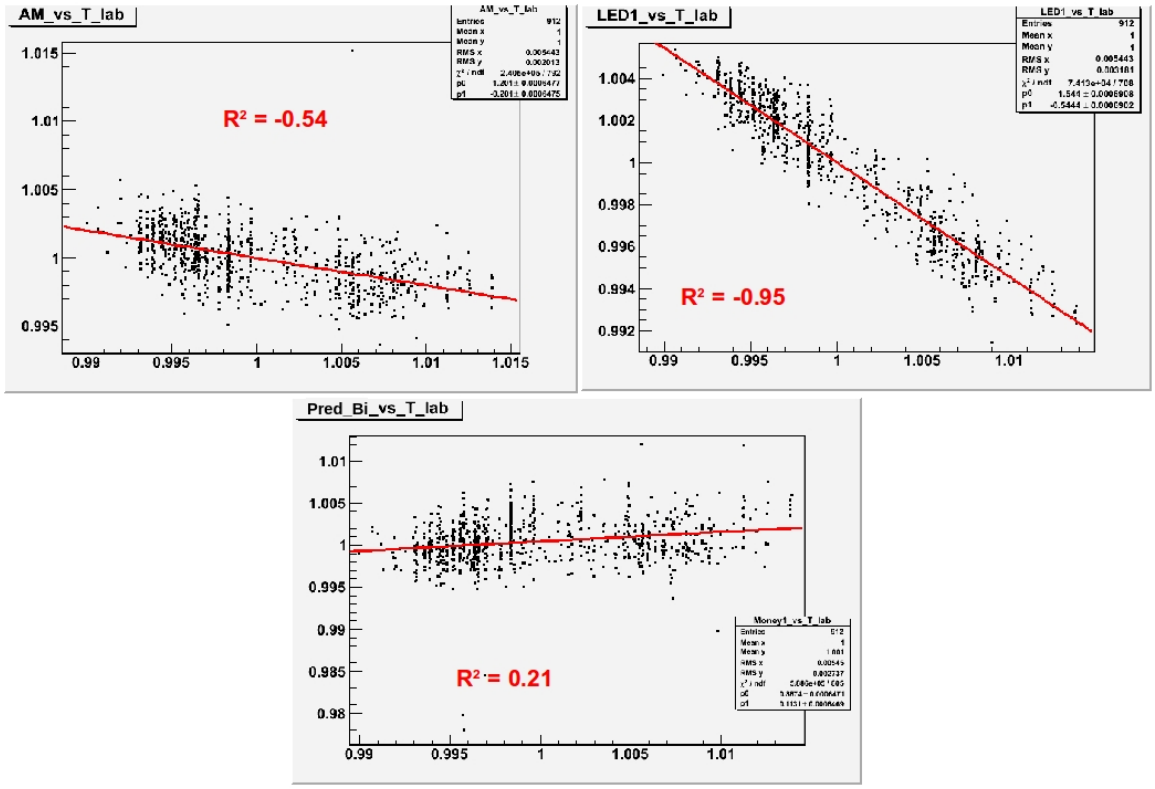

Figure 7.16: The upper left plot shows relative changes in the ^{241}Am peak position versus relative change in lab temperature with a Pearson correlation coefficient of -0.54. The upper right plot shows the same thing though for the LED peak position and now the correlation is much stronger at -0.95. The lower plot shows the correlation between our predicted ^{207}Bi peak and temperature and here the correlation is much weaker thus demonstrating the diminished effect of temperature on the goal of the LI system

Chapter Eight: Conclusions

Searching for time variation in fundamental constant of nature has long been an active area of research in probing the limits of current physics models. Observations of such a phenomena could hint at BSM physics which may ultimately lead to a more fundamental understanding of the workings and interactions of the known constituents of the universe. Past and recent experiments trying to detect such fluctuations have done so by studying, on various time scales, different processes that these constants underlie such as nucleosynthesis, atomic transitions, and nuclear decays. If observed, temporal fluctuations (periodic or otherwise) in such processes could be traced back to specific constants associated with the interactions involved such as the strong, weak, or electromagnetic forces. The end result would have dramatic implications for fundamental physics as well as cosmology, astrophysics, and nuclear physics.

Recent studies of β decay rates have yielded claims [4] [5] [52] [53] [55] [67] [70] for oscillatory behavior with periods that suggest possible solar influences. As of this writing, counter claims have been demonstrated based on other experiments but a definitive conclusion has yet to be reached. Searches in other isotopes and other decay types have introduced more complexity and questions on how, if at all, the modulations are affected by decay type and isotope.

The NEMO-3 experiment was designed with the goal of searching for $0\nu\beta\beta$ decay and measurement of $2\nu\beta\beta$ decay of several isotopes by employing a combination of tracking and calorimetry based techniques to reconstruct full decay topologies. The detector was situated in the Laboratoire Souterrain de Modane where it operated from 2003 - 2011 while observing nearly 10 kg of source isotopes. The most abundant

isotope in the detector was ^{100}Mo , for which 6.9 kg were amassed, which produced a very pure data set of $\beta\beta$ decay events with signal to background ratio of 76 (in the low-radon Phase 2 data set). A complete description of this detector and its operation are presented herein followed by a thorough explanation of the analysis of its data.

The world's first ever search for variations in a second-order weak decay rate, namely in the $\beta\beta$ decay of ^{100}Mo , is presented in this thesis. Two nearly identical frequency-domain analysis techniques, both suited for analyzing unevenly sampled data, were applied to the Phase 2 data set spanning 6.02 yrs from October 24^{th}, 2004 until November 1^{st}, 2010. Both techniques involve the construction of a periodogram which calculates the power of different sample frequencies as they appear in the data (it is equivalent to a least squares fitting of sine-waves to the data). The two are used as a cross check of one another but the only difference between them is that one is a more generalized form which accounts for offsets of the times series and accounts for weighted data points. The sample frequency range is bound by the smallest and largest periods that can be observed in the data: the minimal period being half the average spacing between data points and the largest being about twice the full span of the data. An oversampling factor of four was chosen so that a total of 15460 frequencies between $0.083063 - 365.25\,\mathrm{yrs}^{-1}$ were sampled by each technique to construct the periodogram. In both periodograms, no frequency produced a peak in the power spectrum with significance higher a 60% C.L. Therefore, the data does not support a claim for any periodic modulations in the $\beta\beta$ decay rate of ^{100}Mo in the range of sampled frequencies. Instead, limits can be placed based on sensitivity studies done with Monte Carlo data sets. Considering the claim for yearly

modulations (a frequency of $1\,\mathrm{yrs}^{-1}$), the modulation amplitude must satisfy

$$A < 2.1\%(90\%\,\mathrm{C.L.}). \tag{8.0.1}$$

The latter half of this work introduced the SuperNEMO experiment as the successor of NEMO-3. This experiment will employ the same proven strategy of the NEMO tracking and calorimetry technique to search for $0\nu\beta\beta$ decay with $T_{1/2}$ sensitivities of order 10^{26} yrs corresponding to an effective Majorana mass of $\langle m_{\beta\beta}\rangle < 50-100\,\mathrm{meV}$. A full summary is presented herein of the overall SuperNEMO design and where and how it improves over the NEMO-3 detector.

In addition to the general advances of SuperNEMO over is predecessor, an overview was also given of the Light Injection (LI) monitoring system that will track the response of each of the 712 SuperNEMO calorimeter modules. The R&D required to establish the final design was presented along with the results from an early prototype, referred to as the LI Test Bench, which demonstrated its ability to track the response of a test optical module for over a month with a precision of $\pm 1\%$. This system, along with the SuperNEMO Demonstrator itself, is currently under construction and is slated for completion early next year when it will be installed in the LSM alongside the Demonstrator and help it reach its sensitivity goals.

It is expected that the SuperNEMO Demonstrator will be turned on and begin collecting data in the second half of 2017. It has been designed with the target of reaching NEMO-3 levels of sensitivity after only one year of operation and as with its predecessor it will also use its early data set to establish what backgrounds are present at significant levels and measure their activities.

Future SuperNEMO detector modules will then continue the success of the Demonstrator while adding more isotope mass. At the same time the flexibility of the program will allow future modules to benefit from advance in different technologies such

as PMT and scintillator development, isotope enrichment, or material radiopurity improvements, all of which will contribute to a higher sensitivity to detecting $0\nu\beta\beta$ decay.

Bibliography

[1] J. P. Uzan, *The stability of fundamental constants*, Comptes Rendus Physique **16** (2015) 576-585. 1

[2] C. Nassif, A. C. Amaro de Faria Jr., *Variation of the fundamental constants over the cosmological time: veracity of Dirac's intriguing hypothesis*, Can. J. Phys. **94** (2016) 89-94. 1

[3] J. Solà, *Fundamental Constants in Physics and Their Time Variation: Preface*, Mod. Phys. Lett. A **30** (2015) 1502004. 1

[4] P. A. Sturrock, et al., *Concerning the variability of beta-decay measurements*, arXiv:1510.05996 [nucl-ex] (2015). 1, 20, 162

[5] P. A. Sturrock, et al., *Analysis of beta-decay rates for Ag108, Ba133, Eu152, Eu154, Kr85, Ra226, and Sr90, measured at the Physikalisch-Technische Bundesanstalt from 1990 TO 1996*, The Astrophysical Journal, **794** (2014) 42 (6pp). 1, 162

[6] D. O'Keefe, et al., *Spectral content of $^{22}Na/^{44}Ti$ decay data: implications for a solar influence*, Astrophys. Space Sci. **344** (2013) 297303. 1

[7] P. A. M. Dirac, *A New Basis for Cosmology*, Proceedings of the Royal Society A **165** (921): 199208. 3

[8] J. P. Uzan, *Varying Constants Gravitation and Cosmology*, Living Rev. Relativity, **14** (2011) 2. 3

[9] W.J. Marciano, *Time Variation of the Fundamental "Constants" and Kaluza-Klein Theories*, Phys. Rev. Lett., **52** (1984) 489. 3

[10] K. A. Olive *Testing the variation of fundamental constants with astrophysical and spectroscopic data*, Canadian Journal of Physics, 2011, 89(4): 361-369, 10.1139/p10-107 3

[11] E. W. Kolb, et al., *Time variation of fundamental constants, primordial nucleosynthesis, and the size of extra dimensions*, Phys. Rev. D. **33** (1986) 869. 3

[12] H. Oberhummer, A. Csótó and H. Schlattl, *Stellar production rates of carbon and its abundance in the universe*, Science **289** (2000) 88. 4

[13] M. J. Duff, *Comment on time-variation of fundamental constants*, arXive.org, hep-th/0208093 (2002). 4

[14] G. Gabrielse, et al., *New Determination of the Fine Structure Constant from the Electron g Value and QED*, Phys. Rev. Lett. **97**, 030802 (2006), Erratum, Phys. Rev. Lett. **99**, 039902 (2007). 4

[15] M. P. Savedoff, *Physical Constants in Extra-Galactic Nebulae*, Nature **178** (1956) 688-689. 5

[16] A. I. Shlyakhter, *Direct test of the constancy of fundamental nuclear constants*, Nature **264** (1976) 340. 5

[17] S. K. Lamoreaux, J. R. Torgerson, *Neutron moderation in the Oklo natural reactor and the time variation of* α, Phys. Rev. D **69** (2004) 121701. 5

[18] T. Rosenband, et al., *Frequency Ratio of Al+ and Hg+ Single-Ion Optical Clocks; Metrology at the 17th Decimal Place*, Science **319**, 5871 (2008) 18081812. 5

[19] I. I. Shapiro, W. B. Smith, and M. B. Ash, *Gravitational Constant: Experimental Bound on Its Time Variation*, Phys. Rev. Lett. **26** (1971) 27. 6

[20] J. Mould, S. A. Uddin, *Constraining a Possible Variation of G with Type Ia Supernovae*, Publications of the Astronomical Society of Australia **31**, e015, (2014) 6

[21] B. E. J. Pagel, *On the limits to past variability of the proton-electron mass ratio set by quasar absorbtion line redshift*, Mon. Not. R. astr. Soc. **179** (1977) 81-85. 7

[22] J. Bagdonaite, et al., *A Stringent Limit on a Drifting Proton-to-Electron Mass Ration from Alcohol in the Early Universe*, Science **339**, 6115 (2013) 46-48. 7

[23] A. Yahil, *The Interaction Between Science and Philosophy*, edited by Y. Elkana, Humanities, New York (1975), p. 27. 7

[24] C. R. Gould, et al., *Time variability of α from realistic models of Oklo reactors*, Phys. Rev. C **74** (2006) 024607. 7

[25] J. P. Uzan, *The fundamental constants and their variation: observational and theoretical status*, Reviews of Modern Physics **75** (2003) 403-455. 7

[26] F. J. Dyson, *Aspects of Quantum Theory*, ed. A. Salam, E. P. Wigner (Cambridge University Press, Cambridge), (1972) pp. 213-236 8

[27] T. Damour, F. Dyson, *The Oklo bound on the time variation of the fine-structure constant revisited*, Nucl. Phys. B **480** (1996) 37-54. 8

[28] S. M. Carroll, *Quintessence and the Rest of the World: Suppressing Long-Range Interactions*, Phys. Rev. Lett. **81** (1998) 3067-3070. 8

[29] Y. V. Stadnik, V. V. Flambaum, *Can Dark Matter Induce Cosmological Evolution of the Fundamental Constants of Nature*, Phys. Rev. Lett. **115** (2015) 201301. 8

[30] B. Pontecorvo, *Mesonium and anti-mesonium*, Sov. Phys. JETP **6** (1957) 429. 9

[31] H. Becquerel, Comptes Rendus, 501 (1896). 11

[32] H. Becquerel, *Sur la dispersion du rayonnement du radium dans un champ magnetique*, Comptes Rendus **130** (1900), 372-376. 12

[33] J. Chadwick, *Intensittsverteilung im magnetischen Spektren der -Strahlen von Radium B + C*, Deutsche Physikalische Gesellschaft. **16** (1914) 383391. 12

[34] L. M. Brown, *The idea of the neutrino*, Physics Today **31** (1978) 23. 13

[35] E. Fermi, *Tentativo di una teoria dei raggi* β , Il Nuovo Cimento **11** (1934) 119. 13

[36] F. L. Wilson, *Fermi's Theory of Beta Decay*, American Journal of Physics **36** (1968) 1150.

[37] C. L. Cowan, et al., *Detection of the Free Neutrino: a Confirmation*, Science **124** (1956) 1034. 13

[38] C. Weizsacker, *Zur Theorie der Kernmassen*, Z.Phys. **96** (1935) 431458. 15

[39] M. Goeppert-Mayer, *Double Beta-Disintegration*, Phys. Rev. **48** (1935) 512. 17

[40] E. Majorana, *Teoria simmetrica dellelettrone e del positrone*, Nuovo Cimento **14** (1937) 171. 17

[41] W. H. Furry, *On Transition Probabilities in Double Beta-Disintegration*, Phys. Rev. **56** (1939) 1184. 17

[42] R. Henning, *Current status of neutrinoless double-beta decay searches*, Reviews in Physics **1** (2016) 29-35. 18

[43] G. Racah, *On the symmetry of particle and antiparticle*, Nuovo Cim. 14 (1937) 322328.

[44] E. Rutherford, *A radio-active substance emitted from thorium compounds*, Philos. Mag. Ser. 5, **49** (296) (1900), pp. 114. 19

[45] M. Curie, H. Kamerling Onnes, *Sur le rayonnement du radium la temprature de l'hydrogne liquide*, Radium, **10** (6) (1913), pp. 181186. (English version: The radiation of Radium at the temperature of liquid hydrogen. KNAW Proceedings 15 II, 19121913, Amsterdam, (1913) 14301441). 19

[46] S. E. Rutherford, J. Chadwick, and C. Ellis, *Radiations from Radioactive Substances*, Cambridge University Press (1930). 19

[47] G. T. Emery, *Perturbation of nuclear decay rates*, Annu. Rev. Nucl. Sci., **22** (1972), pp. 165202. 19

[48] H. P. Hahn, H. J. Born, J. Kim, *Survey on the rate perturbation of nuclear decay*, Radiochim. Acta, **23** (1976), pp. 2337. 19

[49] J. J. Kraushaar, E. D. Wilson, K. T. Bainbridge, *Comparison of the Values of the Disintegration Constant of Be^7 in Be, BeO, and BeF_2*4, Phys. Rev. **90** (1953) 610. 19

[50] E. Segr, C. E. Wiegand, *Experiments on the Effect of Atomic Electrons on the Decay Constant of Be^7*, Phys. Rev. **75** (1949) 39; Erratum Phys. Rev. **81** (1951) 284. 19

[51] P. T. Greenland, *Seeking non-exponential decay*, Nature, **335** (1988), p. 298. 19

[52] J. H. Jenkins, et al., *Evidence for Correlations Between Nuclear Decay Rates and Earth-Sun Distance*, Astropart. Phys. 2009. **32**(1): p. 42-46. 19, 20, 21, 23, 102, 162

[53] Fischbach, E., et al., *Time-Dependent Nuclear Decay Parameters: New Evidence for New Forces?* Space Science Reviews 2009. **145**(3): p. 285-335. 19, 162

[54] A. G. Parkhomov, *Deviations from beta radioactivity exponential drop*, J. Mod. Phys. **2** (2011), pp. 13101317. 19

[55] Sturrock, P.A., et al., *Power spectrum analysis of BNL decay rate data*, Astroparticle Physics, 2010. 34(2): p. 121-127. 19, 22, 97, 99, 162

[56] Javorsek II, D., et al., *Power spectrum analyses of nuclear decay rates*, Astropart. Phys. **34** (2010) p. 173-178.

[57] J. H. Jenkins, et al., *Concerning the time dependence of the decay rate of* ^{137}*Cs*, Appl. Radiat. Isot. **74** (2013), pp. 5055. 19

[58] P. A. Sturrock, et al., *Comparative study of beta-decay data for eight nuclides measured at the Physikalisch-Technische Bundesanstalt*, Astropart. Phys. **59** (2014), pp. 4758. 19

[59] Jenkins, J.H. and E. Fischbach, *Perturbation of nuclear decay rates during the solar flare of 2006 December 13*, Astroparticle Physics **31**(6) (2009) p. 407-411. 19

[60] J. Mullins, *Is the sun reaching into earthly atoms?*, New Sci. **202** (2714) (2009), pp. 4245. 19

[61] E. B. Norman, *et al.*, *Evidence against correlations between nuclear decay rates and Earth-Sun distance*, Astroparticle Physics **31** (2009) 135-137. 19

[62] P. S. Cooper, *Searching for modifications to the exponential radioactive decay law with the Cassini spacecraft*, Astroparticle Physics **31** (2009) 267269. 20

[63] T. M. Semkow, et al., *Oscillations in radioactive exponential decay*, Phys. Lett. B. **675** (2009) 415419. 20

[64] E. Bellotti, et al., *Search for time dependence of the 137Cs decay constant*, Phys. Lett. B. **710** (2012), pp. 114117. 20

[65] J. C. Hardy, J. R. Goodwin, V. E. Iacob, *Do radioactive half-lives vary with the Earth-to-Sun distance?*, Appl. Radiat. Isot. **70** (2012), pp. 19311933. 20

[66] J. H. Jenkins, D. W. Mundy, and E. Fischbach, *Analysis of environmental influences in nuclear half-life measurements exhibiting time-dependent decay rates*, Nucl. Instrum. Methods A, **620** (2010) pp. 332-342. 20

[67] P. A. Sturrock, et al., *Concerning the phases of the annual variations of nuclear decay rates*, Astrophysical Journal **737** (2011) 65. 20

[68] R. Bernaei, et al., *Final model independent result of DAMA/LIBRA-phase 1*, Eur. Phys. J. **C73** (2013) 2648. 20, 162

[69] P. A. Sturrock, et al., *Time-Series Analysis of Reconstructed DAMA Data*, arXiv:1210.7496 [hep-ph]. 23, 81

[70] P. A. Sturrock, et al., *Comparative Analyses of Brookhaven National Laboratory Nuclear Decay Measurements and Super-Kamiokande Solar Neutrino Measurements: Neutrinos and Neutrino-Induced Beta-Decays as Probes of the Deep Solar Interior*, Sol. Phys. **291** (2016) pp. 3467-3484. 23, 97, 99

24, 97, 99, 102, 162

[71] R. Arnold, et al., *Technical design and performance of the NEMO-3 detector*, Nucl.Instrum.Meth. **A536** (2005) 79122.

[72] J. Argyriades et al., *Measurement of the background in the NEMO-3 double beta decay experiment*, Nucl.Instrum.Meth. **A606** (2009) 449465. 55

[73] T. Bernatowicz, et al., *Neutrino mass limits from a precise determination of* $\beta\beta$*-decay rates of* ^{128}*Te and* ^{130}*Te*, Phys. Rev. Lett. **69** (1992) pp. 2341-2344. 33

[74] N. Takaoka, Y. Motomura, and K. Nagao, *Half-life of* ^{130}*Te double-upbeta decay measured with geologically qualified samples*, Phys. Rev. C, vol. **53** (1996) pp. 1557-1561. 33

[75] R. Brun and F. Rademakers, *ROOT - An Object Oriented Data Analysis Framework*, Proceedings AIHENP'96 Workshop, Lausanne, Sep. 1996, Nucl. Inst. & Meth. in Phys. Res. A **389** (1997) 81-86. 56

[76] O. Ponkratenko, V. Tretyak, and Y. Zdesenko, *The Event generator DECAY4 for simulation of double beta processes and decay of radioactive nuclei*, Phys.Atom.Nucl. **63** (2000) 12821287. 57

[77] R. Brun, F. Bruyant, M. Maire, A. McPherson, and P. Zanarini, *GEANT3*, CERN-DD-EE-84-1 (1987) . 57

[78] R. Arnold, et al., *Search for Neutrinoless Double-Beta Decay of ^{100}Mo with the NEMO-3 Detector*, Phys. Rev. D **89** (2014) 111101(R). 70

[79] R. Arnold, et al., *First Results of the Search for Neutrinoless Double-Beta Decay with the NEMO-3 Detector*, Phys. Rev. Lett. **95** (2005) 182302. 70

[80] N. R. Lomb, *Least-Squares Frequency Analysis of Unevely Spaced Data*, Astrophysics and Space Science **39** (1976) 447-462 . 81

[81] J. D. Scargle, *Studies in astronomical time series analysis. II. Statistical aspects of spectral analysis of unevenly spaced data*, The Astrophysical Journal **263** (1982) 835-853. 81, 86, 87

[82] M. Zechmeister, M. Kürster, *The generalised Lomb-Scargle periodogram, A new formalism for the floating-mean and Keplerian periodograms*, Astronomy and Astrophysics **496**(2) (2009) 577-584. 81, 87, 89

[83] J. Yoo, et al., *Search for periodic modulations of the solar neutrino flux in Super-Kamiokande-I*, Phys. Rev. D. **68** (2003) 092002. 81

[84] B. Aharmim, et al., *Search for periodicities in the ^{8}B solar neutrino flux measured by the Sudbury Neutrino Observatory*, Phys. Rev. D. **72** (2005) 052010. 81

[85] B. Summer *Measurement of the $2\nu\beta\beta$ decay half-life of ^{150}Nd to the ground state of ^{150}Sm and the search for neutrinoless modes with the NEMO-3 detectors*, Ph.D. Thesis, University of Manchester. 111

[86] H. Gmez, et al., *BiPo: A dedicated radiopurity detector for the SuperNEMO experiment*, AIP Conference Proceedings **1549** (2013) no. 1, 9497. 119

[87] Swisstulle AG, Weinfelderstrasse 66, CH-9542 Mnchwilen; www.swisstulle.ch. 121

[88] P. Adamson *et al.*, *The MINOS Light Injection Calibration System*, 133

[89] M. Kauer, *Search for the double beta decay of Zr-96 with NEMO-3 and calorimeter development for the SuperNEMO experiment*, Ph.D. Thesis, University College of London (2010). 154

[90] Microchip Technology Inc., Chandler, Arizona, U.S.A.; www.microchip.com. 134

[91] Visual Communications Co. LLC, 12780 Danielson Court, Poway, CA 90264, U.S.A.; www.vcclite.com. 138

[92] Mitsubishi Rayon Corp., 520 Madison Avenue, New York, NY 10022, U.S.A.; www.mitsubishi.com. 139